

DRAFT

Multiplicity of Galactic Wolf-Rayet stars

Karan Dsilva

Supervisors:

Prof. Dr. Hugues Sana
(KU Leuven, Belgium)

Dr. Tomer Shenar
(University of Amsterdam, Netherlands)

Dissertation presented in partial
fulfillment of the requirements for the
degree of Doctor of Science (PhD):
Astronomy and Astrophysics

July 2022

Multiplicity of Galactic Wolf-Rayet stars

Karan Dsilva

Supervisors:

Prof. Dr. Hugues Sana
(KU Leuven, Belgium)
Dr. Tomer Shenar
(University of Amsterdam, Netherlands)

Examination committee:

Prof. Dr. Mieke De Cock, chair
(KU Leuven, Belgium)
Prof. Dr. Jon. Sundqvist
(KU Leuven, Belgium)
Dr. Pierre Royer
(KU Leuven, Belgium)
Prof. Dr. Paul Crowther
(University of Sheffield, U.K.)
Prof. Dr. Nicole St. Louis
(University of Montreal, Canada)

Dissertation presented in partial fulfillment of the requirements for the degree of Doctor of Science (PhD): Astronomy and Astrophysics

July 2022

Cover design credit:

Acknowledgements: This research has been funded with funds from the European Research Council (ERC) through the COG MULTIPLES under European Union's Horizon 2020 research programme (grant agreement No. 772225). This work is based on observations carried out with the Flemish Mercator Telescope at the Spanish Observatorio del Roque de los Muchachos (ORM, La Palma, Spain). This research has also made use of the SIMBAD database, operated at CDS, Strasbourg, France.

© 2022 KU Leuven – Faculty of Science
Uitgegeven in eigen beheer, Karan Dsilva, Celestijnenlaan 200D box 2401, B-3001 Leuven (Belgium)

Alle rechten voorbehouden. Niets uit deze uitgave mag worden vermenigvuldigd en/of openbaar gemaakt worden door middel van druk, fotokopie, microfilm, elektronisch of op welke andere wijze ook zonder voorafgaande schriftelijke toestemming van de uitgever.

All rights reserved. No part of the publication may be reproduced in any form by print, photoprint, microfilm, electronic or any other means without written permission from the publisher.

Contents

Contents	i
1 Introduction	1
1.1 Wolf-Rayet stars	2
1.1.1 Observational characteristics	2
1.1.2 Stellar winds	4
1.1.3 Multiplicity and its effect on stellar evolution	5
1.1.4 Formation and evolution of WR stars	7
1.2 WR stars in the Milky Way	11
1.2.1 Observed distributions	11
1.2.2 Observed multiplicity properties	11
1.2.3 Observational biases	15
1.3 Motivation and outline of this thesis	17
2 Data reduction	19
2.1 Introduction	20
2.1.1 Instrumental response function	20
2.2 HERMES Pipeline	21
2.2.1 Atmospheric extinction and telluric correction	21

2.2.2	Response correction	22
3	Multiplicity properties of the carbon-rich Wolf-Rayet population	26
3.1	Introduction	27
3.2	Overview of the sample and data reduction	28
3.2.1	The sample	28
3.2.2	Observations	28
3.2.3	Data reduction and normalisation	29
3.3	Radial velocity determination	31
3.3.1	Cross-correlation	31
3.3.2	Mask selection	33
3.3.3	Uncertainties from systematic sources and wind-variability: A proto-study of the binary WR 137	34
3.4	Results and discussion	37
3.4.1	Observed spectroscopic binary fraction	37
3.4.2	Comparison with the literature	38
3.4.3	Intrinsic multiplicity properties	40
3.5	Evolutionary implications and conclusions	45
4	Multiplicity properties of the Galactic WNE population	46
4.1	Introduction	48
4.2	Sample and data reduction	48
4.2.1	Sample	48
4.2.2	Data reduction and normalisation	49
4.3	Measuring radial velocities	49
4.3.1	Cross-correlation and mask selection	50
4.3.2	Studying the long-period binary system WR 138 to quantify wind variability	52

4.4	Observed binary fraction	55
4.5	Intrinsic multiplicity properties	56
4.5.1	Detection probability	56
4.5.2	Adopting a Bayesian approach	58
4.5.3	Revisiting the WC sample	61
4.6	Discussion	63
4.6.1	Comparison of the binary properties with the literature	63
4.6.2	Observational biases due to the magnitude limit	63
4.6.3	Implications for binary evolution	64
4.7	Conclusions	66
5	Multiplicity properties of the Galactic WNL population	68
5.1	Introduction	69
5.2	Sample and data reduction	70
5.3	Radial velocity measurements	71
5.3.1	Cross-correlation to measure radial velocities	71
5.3.2	Wind variability and its effect on radial velocity measurements	71
5.4	Results	74
5.4.1	Observed binary fraction and detection probability	74
5.4.2	Multiplicity properties: WNL population	75
5.4.3	Multiplicity properties: combined WN population	80
5.5	Discussion	80
5.5.1	Comparison with the literature	80
5.5.2	Observational biases due to the limiting magnitude	81
5.5.3	Consequences on binary evolution	82
5.6	Conclusions	85
6	Summary and future work	86

6.1	Summary	86
6.2	Future work	88
6.2.1	Expanding the sample	88
6.2.2	An improved Bayesian analysis	89
6.2.3	Orbital analysis of WR binaries	89
A	Appendix for Chapter 3	91
A.1	Comments on specific objects	91
A.2	Relative RV measurements	94
B	Appendix for Chapter 4	103
B.1	Comments on specific objects	103
B.2	Relative RV measurements	107
B.3	Posterior plots from MC simulations	109
B.3.1	WC sample	112
C	Appendix for Chapter 5	121
C.1	Comments on individual objects	121
C.2	Relative radial velocity measurements	123
Bibliography		133
List of publications		147

Chapter 1

Introduction

Massive stars have initial masses larger than eight times the mass of our sun ($M_i \gtrsim 8 M_{\odot}$) and are fundamental cosmic engines. Through their strong stellar winds, intense radiation and powerful explosions, they dominate the transport of energy and momentum into the interstellar medium (Mac Low et al. 2005). The final explosions of massive stars are so bright that they can be seen throughout the universe and allow the study of its properties across cosmic times (Tanvir et al. 2009). The first generation of massive stars are thought to have played a pivotal role in the assembly of the first galaxies (Bromm & Larson 2004; Robertson et al. 2010). They are potential progenitors of core-collapse supernovae (SN) and gamma-ray bursts (Woosley & Bloom 2006), the remnants of which are neutron stars (NS) and black holes (BHs). In binary systems, these compact objects can undergo coalescence to produce intense bursts of gravitational waves.

Despite their importance in a variety of astrophysical phenomena, there remain major uncertainties in our understanding of massive stellar evolution. Processes such as internal mixing, rotation, magnetic fields and multiplicity are few of the numerous parameters that strongly affect the mass, and hence evolution, of a star. In the past decades, observational surveys have shown that multiplicity is the rule, and not the exception, among massive OB-type stars (Mason et al. 1998, 2009; Sana et al. 2012, 2013, 2014; Kobulnicky et al. 2014; Barbá et al. 2014; Dunstall et al. 2015; Maíz Apellániz et al. 2016, 2019; Almeida et al. 2017; Banyard et al. 2022; Villaseñor et al. 2021). Most of the stars in these systems will interact with their companions (Fryer et al. 2007; Sana et al. 2012, 2013; Dunstall et al. 2015), thereby fundamentally impacting the evolution of most of these systems (Paczyński 1967; Pols 1994; Vanbeveren et al. 1998; de Mink et al. 2014). This thesis mainly addresses the aspect of multiplicity in a subset of massive stars, called Wolf-Rayet (WR) stars,

from an observational standpoint. This **chapter** provides a brief introduction on stellar evolution, summarises the characteristics of WR stars, dives into the Galactic population of WR stars and provides the motivation for this thesis.

1.1 Wolf-Rayet stars

The content of this section is mainly based on [Crowther \(2007\)](#) and [Langer \(2012\)](#).

A small subset of massive stars appear as WR stars. The class is named after French astronomers Charles Wolf and Georges Rayet, who in 1867 observed and identified three stars in the constellation Cygnus whose spectra showed spectacularly broad and strong emission lines, particularly of He II $\lambda 4686$. In the context of stellar evolution, WR stars are candidate progenitors of core-collapse SN and BHs, making their study quintessential in understanding the initial properties of such phenomena.

1.1.1 Observational characteristics

WR stars comprise a spectral class of stars with emission-line dominated spectra. They appear in multiple “flavours” based on the chemical composition of their atmospheres: nitrogen-rich (WN), carbon-rich (WC), and the rare oxygen-rich (WO) sequences (Fig. 1.1). Based on the strengths and ratios of various emission lines, WN and WC stars are also sub-classified as early (WNE: WN2-WN5, WCE: WC4-6) or late (WNL: WN6-WN9, WCL: WC7-9) following the convention from [Smith \(1968b\)](#). The spectral types of WN stars can be suffixed by ‘h’ or ‘o’ depending on the presence or absence of hydrogen in the spectra. **WC stars often have the letter ‘d’ as a suffix, indicating the presence of dust (usually detected in the infrared).**

The optical emission-line spectra of WR stars are primarily constituted by recombination lines. The strength of these lines depend on the number of electrons and ions in the outflowing wind, and hence scale with the square of the density. This is why the spectral appearance of a WR and O star are drastically different, despite the wind density changing by only a factor of 10 or so. The high density in the wind also results in a high optical depth, such that the **hydrostatic layers are** hidden from sight. Therefore, the spectra of WR stars are formed in the geometrically-extended, fast-moving stellar wind. As a result, it is challenging to obtain information about the stellar parameters through spectroscopic analysis, as this requires an in-depth understanding of the structure of the wind.

WR stars are notorious for their line-profile variability ([Lepine et al. 1996](#); [Lépine et al. 2000](#); [St-Louis et al. 2009](#); [Chené & St-Louis 2011](#); [Chené et al. 2020](#)). This is usually attributed to inhomogeneities in the wind, which results in the spectral lines of WR

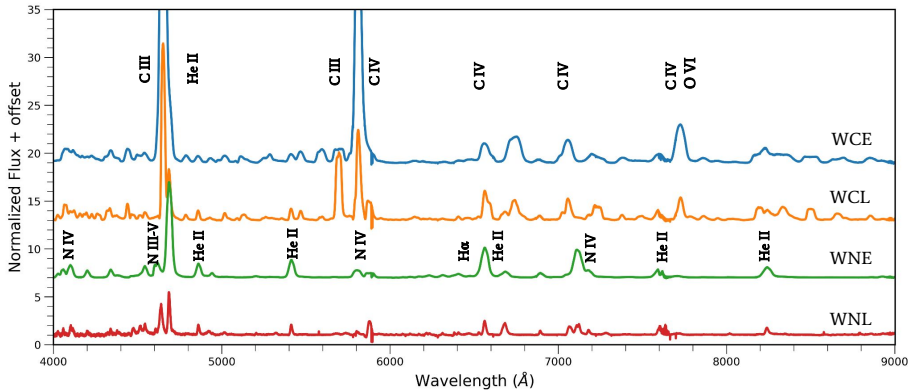


Figure 1.1: HERMES spectra of WR 111 (WCE), WR 135 (WCL), WR 6 (WNE) and WR 120 (WNL) demonstrating the different spectral features of the various WR sub-types in the Galaxy. The spectra are rebinned for clarity and plotted with an offset, with various spectral lines indicated in black.

stars changing their appearance over time. Periodic change in the equivalent widths and the full-width half maximum of line profiles has even led to speculations of binary companions (e.g. WR 1 [Morel et al. 1999](#)). In the recent years, it has been shown that certain WR stars harbour large-scale structures that could cause such periodicity (e.g. [St-Louis et al. 2008](#); [Aldoretta et al. 2016](#); [St-Louis et al. 2018](#)). The photometry of WR stars also shows quasi-periodic variability on short timescales (e.g. [Moffat & Shara 1986](#); [Balona et al. 1989](#); [St-Louis et al. 2020](#)), which have been attributed to non-radial pulsations, co-rotating interaction regions (CIRs) or binary companions.

WR stars are usually found in isolated regions, although a fair fraction of them in the Galaxy are found in young clusters ([Rosslowe & Crowther 2015](#)). A small fraction of WR stars also have nebulae surrounding them, showing a variety of morphological features ([Toalá et al. 2015](#)). These nebulae are often associated with young WR stars, particularly WN sub-types, although some have been found around WC stars. The nebulae are a result of strong, UV radiation from the WR star interacting with and photo-ionizing the material ejected in a past RSG/LBV phase.

Since the WR phenomenon is defined by observational, spectroscopic characteristics, multiple objects come under the umbrella term. There are three main types of stars that are classified as WR stars:

- ◊ **Main-sequence WR stars:** stars with initial masses $\sim 80 M_{\odot}$ and higher have winds so strong that they can exhibit a WR-like appearance while burning hydrogen in their cores ([Langer et al. 1994](#); [Crowther et al. 1995](#); [de Koter](#)

[et al. 1997](#)). They show lines of hydrogen in their spectra and are called WNh stars (the suffix “h” indicating hydrogen).

- ◊ **Classical WR stars:** these are hydrogen-depleted, helium-rich stars that are thought to be the descendants of WNh and main-sequence O stars with initial masses from $25 M_{\odot}$ and above. Having evolved off the main sequence in the HR diagram, these stars are no longer burning hydrogen in their cores. They are called cWR stars, and are potential candidates as progenitors of type-Ib/c supernovae.
- ◊ **Central stars of planetary nebulae:** as relatively massive post-ABG stars evolve into planetary nebulae, the inner core that is exposed is hot enough to drive strong winds, appearing as WR stars. These are often referred to as [WR] stars (e.g. [Webster & Glass 1974](#)) and are a small subset of all central stars of planetary nebulae. These stars formally stem from lower-mass ($M_i \leq 8 M_{\odot}$) objects.

A large fraction of [WR] stars have been found in short-period binary systems, whose formation could potentially be explained through a common-envelope scenario ([Miszalski et al. 2009, 2011; Jones et al. 2015](#)). Complementing this, a handful of dust-forming, candidate long-period [WC] binaries are being monitored using spectroscopy ([Manick et al. 2015; Miszalski et al. 2015](#)). These objects are thought to be the lower-mass analogues of classical WR stars, and hence understanding their binary evolution history is useful when studying their massive counterparts. However, in this work we refrain from discussing them further and focus on classical- and main-sequence WR stars.

Another point that must be brought to attention is the difference between WNh and WNH stars. Given that a fraction of both WNE and WNL stars are observed contain hydrogen in their spectra (e.g. WR 3 - WN3ha and WR 108 - WN8ha), [Smith & Conti \(2008\)](#) advocated the usage of the term ‘WNH’ stars to encompass the luminous, hydrogen-rich WN stars of both early- and late-type that are hypothesised to be the progenitors of cWR stars. On the other hand, as mentioned previously, the suffix ‘h’ is part of the nomenclature for the spectral classification of WR stars, to denote the presence of hydrogen in the spectra (‘ha’ for hydrogen in absorption).

1.1.2 Stellar winds

The high temperatures and luminosities of massive stars imply that most of their radiation is in the UV. Given the plethora of spectral lines present in the UV domain (mainly of iron), this radiation induces a force strong enough to drive material away

from the star. This stream of outflowing material is then called a radiation-driven stellar wind (Lucy & Solomon 1970; Castor et al. 1975). As material is accelerated away from the star, spectral lines are Doppler-shifted due to their high velocities, and so photons with wavelengths away from the line-center can also interact with these atoms, further increasing the radiative force on the wind.

The outflows of massive stars were initially thought to be homogeneous and smooth (de Jager et al. 1988; Nieuwenhuijzen & de Jager 1990). However, photometric and spectroscopic observations of WR stars showed variability over timescales too short to be attributed to a companion, implying a structured wind (Moffat & Haupt 1974; Lamontagne & Moffat 1987; Moffat & Shara 1986; Moffat et al. 1988; Brown et al. 1995; Lépine et al. 2000). Indeed, this was followed by theoretical studies indicating that massive-star outflows are clumpy (Owocki et al. 1988; Dessart & Owocki 2005; Sundqvist & Owocki 2013; Sundqvist et al. 2018; Driessen et al. 2019). Similar to the stellar outflows of all massive stars, the winds of WR stars are also clumpy (Hillier 1991; Hamann & Koesterke 1998; Puls et al. 2006; Fullerton et al. 2006).

There are a number of unanswered questions related to the atmosphere models of WR stars. First, spectroscopic observations of WR stars find WR radii much larger than those predicted by theory (Crowther 2007; Hamann et al. 2019; Sander et al. 2019). This is called the WR core-radius problem. Secondly, the structure of WR winds are still a point of research, as the launching mechanisms in one-dimensional optically thick winds fail to sustain a stellar wind that can escape the stellar potential (e.g. Ro & Matzner 2016; Sander et al. 2017). Poniatowski et al. (2021) showed that WR winds can be launched with a hybrid-opacity model, and that the inner regions of WR winds are dynamically inflated. This also provides a potential solution to the WR core-radius problem. Three-dimensional radiation-hydrodynamic simulations by Moens et al. (2022) have shown that, for sufficiently-high luminosities, the winds can be launched from the deep sub-surface regions. Moreover, their simulations also predict structure in the winds of WR stars. Comparing observational time-series data of spectra (e.g. Lépine et al. 2000) with synthetic predictions to constrain wind parameters is something that is now feasible.

1.1.3 Multiplicity and its effect on stellar evolution

The content of this section is mainly based on Podsiadlowski et al. (1992) and Hilditch (2001)

As explained earlier, the majority of massive stars have been found to reside in binaries. Most of these binary systems will interact with each other over the course of their lifetimes by exchanging mass and/or by undergoing a merger. These events significantly

affect their further evolution (see, e.g. [Pols 1994](#); [Langer 2012](#)). The initial orbital period (P) and the mass-ratio ($q \equiv M_2/M_1$) of a binary system are the primary factors that will influence their evolution ([Podsiadlowski et al. 1992](#)).

In binary systems that are sufficiently close, the gravitational force of the individual components are strong enough to affect their companions. These *tidal* forces are capable of changing the orbital parameters of the binary system over time. In particular, tidal forces tend to circularise the orbit and synchronise the rotation period of the individual components with the orbital period. The timescale for synchronisation are much shorter than what is expected for circularisation of the orbit. However, both of these timescales are smaller than the main-sequence lifetimes for massive stars, and so by the end of the hydrogen-burning phase, close binaries are expected to be synchronously rotating and in circular orbits ([Hut 1981](#); [Zahn 1977](#)). Tides also influence the shapes of the binary components to the extent where they deviate significantly from sphericity. The formulation of the gravitational potential along with equipotential surfaces in binary systems is called the Roche model (Fig. 1.2).

In the Roche model, binaries that are well-detached will have spherical stars, as indicated by the circles around m_1 and m_2 . As we move away from the centres of the stars, the equipotential surfaces are distorted. The point where the equipotential surfaces away from m_1 and m_2 come into contact is called the inner Lagrangian point (L1). The limiting volumes marked by this equipotential surface are called the Roche lobes of the stars. There are other points of equal potential in this model, of which only the outer Lagrangian point (L2) is marked in this figure. It is through L2 that mass can most easily escape from the gravitational field of the binary system.

Aside from tidal forces, a stronger catalyst of interaction is driven by the exchange of mass, and therefore angular momentum, between the stars in a binary system (see, e.g., [Paczyński 1967](#); [de Mink et al. 2013](#); [Podsiadlowski et al. 1992](#)). The massive component in the binary (the primary) will evolve faster and, after it fills its Roche lobe, will transfer mass through L1 to the secondary. This process is called Roche-lobe overflow (RLOF). Depending on the evolutionary stage in which the primary fills its Roche lobe, mass transfer can occur when the primary is on the main sequence (Case A), during hydrogen-shell burning in the transitional phase towards a red (super)giant (Case B), or after the (super)giant phase (Case C).

Additionally, the stability of mass transfer also influences the evolution of the orbit. If the secondary is able to accrete all of the material donated by the primary such that the total mass and angular momentum of the system is conserved, this is called conservative mass transfer. During conservative mass transfer, the orbital period will shrink until the mass-ratio reaches unity (i.e., $q \equiv m_2/m_1 = 1$). If the primary continues to donate mass even after this then the orbital separation and period will increase. In this process, the hydrogen-rich envelope of the primary is stripped by the secondary star. It will accrete mass and spin up as it gains angular momentum, while the primary

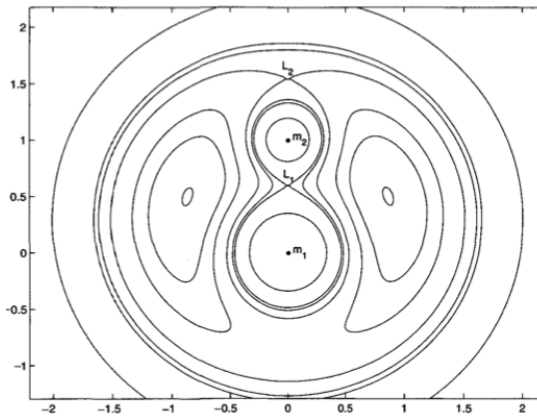


Figure 1.2: The Roche model for gravitational potential in a close binary system with stars of masses m_1 and m_2 , where $m_1 > m_2$. The solid lines mark equipotential surfaces, with the innermost circles depicting the stellar radii. The Lagrangian points L1 and L2 are also depicted (see text for more information). Figure from [Hilditch \(2001\)](#).

appears hot and compact as its inner layers are exposed.

Another reasonable scenario that can be expected to occur is that in which only part of the mass and angular momentum is transferred by the primary to the secondary, while the rest is ejected from the system. Rapid mass transfer on a dynamical timescale after the primary undergoes RLOF would result in the secondary being unable to accrete all of the mass, resulting in the formation of a common envelope (CE). This is more likely to occur in cases of extreme mass-ratios (see, e.g., [Ivanova et al. 2013](#)), although the details are still quite uncertain. The friction between the common envelope and the orbiting stars causes energy to be transferred into the envelope and the orbital period shrinks. When sufficient energy is injected into the envelope, it is expelled and a tight binary remains. This phase is thought to be rapid, such that the secondary emerges unchanged. In cases where the envelope cannot be ejected, a stellar merger occurs. Extreme mass loss via stellar winds, which can occur in the case of WR stars, is also a case of non-conservative mass transfer. In this case, mass loss results in the increase in the period of the binary.

1.1.4 Formation and evolution of WR stars

The content of this section is mainly from [Crowther \(2007\)](#) and [Shenar et al. \(2020\)](#).

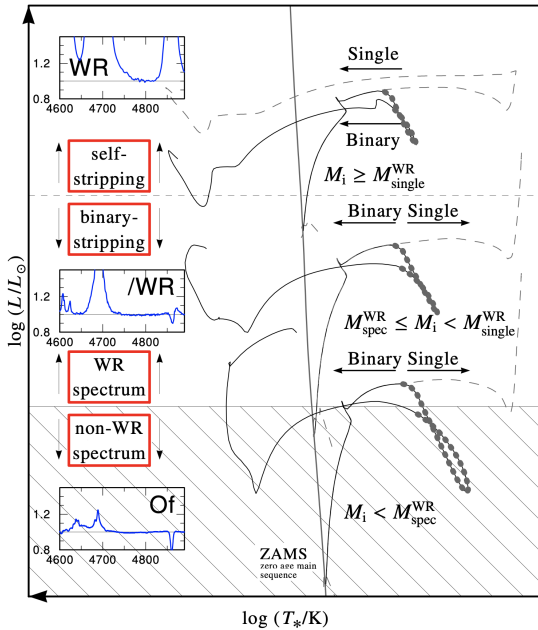


Figure 1.3: An illustration of the different formation channels through which WR stars can be formed. $M_{\text{single}}^{\text{WR}}$ is the minimum initial mass for a star to be able to strip itself via stellar winds. $M_{\text{spec}}^{\text{WR}}$ is the minimum initial mass required for a star to appear as a WR star *after* being stripped. Figure adopted from [Shenar et al. \(2020\)](#) with stellar evolution models from BPASS.

[Gamow \(1943\)](#) first suggested that the chemical composition of the spectra of WR stars showed the products of nuclear fusion in the core of massive O-type stars. For this to be possible, an O star has to shed its hydrogen-rich envelope. An explanation was provided by [Paczyński \(1967\)](#), who explained that this was possible through mass-transfer in close binaries. This led to the initial claim that all WR stars were the product of binary interaction. Soon after this, Peter Conti hypothesised that a single, massive star could shed its hydrogen envelope through mass loss via its own stellar winds. As the star further evolved, first the products of hydrogen-burning (through the CNO-cycle, nitrogen) and then helium-burning (through the triple-alpha process, carbon) would be exposed. This came to be known as the “Conti evolutionary scenario” or simply the “Conti scenario” ([Conti 1976](#)). This explanation became more popular as it did not require external help for an O star to evolve into a WR star. O stars can also lose mass through episodic outbursts due to instabilities (e.g. [Langer et al. 1994](#)) or due to continuum driven instabilities ([Smith & Owocki 2006](#)).

Ever since it was shown that the majority of O stars live in close binaries that will interact over the course of their lifetime (Sana et al. 2012), the debate over the dominant mechanism through which the envelope of an O star is stripped is still ongoing (Vanbeveren et al. 1998; Foellmi et al. 2003a; Shenar et al. 2019; Neugent & Massey 2014; Shenar et al. 2020). Since the opacity required for the driving of stellar winds is dependent on metallicity, the mass-loss rates of massive stars decrease with reduced metallicity (Vink et al. 2001; Vink & de Koter 2005; Hainich et al. 2015; Shenar et al. 2019). As a result, it was thought that envelope stripping by a companion is the major formation channel at lower metallicities (Maeder & Meynet 1994; Smith 2014; Groh et al. 2019). For example, according to Meynet & Maeder (2003, 2005) a star with an initial mass of $25 M_{\odot}$ can strip itself at solar metallicity. This value increases to $\sim 45 M_{\odot}$ for the SMC, although both of these values are highly dependent on underlying assumptions. However, Shenar et al. (2020) have shown that while binary stripping might occur for most stars at lower metallicities, the resulting stars will not have strong enough stellar winds to appear as WR stars (Fig. 1.3). Hence, the role of binary interactions in forming WR stars, in our Galaxy as well as across the Cosmos, remains an unsolved problem.

Evolution at Galactic metallicity

Stars with initial masses $M_i \gtrsim 25 M_{\odot}$ are able to strip their envelopes via their stellar winds. They are thought to avoid the cooler supergiant phase, instead experiencing strong mass-loss through stellar winds or through episodic eruptive events in the luminous blue variable (LBV) phase. After the LBV/RSG phase, these stars may appear as WR stars (Fig. 1.4). This phase is short-lived ($\sim 10\%$ of the stellar lifetime) after which they end their lives either as Type Ib/c supernovae or through direct collapse, leaving behind NS or BHs (Heger et al. 2003).

Observational analysis of WR stars is important in understanding their mass-loss rates, radii and masses, among other parameters. For the population of single Galactic WR stars, the atmospheric-modelling work of Hamann et al. (2019) for WN stars and Sander et al. (2019) for WC stars has been significant. With distances from Gaia DR2, Hamann et al. (2019) confirmed that most WNL stars are slightly more luminous than WNE stars. Sander et al. (2019) also showed with Gaia DR2 distances that the luminosity and temperature of WC stars was, on average, similar to that of Galactic WNE stars. In their analysis, Hamann et al. (2019) also show that most, if not all, WNL stars contain hydrogen in their spectra. An updated evolutionary channel for single O stars to evolve into WR stars, based on their initial mass (modification to the Conti scenario) is given in Sander et al. (2019). For $M_i > 80 M_{\odot}$,



for $35 \leq M_i \leq 80 M_{\odot}$,

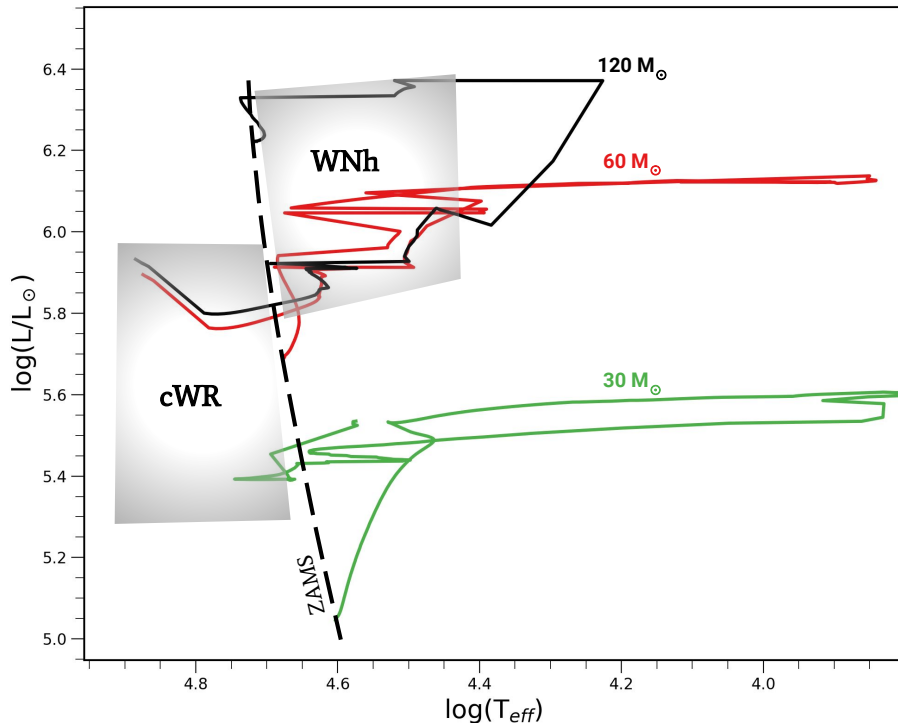


Figure 1.4: Hertzsprung-Russel diagram showing the evolution of massive stars using tracks from the Geneva code (Ekström et al. 2012). Evolution tracks for initial masses of 30, 60 and 120 M_{\odot} are shown, along with the zero-age main sequence (ZAMS). The shaded grey areas are regimes where stars can appear as WNh (**hydrogen-rich WN stars**) or cWR stars.

$O \rightarrow O/WNH \longleftrightarrow LBV \rightarrow WN \rightarrow WC \rightarrow WO \rightarrow CC$,

for $18 \leq M_i \leq 35 M_{\odot}$,

$O \rightarrow RSG \rightarrow WNL [\longleftrightarrow LBV] \rightarrow WN \rightarrow WC \rightarrow WO \rightarrow CC$,

and for $8 \leq M_i \leq 18 M_{\odot}$,

$OB \rightarrow RSG [\rightarrow BSG] \rightarrow SN II$

where ‘CC’ indicates core-collapse. The mass ranges above are not set in stone, and they are derived by comparing empirically derived luminosities to stellar evolution models. However, the specific end stages presented above are widely debated in the literature and depend on the physics included in evolutionary models (e.g., see Heger et al. 2003; Woosley & Bloom 2006; Lamers & Levesque 2017).

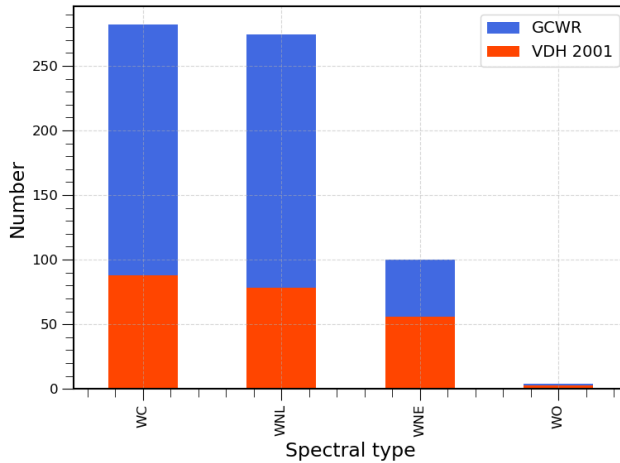


Figure 1.5: Distribution of Galactic WR stars from [VDH01](#) and [GWCR](#) versus their spectral types.

1.2 WR stars in the Milky Way

1.2.1 Observed distributions

The largest observed sample of Galactic WR stars is the VIIth catalogue of WR stars ([van der Hucht 2001](#), henceforth [VDH01](#)). Given the high interstellar extinction in the Galaxy, a large number of WR stars are quite faint in the optical. However, they are bright in the infrared (IR) regime ([Rosslowe & Crowther 2015](#)), and hundreds have been found since ([Mauerhan et al. 2009](#); [Shara et al. 2009, 2012](#); [Faherty et al. 2014](#); [Rosslowe & Crowther 2018](#)). Currently, the Galactic Catalogue of WR stars (v1.25) has 667 stars and is being maintained by Paul Crowther¹ ([Rosslowe & Crowther 2015](#); [Rate & Crowther 2020](#), henceforth [GCWR](#)). The distribution of Galactic WR stars from the [GCWR](#) and [VDH01](#) over their spectral types is shown in Fig. 1.5, with their distances in Fig. 1.6. The distances reported in the [GCWR](#) are, aside from individual reports, Gaia DR2 distances from [Rate & Crowther \(2020\)](#).

1.2.2 Observed multiplicity properties

When trying to understand the evolution of a binary system, it is important to define the orbital parameters: the period P , eccentricity e , inclination i , mass-ratio q , etc.

¹<http://pacrowther.staff.shef.ac.uk/WRcat/>

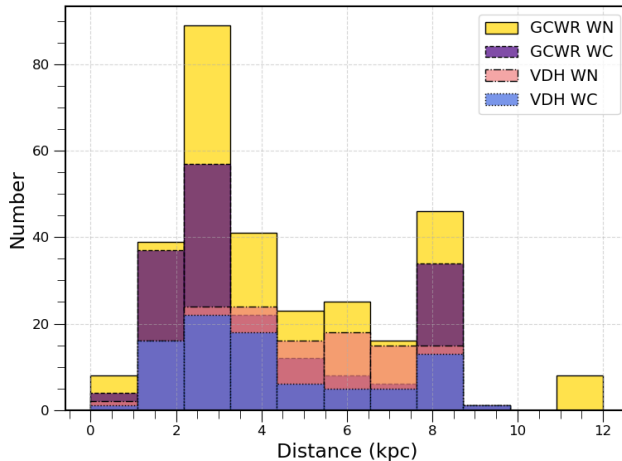


Figure 1.6: Distances to Galactic WR stars from [VDH01](#) and GWCR.

Based on the evolution of the individual stars, these parameters will change over the course of their lifetimes. Knowledge of these parameters allows us to predict if binary systems interact, merge or become unstable. While there are more parameters to work with (as compared to single stars), binary systems offer the benefit of being able to measure the (minimum) masses of the individual components **using** Kepler's laws. This is extremely beneficial in the context of WR stars, since these direct measurements of dynamical mass and radius are valuable in constraining evolutionary models, of importance is the period distribution of the WR binary population, which help calibrate the physics of binary interaction in population syntheses codes.

The observed fraction of Galactic WR stars in binaries was reported to be ~ 0.4 by [VDH01](#). This fraction is based on a compilation of 227 WR stars, of which 87 (43% binaries) are of the WC sub-type, 127 WN stars (39% binaries), 10 WN/WC stars. This includes very-long and extremely-long period binaries ($P > 1000$ d), and binaries identified through different methods (e.g. spectroscopy, visual binaries, photometry). Without going into details, we also examine the observed multiplicity at different metallicities. Through spectroscopic surveys, the multiplicity fraction of WR stars in the Large and Small Magellanic Clouds (LMC and SMC) were found to be ~ 0.3 and ~ 0.4 respectively ([Bartzakos et al. 2001](#); [Foellmi et al. 2003a,b](#); [Schnurr et al. 2008](#)). At higher metallicities, [Neugent & Massey \(2014\)](#) found that in the galaxies M31 and M33, the fraction of WR stars in short period binaries was ~ 0.3 . Although the number of WR stars in these galaxies are lower than those in our own and the detection of binarity probably more difficult, the observed binary fraction seems to be roughly independent of metallicity.

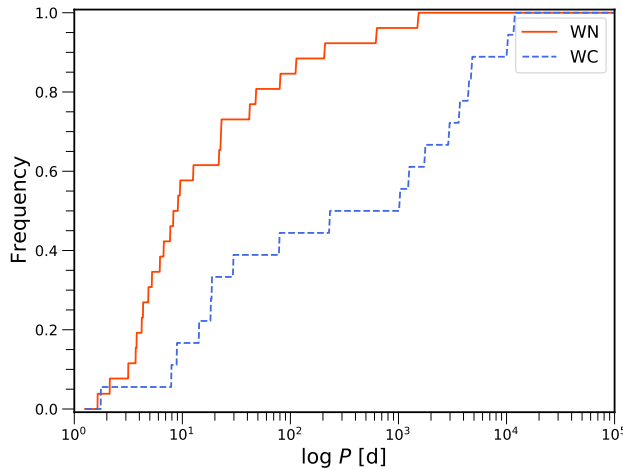


Figure 1.7: Observed period distribution of Galactic WC and WN binaries from [VDH01](#).

Returning our attention to the Galactic population, the stars in the GCWR have not been examined for binarity in a homogeneous manner. The cumulative orbital period distribution from [VDH01](#) is presented in Fig. 1.7. It is clear that the period distribution of Galactic WC binaries is skewed towards longer periods compared to that of the WN population. While $\sim 60\%$ of WN binaries with known orbital periods have periods less than 10 days, the equivalent fraction for the WC binaries is only reached at orbital periods of ~ 1000 days. An important distinction to highlight here is the lack, but not the absence, of short-period (10–100 d) WC binaries when compared with the Galactic WN population. This is somewhat surprising, since short-period WR binaries should be the easiest to detect, given the large Doppler motion.

Detecting Wolf-Rayet binaries

Apart from orbital analysis, there are a multitude of techniques used to identify WR binaries. Depending on the orbital period, brightness-ratio, mass-ratio and inclination of these systems, different observational techniques allow for observers to detect WR binaries.

Dilution of emission lines: This technique only works when the brightness of the companion is comparable to the WR star. If a WR star is in a binary with an OB companion, the strength of the WR emission is theoretically diluted by the light from the companion ([Smith 1968](#); [Conti & Massey 1989](#); [Crowther 2007](#)). However, if the companion is as bright or brighter than the WR star, then the composite spectrum of the system can even show absorption lines from the companion. Moreover, the strengths

of emission lines of WR stars are not set in stone, and it is not always clear whether weak emission is the result of line dilution or weak winds.

Identifying absorption lines in the spectrum: This is a common technique used when it is difficult to obtain multi-epoch data on WR stars (e.g., [Conti & Massey 1989](#)). A high signal-to-noise, high resolution spectrum is often enough to detect absorption lines from a companion. However, some WR stars, especially at low metallicity (e.g., [Hainich et al. 2015](#)), show pseudo-absorption lines in their spectra, making them difficult to discern from a potential companion. Similar to the first method, this only works if the companion is comparable in brightness, even if the orbital period is of the order of years.

Periodic change in the equivalent-width of spectral lines: In WR stars that have strong line-profile variability, a technique to measure periodicity is through the equivalent widths of particular spectral lines. Such line-profile variability would occur if the companion was close enough for their winds to interact, i.e. with periods of a few days. However, the interpretation of this periodicity could also be co-rotating interaction regions, other large-scale structures in the wind, non-radial pulsations or an embedded neutron star/low-mass object in the wind of the WR star (see Sect. 1.1.1). **This technique was prominently used to detect a short-period signal in the emission lines of WR 1** [Morel et al. \(1999\)](#).

Spectroscopic monitoring campaigns: Spectroscopic campaigns are another way of detecting WR binaries. As spectroscopy relies on detecting significant radial velocity (RV) variations in the WR star, it is highly sensitive to orbital periods up to a year, high inclinations and mass-ratios ($q = M_{\text{WR}}/M_2$) of the order of unity or higher (see e.g., [Marchenko et al. 1998a](#); [David-Uraz et al. 2012](#); [Richardson et al. 2021](#)). These systems can be classified as either SB1 (only one component detected in the spectra) or SB2 systems. The advantage of this method is that orbital solutions using Kepler's equations give us a model-independent method of determining minimum masses of the WR star and its companion. As mentioned before, this technique (and the previous two) are insensitive to small mass-ratios, as the companion would be too faint and too low-mass to induce RV variations in the WR star.

Interferometric campaigns: As the orbital period increases to more than a few years, spectroscopic campaigns are quite inefficient at catching these binaries. The increase in the orbital period also implies a larger physical separation, and this is where interferometry plays a significant role. At separations of 1-10 AU, long-baseline interferometry can resolve the visual orbits of WR binaries (e.g. for WR 113 and WR 140, respectively: [Richardson et al. 2021](#); [Thomas et al. 2021](#)). This translates to periods of 1 to \sim 20 yr.

Infrared photometry: Another technique used to monitor long-period WC binaries is through infrared photometry ([Williams 1995](#); [Marchenko et al. 1999](#); [Williams et al.](#)

2001, 2005; Williams 2019). WC stars are episodic dust makers, and the popular theory is that the WR + OB binary develops the right conditions to produce dust at periastron passage. These usually require decades of monitoring, **and is only useful when hunting for WC binaries since long-period WN binaries are not known dust producers. As a result, the observed period distribution of WC binaries have a larger number of systems at long periods as compared to that for the WNs.**

Other techniques: Lastly, long period binaries can be detected via imaging, X-rays from colliding winds or via non-thermal radio excess (e.g. Dougherty et al. 1996, 2000; Zhekov 2017; Rodríguez et al. 2020; Zhekov et al. 2020).

1.2.3 Observational biases

The detection of binaries through spectroscopic campaigns mainly depends on the Doppler shifts of the WR line-profiles. These depend on the orbital parameters of the system, which we describe briefly. Any binary system can be defined by

- ◊ orbital period (P) of the binary
- ◊ mass-ratio, defined here as ($q = M_{\text{WR}}/M_2$)
- ◊ eccentricity (e) of the orbit
- ◊ inclination (i) of the orbit with respect to the plane of the sky
- ◊ longitude of the ascending node of the secondary (Ω)
- ◊ argument of the periastron of the secondary, measured with respect to the ascending node (ω)

In a spectroscopic campaign, selected targets are observed with a particular combination of telescope/instrument for a certain amount of time. The total length of the observational campaign is called the *time-base*, and the number of epochs observed spread out over the time-base is called the *sampling*. The Doppler motion of the WR star is measured through RVs, which vary periodically over the orbital period. The semi-amplitude of the WR RV is called K_{WR} , and it is related to the orbital parameters listed above. The semi-amplitude of the secondary is called K_2 . These amplitudes are directly related to the mass-ratio, through

$$K_2/K_{\text{WR}} = q \quad (1.1)$$

As mentioned above, the orbital configuration of the system (or orbital phase, ϕ) define the properties of the RV variations. As an example, we consider a binary system with

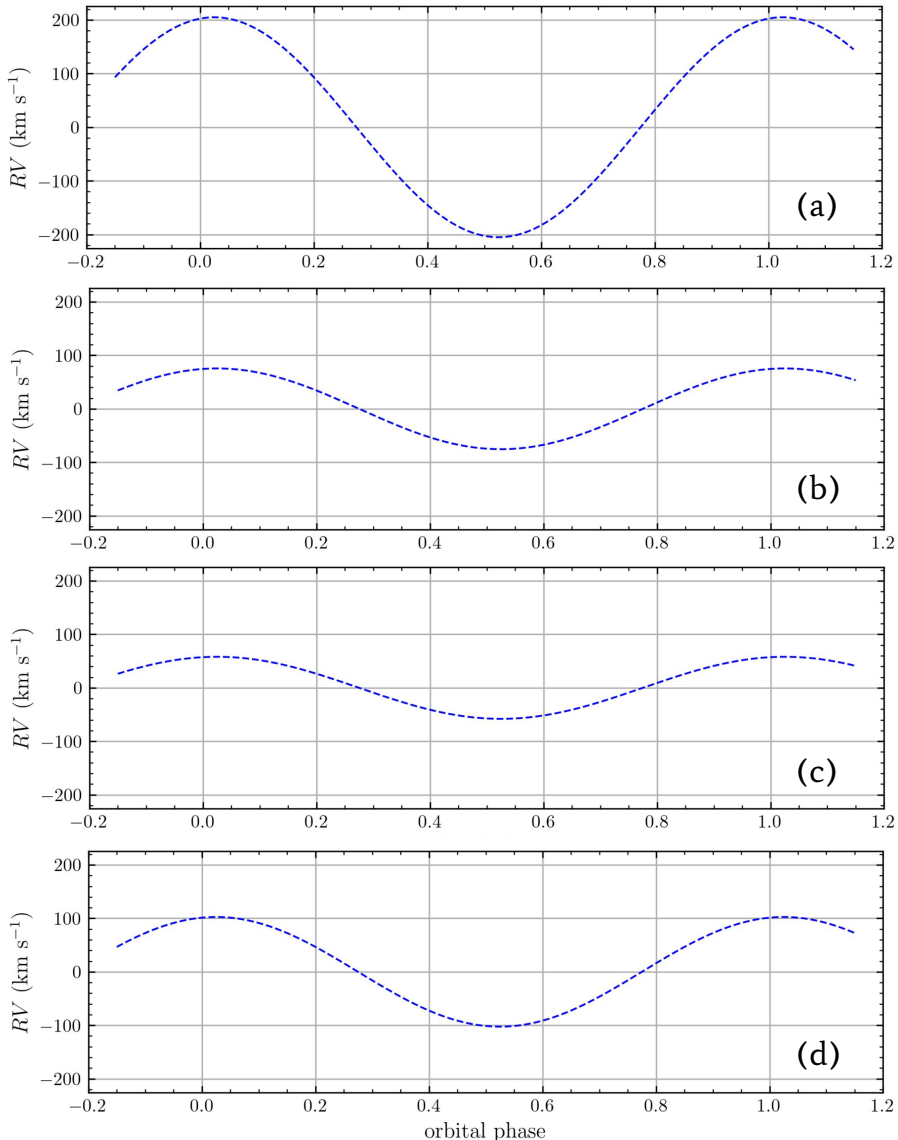


Figure 1.8: Theoretical RV plots from spinOS (Fabry et al. 2021) for a star in a binary system with $P = 15 \text{ d}$, $q = 0.5$, $e = 0$ and $i = 90^\circ$ (panel (a)). The change in ΔRV is shown by keeping all the parameters constant and varying (b) $P = 300 \text{ d}$, (c) $q = 3$ and (d) $i = 30^\circ$.

$M_{\text{WR}} = 15 M_{\odot}$ and $M_2 = 30 M_{\odot}$. For simplicity, the orbit is circular ($e = 0$), implying the Ω and ω are not of consequence for now. With $P = 15$ d and $i = 90^\circ$, the theoretical RV curve computed with spinOS (Fabry et al. 2021) can be seen in panel (a) of Fig. 1.8. **By changing the period (panel (b), $P = 300$ d), mass-ratio (panel (c), $q = 3$) and inclination (panel (d), $i = 30^\circ$) while keeping all other parameters constant, the RV variations, particularly the amplitude (ΔRV) change significantly.** Clearly, the measured ΔRV is highly dependent on these parameters. To compound this problem further, the RV variation changes in an eccentric orbit and also depends on ω and Ω . This implies that the time-base and sampling of the campaign have to be considered along with the aforementioned parameters when attempting to correct for observational biases.

Comparing panels (a) and (b) in Fig. 1.8 shows that random sampling over a few epochs prefers the detection of shorter period systems as they exhibit larger RV amplitudes. Panel (c) shows a smaller ΔRV for the WR star with a low-mass companions. The effect of this bias can be seen in VDH01 and the GCWR, as all of the currently known companions of Galactic WR stars are OB stars (except Cyg-X3, which is thought to be a black hole). This is understandable, because a WR star with a low-mass companion at a low inclination would be hard to detect, especially if the WR star has significant line-profile variability. Moreover, the detection of edge-on over face-on systems are preferred (Fig. 1.8, panel (a) versus (d)) as the Doppler shift in the line-of-sight is larger. Another potential bias that we discuss in Chapters 4 and 5 is that of the sample selection relating to the brightness of WR stars. As mentioned before, a fair fraction of WR stars exhibit strong line-profile variability. This can significantly affect the RV measurements, which is why accounting for this while deriving the uncertainties on the RVs is crucial to account for this bias. Another uncertainty on the RV to account for is from the data-reduction and processing, along with the mathematical technique used to measure RVs. This is addressed in Chapter 3.

1.3 Motivation and outline of this thesis

There are numerous uncertainties that plague our understanding of massive-star evolution. Some of them include rotation, internal mixing, mass loss, binary interaction and magnetic fields. Handling all of this in a one-dimensional stellar evolution code only compounds the problem, as a deviation from spherical symmetry can be reached with more than one of the above parameters. As it is the post-main sequence phase of stellar evolution, the WR phase acts like a magnifying glass, highlighting the effects of these uncertainties. Studying the population of WR stars in a statistically significant manner provide an anchor point for stellar evolution models, using which we can work towards mitigating the shortcomings in our current knowledge. Additionally, WR stars are also progenitors of black holes, either via core-collapse SN or through

direct collapse. The mass, multiplicity fraction and orbital configurations of WR stars directly give us insight on the future population of GW progenitors. Moreover, WR stars are suspected to be progenitors of GRBs, and the multiplicity properties of the WR population might help in understanding more about this phenomenon.

With this in mind, the following questions are of interest to us: what fraction of Galactic WR stars reside in binaries? What are the orbital configurations of these binaries? Do they give us insight into past events of binary interaction from the main-sequence phase (e.g. mergers, ejections)? Is the observed discrepancy in the orbital period distribution between WN and WC stars real, or is it simply a bias? What is the effect of multiplicity on the Conti scenario?

To attempt and constrain the intrinsic multiplicity properties of Galactic WR stars, we undertook a homogeneous spectroscopic monitoring campaign using the HERMES spectrograph mounted on the Mercator telescope on La Palma. From 2017-2021, we monitored 39 northern WR stars and obtained at least six epochs, and calculated the observed multiplicity fraction. We then corrected this fraction for observational biases and obtained the intrinsic multiplicity properties of the Galactic WR population.

In Chapter 2, we introduce the instrument and data reduction techniques used in a homogeneous fashion. We developed an additional reduction scheme on top of the standard HERMES pipeline to correct for the instrumental response, and used continuum models to normalise the spectra.

In Chapter 3, we focus on the pilot study of 12 WC stars, where the methods in Chapter 2 were applied. We use cross-correlation to measure RVs, after which we identify the observed binary fraction. We then use Monte-Carlo simulations to quantify the detection probability in our sample across the relevant parameter space, and apply a correction for observational biases.

In Chapter 4 we apply the above techniques to analyse a sample of 16 WNE stars. We develop a Bayesian framework around Monte-Carlo simulations, using which we calculated the power-law index, the upper and lower bounds of the period distribution along with the intrinsic multiplicity fraction of the WNE population. We re-visited the WC population and used these improved simulations to confirm what is observed in the literature, i.e. a lack of short period binaries. We compare what is obtained to main sequence O stars and discuss possible evolutionary consequences.

In Chapter 5 we round off our sample by analysing 11 WNL stars. We discover that the multiplicity properties are similar to those of the WNE population and run simulations for the combined WN population. After reconstructing the period distribution, we confirm that the addition of the WNL sample further strengthens our conclusions. We discuss possible binary evolutionary channels that could link the O, WN and WC populations and reproduce their multiplicity properties. Finally, Chapter 6 summarises the work completed in this thesis and discusses future work.

Chapter 2

Data reduction

The work presented in this chapter is part of a larger study:

MELCHIORS: The Mercator Library of High Resolution Stellar Spectroscopy

P. Royer, **K. Dsilva**, T. Merle, S. Sekaran, H. Van Winckel, Y. Frémat, M. Laverick, M. Abdul Masih, B. Acke, M.L. Alonso, S. Bandhu Mahoto, P. Beck, N. Behara, S. Bloemen, B. Buyschaert, N. Cox, J. Deboscher, P. De Cat, P. Degroote, R. De Nutte, K. De Smedt, B. de Vries, L. Dumortier, A. Escorza Santos, K. Exter, S. Goriely, N. Gorlova, H. Hensberghe, M. Hillen, W. Homan, M. Hrudkova, D. Kamath, R. Karjalainen, P. Lampens, R. Lombaert, P. Marcos Arenal, J. Menu, F. Merges, E. Moraweji, P. Nemeth, P. Neyskens, R. Ostensen, P. Papics, J. Perez, S. Prins, A. Samadi, H. Sana, A. Sans Fuentes, S. Scaringi, V. Schmid, L. Siess, C. Siopis, K. Smolders, S. Sodor, A. Thoul, A. Tkachenko, S. Triana, B. Vandenbussche, M. Van der Swaelmen, M. Van de Sande, G. Van De Steene, S. Van Eck, P. van Hoof, A.J. Van Marle, T. Van Reeth, L. Vermeylen, D. Volpi, J. Vos and C. Waelkens

Soon to be submitted to Astronomy & Astrophysics

Author contributions: The campaign and the assembly of the library was led by P. Royer. K. Dsilva developed the telluric correction and implemented the instrumental response correction for the HERMES pipeline, with guidance and regular discussions with H. Sana, P. Royer and H. Van Winckel. S. Sekaran and T. Merle obtained models for the spectrophotometric standards. All other co-authors conducted a significant amount of observations for the spectral library with the HERMES spectrograph.

2.1 Introduction

The spectroscopic data used in this thesis was obtained with the High Efficiency, high-Resolution Mercator Echelle Spectrograph (HERMES, [Raskin et al. 2011](#)). As WR stars do not have any continuum, normalising their spectra is challenging, and is usually possible with stellar model atmospheres. However, the pipeline of HERMES does not provide flux-calibrated spectra and hence the shape of the delivered scientific spectra are heavily impacted by that of the response curve of the instrument. In order to circumvent this, we developed a methodology to correct for the instrumental response. The resulting spectrum is a scaled version of the spectral energy distribution, with a contribution from interstellar reddening. In this chapter, the data reduction process is explained in detail.

2.1.1 Instrumental response function

At the entrance of the telescope, any stellar spectrum S can be decomposed into a number of factors:

$$S = C \cdot N \cdot A^e \cdot A^m \quad (2.1)$$

where A^e is the atmospheric extinction, A^m the molecular absorption by the Earth's atmosphere, and $S^0 = C \cdot N$ is the stellar spectrum. Finally C represents the stellar continuum, i.e. the ratio between S^0 and the normalised spectrum N . The spectrum S contains the effect of the interstellar absorption, which is not corrected for and is consequently included in C .

To achieve this, we considered three types of measurements: observations of scientific targets (f_{obj}), observations of spectrophotometric calibrators (f_{cal}), and flat field exposures (ff_{raw}). After the subtraction of the electronic offset, these can be expressed as:

$$f_{obj} = S_{OBJ} \cdot \mathfrak{R}' \quad (2.2)$$

$$f_{cal} = S_{CAL} \cdot \mathfrak{R}' \quad (2.3)$$

$$ff_{raw} = FF_{SED} \cdot \mathfrak{R}' \quad (2.4)$$

where FF_{SED} expresses the spectral energy distribution (SED) of the flat-field signal, imposed by the spectrum of the lamps and filters used for these measurements. The instrumental response is defined by $\mathfrak{R}' = \mathfrak{R} \cdot B \cdot P$, in which B represents the blaze function driving the response inside every order of the echelle spectrometer, P is the pixel response non uniformity, and \mathfrak{R} (hereafter called the response) captures the remaining instrumental effects (quantum efficiency of the detector, transmission and reflection of the optical elements, etc.).

The response \mathfrak{R} is wavelength and time dependent. The wavelength dependence describes the relative spectral response function and the time dependence takes into account possible variations of the environmental conditions (temperature, atmospheric pressure and humidity), instrument aging and in our case residuals with respect to the average atmospheric extinction (see below). Formally, the response encapsulates the flux calibration coefficient, which is disregarded here as HERMES spectra are not calibrated in flux.

The flat-field exposures are usually acquired at the beginning and at the end of the night. The spectrophotometric calibrators are celestial targets whose absolute spectra are known from accurate modelling. One such object was observed every night whenever possible. We used them to determine and correct for the instrumental response (Sect. 2.2.2).

2.2 HERMES Pipeline

The raw 2-D echelle spectra are first processed with the standard HERMES pipeline, which includes bias correction, background subtraction, flat-field correction, cosmic-ray clipping and, order merging (Raskin et al. 2011). The flat-field correction is a mandatory step to remove the pixel response non uniformity, but also, prior to order merging, to remove the effect of the blaze function in every order. Dividing by the flat-field is nevertheless artificially imposing the shape of $1/FF_{SED}$ onto every spectrum thus corrected. The output of the pipeline hence consists in 1-D spectra still affected by the effects of the Earth’s atmosphere and the newly introduced shape of the flat-field.

Table 2.1: Wavelength ranges and the respective molecules included in the fitting process with Molecfit.

Wavelength start (Å)	Wavelength end (Å)	Molecule
6274	6324	O ₂
6850	7074	O ₂ (B band)
7227	7269	H ₂ O
7589	7714	O ₂ (A band)
8101	8344	H ₂ O
8940	8971	H ₂ O

2.2.1 Atmospheric extinction and telluric correction

To correct for the atmospheric extinction A^e , a wavelength and airmass-dependent atmospheric correction is applied following tabulated values for the Roque de Los

Muchachos Observatory on the island of La Palma¹. This correction is an average: it slightly varies in cases where the observations were carried out under conditions of thin clouds and also strongly depends on the nature and quantity of dust along the atmospheric line-of-sight. However, the spectra obtained for the RV monitoring campaign were obtained on clear nights, and so this does not seem to be a problem.

To correct for the telluric line absorption A^m , we use the publicly available tool Molecfit (Smette et al. 2015; Kausch et al. 2015). By combining essential input from the Mercator meteo-station with a molecular line database and a radiative transfer code, Molecfit models the instrument line spread function and atmospheric content at the time of the observation. The wavelength ranges and molecules included in the fitting procedure are listed in Table 2.1. For every region included in the fit, the continuum is estimated locally using a first order polynomial. Molecfit also corrects for any minor wavelength shifts by fitting the wavelength solution with a second order Chebyshev polynomial.

After correction, the spectra show residuals of $\sim 5\%$ (Fig. 2.1) of the continuum in the telluric bands, with the exception of the saturated lines. While fitting saturated lines, the division of two numbers close to zero often results in large residuals (the oxygen band around 7600 Å, is often impacted this way). In the region after 8950 Å we observe residuals due to a small imperfection of the wavelength calibration solution at the red edge of the spectra (Fig. 2.2).

2.2.2 Response correction

At this stage, the spectra can be expressed as:

$$f_{obj}^{0,FF} = \frac{S_{OBJ}^0 \cdot \mathfrak{R}}{ff} \quad (2.5)$$

$$f_{cal}^{0,FF} = \frac{S_{CAL}^0 \cdot \mathfrak{R}}{ff} \quad (2.6)$$

where "FF" and "0" indicate that the flat-field and atmospheric corrections have been applied and $ff \triangleq FF_{SED} \cdot \mathfrak{R}$.

If we define an effective instrumental response $\hat{\mathfrak{R}}$ combining the system response with the effect of the flat-field

$$\hat{\mathfrak{R}} \triangleq \frac{\mathfrak{R}}{ff} = \frac{f_{cal}^{0,FF}}{S_{CAL}^0} \quad (2.7)$$

¹https://www.ing.iac.es/Astronomy/observing/manuals/html_manuals/general/obs_guide/node293.html

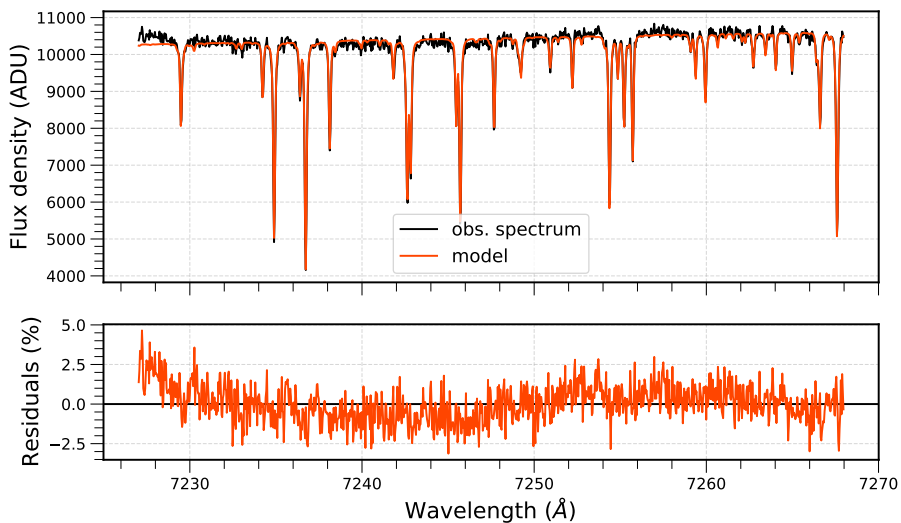


Figure 2.1: Telluric correction of WR 136 (WN6b(h)) in the region 7227 Å to 7269 Å, showing residuals less than 5%.

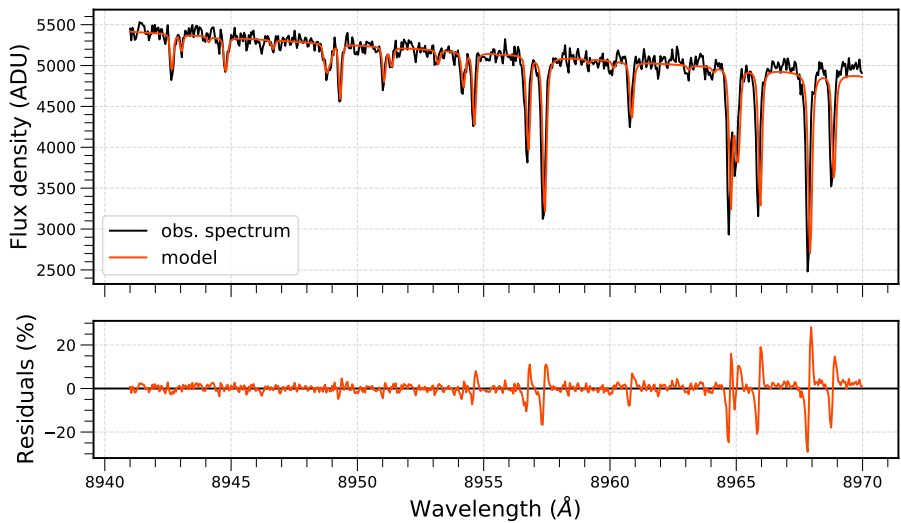


Figure 2.2: Telluric correction of WR 136 (WN6b(h)) in the region 8940 Å to 8970 Å. The uncertain wavelength calibration causes residuals of the order 20%.

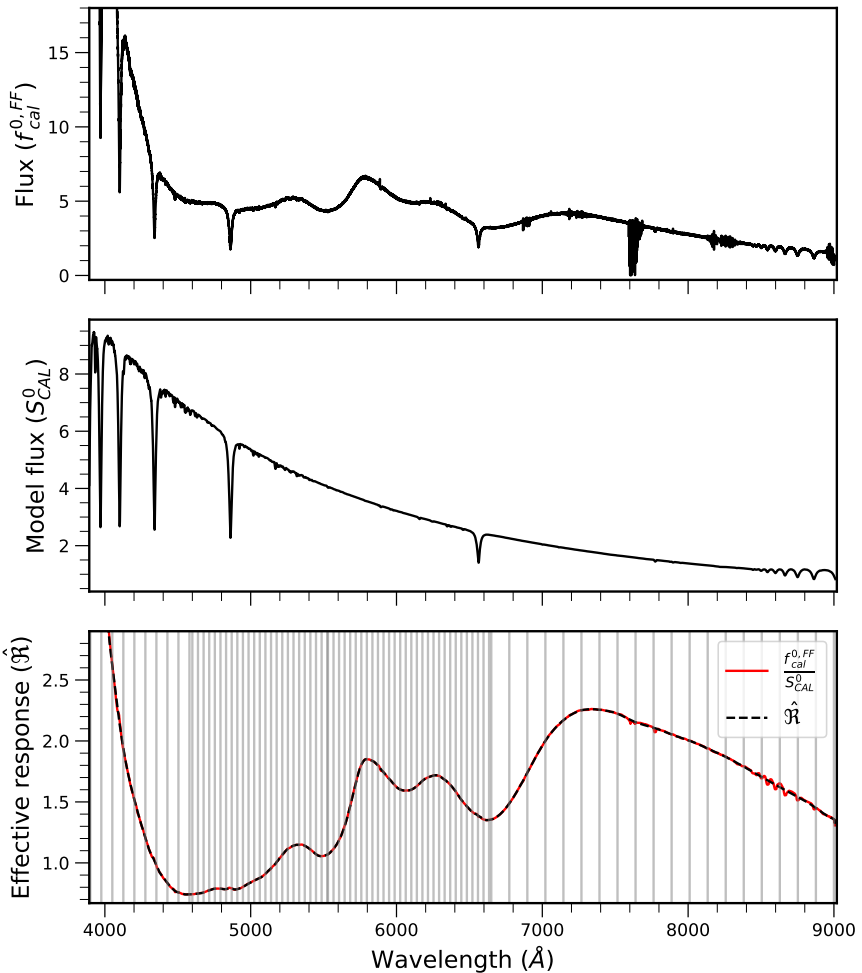


Figure 2.3: The derivation of the effective response for a night (Eq. 2.7). The spectrophotometric calibrator star used in this example is HD 42818. **Top:** the spectrum corrected for flat-field and atmospheric effects ($f_{cal}^{0,FF}$). **Middle:** Model SED used to derive the response (S_{CAL}^0). **Bottom:** The derived effective response ($\hat{\mathfrak{R}}$) in red which is fit with a spline in black. The knot points used to fit the spline are shown with vertical grey lines.

we can express the final spectrum, corrected from the instrumental response, the effects induced by the flat-field correction and the effects from the atmosphere as:

$$S_{OBJ}^0 = \frac{f_{obj}^{0,FF}}{\hat{\mathfrak{R}}} \quad (2.8)$$

One spectrophotometric standard was observed every night when possible as part of the normal calibration set of HERMES, aiming at a daily determination of $\hat{\mathcal{R}}$. These targets were carefully selected for this purpose: they are well documented in the literature, and have reliable models established by a series of independent publications. All of these targets were modelled with the LTE model-atmosphere code gssp ([Tkachenko 2015](#)). gssp generates synthetic spectra using the SYNTHV radiative transfer code ([Tsymbal 1996](#)) combined with a grid of atmospheric models from the LLMODELS code ([Shulyak et al. 2004](#)). These synthetic spectra are then fitted to the highest-SNR observed spectrum for each star in the HERMES archive. The atmospheric parameters T_{eff} , $\log g$, projected rotational velocity ($v \sin i$), microturbulent velocity (v_{mic}) and the metallicity ([M/H]) and their corresponding uncertainties were then determined from the distribution of χ^2 values of the fit of each synthetic spectrum to the observed spectrum. We then used the closest parameters in the LLMODELS grid to our best-fitting values as the input to generate the spectral energy distribution (SED) models of our calibrators.

The result of the division of the calibrator spectrum by the model in Eq. 2.7 is first smoothed with a median filter and then fit with a spline in order to produce a smooth, yet accurate representation of the effective response ($\hat{\mathcal{R}}$) before injecting it in Eq. 2.8, hence avoiding the introduction of noise resulting from the observation of the calibration star or local residuals from its model in the corrected spectra. The density of knot points used to fit the spline are chosen locally depending on the complexity of the response (bottom panel of Fig. 2.3). All spectra obtained over the corresponding night are then divided by this response, resulting in a reliable representation of the continuum shape. In a few cases where a spectrophotometric standard was not observed, the effective response derived for the nearest night in time was then used instead. It is important to note that the shape of the flat-field affects the effective response. This change in the FF_{SED} depends on the temperature of the lamps, which is not monitored. Hence, we have no control over the applicability of a given response (derived from another night) to a given night. As a result, a few of the response corrections are inaccurate on such nights, leaving characteristic low-frequency signatures in the spectra.

The output of the response correction are HERMES spectra whose shapes represent the star's SED. Although the spectra are not flux-calibrated, we are able to use continuum models to normalise these spectra. In the Chapters 3, 4 and 5, we will use this technique to reduce all of our observations of WR stars. Furthermore, the calibration techniques presented in this chapter have been deployed and applied to the entire HERMES archive (3258 spectra, 478 nights) in the context of an upcoming data release of the Mercator Library of High-Resolution Stellar Spectroscopy (Royer, Dsilva et. al in prep).

Chapter 3

Multiplicity properties of the carbon-rich Wolf-Rayet population

The work presented in this chapter is based on:

A spectroscopic multiplicity survey of Galactic Wolf-Rayet stars: I. The northern WC sequence

K. Dsilva, T. Shenar, H. Sana and P. Marchant

Originally published as:

ASTRONOMY AND ASTROPHYSICS, 641, A26 (2020)

Author contributions: K. Dsilva performed a majority of the analysis in this chapter with the guidance of H. Sana and T. Shenar. The Monte-Carlo simulations were run by H. Sana. T. Shenar assisted with the line identifications for the cross-correlation. P. Marchant assisted with the evolutionary interpretations of the presented results. All the authors provided feedback on the text, which was written by K. Dsilva.

Original abstract:

It is now well established that the majority of massive stars reside in multiple systems. However, the effect of multiplicity is not sufficiently understood, resulting in a plethora of uncertainties about the end stages of massive-star evolution. In order to investigate these uncertainties, it is useful to study massive stars just before their demise. Classical Wolf-Rayet stars represent the final end stages of stars at the upper-mass end. The multiplicity fraction of these stars was reported to be ~ 0.4 in the Galaxy but no correction for observational biases has been attempted.

The aim of this study is to conduct a homogeneous radial-velocity survey of a magnitude-limited ($V \leq 12$) sample of Galactic Wolf-Rayet stars to derive their bias-corrected multiplicity properties. The present paper focuses on 12 northern Galactic carbon-rich (WC) Wolf-Rayet stars observable with the 1.2 m Mercator telescope on the island of La Palma.

We homogeneously measured relative radial velocities (RVs) for carbon-rich Wolf-Rayet stars using cross-correlation. Variations in the derived RVs were used to flag binary candidates. We investigated probable orbital configurations and provide a first correction of observational biases through Monte-Carlo simulations.

Of the 12 northern Galactic WC stars in our sample, seven show peak-to-peak RV variations larger than 10 km s^{-1} , which we adopt as our detection threshold. This results in an observed spectroscopic multiplicity fraction of 0.58 with a binomial error of 0.14. In our campaign, we find a clear lack of short-period ($P < \sim 100 \text{ d}$), indicating that a large number of Galactic WC binaries likely reside in long-period systems. Finally, our simulations show that at the 10% significance level, the intrinsic multiplicity fraction of the Galactic WC population is at least 0.72.

3.1 Introduction

The multiplicity of WR stars serves as an important observational constraint in understanding binary evolution, as well as the properties immediately prior to core-collapse (Sect. 1.1). To achieve this, a homogeneous observational survey of WR stars is crucial to properly correct for observational biases (Sect. 1.2.3). With this in mind, the WR RV monitoring campaign began in 2017 using the HERMES spectrograph mounted on the 1.2 m Flemish Mercator Telescope on La Palma (Sect. 1.3). HERMES covers the optical wavelength range from 3800 \AA to 9000 \AA , with a spectral resolving power of $R \sim 85\,000$. In this chapter, we analyse a sample of 12 WC stars to demonstrate

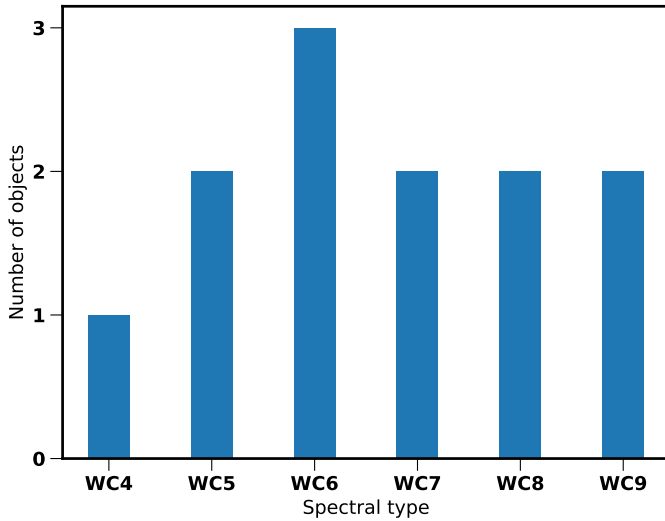


Figure 3.1: Spectral type distribution of the stars in our sample.

that the combination of high-resolution with good S/N over a long period of time results in a powerful tool to search for binarity.

3.2 Overview of the sample and data reduction

3.2.1 The sample

Our sample was selected from the GCWR and includes all WC stars with $V \leq 12$ and declination $\delta \geq -30^\circ$. For objects with missing V band magnitudes, narrow-band v magnitudes (Smith 1968a; Massey 1984) were used with the condition $v \leq 13$. This resulted in a final sample of 12 WC stars. The spectral type distribution among our sample is shown in Fig. 3.1.

3.2.2 Observations

For all but one of the 12 objects, at least six epochs were obtained over the course of 15 months. Table 3.1 gives an overview of the campaign (including archival HERMES data). The number of epochs for WR 137 is larger because we obtained an additional 16 epochs with a high cadence over 15 days, with three observations over the same

Table 3.1: Sample of WC stars in the RV monitoring campaign with the number of spectra, time coverage, and average S/N per resolution element at 5200 Å.

WR#	Spectra	Time coverage (d)	S/N @ 5200 Å
4	22	891	62
5	7	718	59
111	8	742	157
113	9	728	116
117	4	488	7
119	7	821	32
135	16	2660	166
137	28	2654	175
140	13	2681	203
143	6	76	33
146	8	847	8
154	4	24	48

night to investigate the effect of short-term atmospheric or wind variability on the measured RVs (Sect. 3.3.3).

3.2.3 Data reduction and normalisation

As mentioned in Sect. 2.2.2, the spectra are first processed by the HERMES pipeline and then corrected for the instrumental response. However, the spectra are still affected by interstellar reddening. In order to achieve a normalisation procedure that is homogeneous over multiple epochs, we developed an algorithm that corrects for these effects. This minimises the effect of variable normalisation on the RV measurements.

To normalise these spectra, pseudo-continuum regions were chosen based on normalised model spectra for WC stars from the Potsdam Wolf-Rayet code (PoWR; Gräfener et al. 2002; Hamann & Gräfener 2003; Sander et al. 2012). Two continuum regions were adopted: in the red, around 8100 Å, and in the blue, around 5200 Å. By anchoring the respective continuum models to the red point and then reddening them based on Fitzpatrick (2004a) we fit the slope and normalise the spectra. For this purpose, we used an R_V value of 3.1, the average value for the Galaxy. The various steps in the data handling are illustrated in Fig. 3.2. We note that we only rely on the aforementioned reddening law to obtain a homogeneous normalisation process and therefore refrain from providing the reddening values obtained through the continuum-fitting procedure.

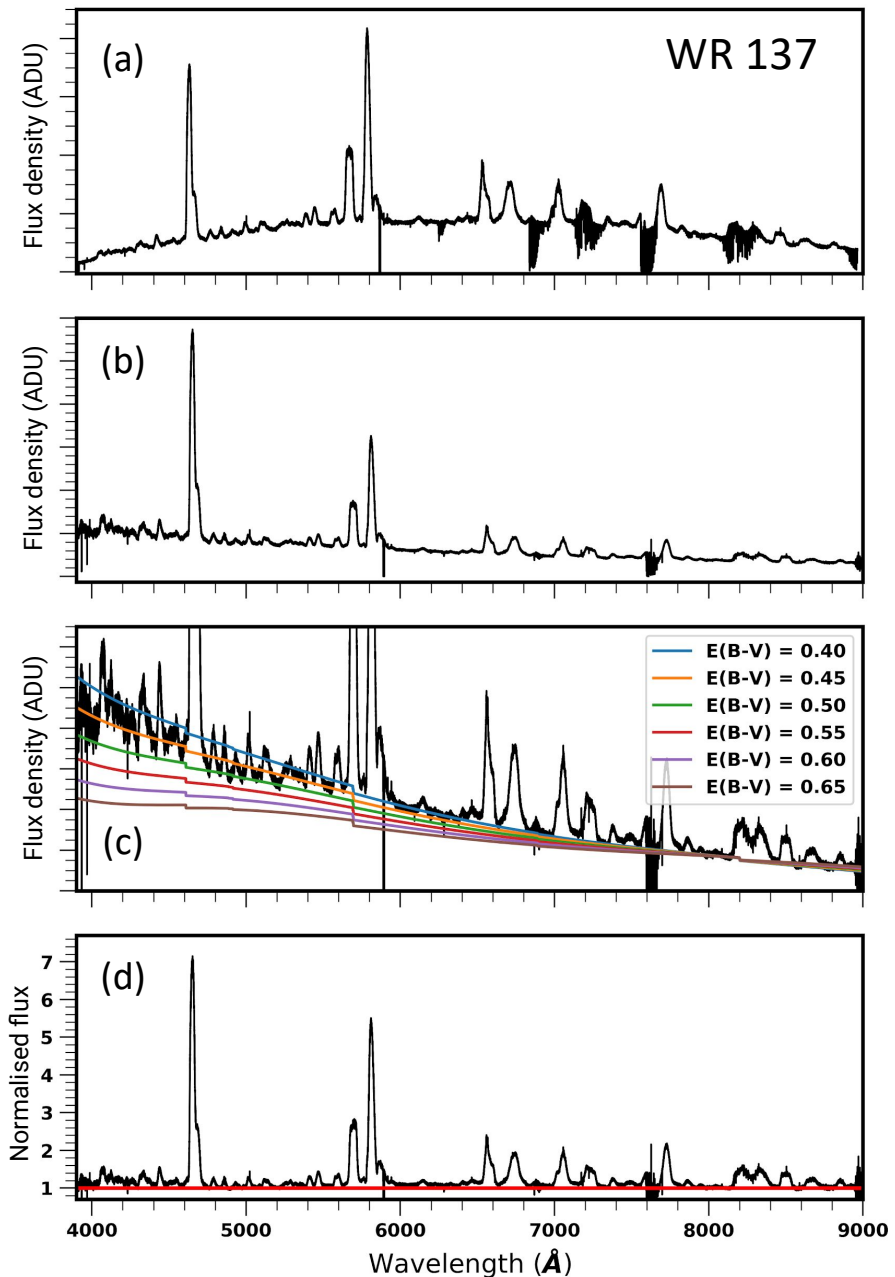


Figure 3.2: Main steps in our data reduction process. From top to bottom: (a) Flat-field corrected spectrum produced by the HERMES pipeline. (b) Spectrum corrected for the instrumental response function and telluric contamination. (c) Continuum flux models from PoWR to the pseudo-continuum region around 5200 Å for different values of $E(B - V)$. (d) Resulting normalised spectrum.

3.3 Radial velocity determination

In order to derive RVs for broad WR emission lines in a systematic manner, one needs a method that can be applied to most, if not all, of the objects in our sample and that yields meaningful errors. The uncertainty on each measurement will have contributions from different sources: statistical (based on the method and S/N), systematic (instrumental and normalisation), and intrinsic (variability in spectral lines). It is important to have reliable estimates of the uncertainties affecting the RV measurements as these will directly propagate into the observational bias correction. For binary systems, an upper limit on the RV measurement uncertainties can be estimated by measuring the dispersion in the residuals after fitting an orbit. However, the very long periods involved do not allow us to use this.

In this study, we focus solely on RV measurements of WR stars. In the case of SB2 binaries (i.e. double-lined spectroscopic binaries), it is, in principle, also possible to measure the RVs of the secondary star (typically an OB-type star). However, as the goal of our current study is binary detection rather than orbital analysis, there is little advantage in doing so. The WR component, being typically the lighter component, would exhibit larger RV amplitudes than its OB-type companion. Moreover, applying additional binary-criteria to SB2 binaries would require us to introduce non-trivial adjustments to our bias correction (see Sect. 3.4.3).

In all cases, the estimation of uncertainties depends on the method used to measure the RVs. In the case of Gaussian fitting, the errors on the RV measurements are usually derived using the co-variance matrix of the least-squares fit. Cross-correlation relies on applying a peak-finding algorithm to the cross-correlation function (CCF), which can be a Gaussian, Lorentzian, parabola or, a sinc function (e.g. Tody 1993). Another approach is to find the bisector of the CCF. The errors are derived based on the width, number of pixels, height of the CCF peak, and the anti-symmetric noise (Tonry & Davis 1979). When measured for WR stars with low-resolution spectra, the errors are magnified by the low number of pixels around a broad CCF peak. In this work, we use a different statistical formulation for the CCF that represents it as a log-likelihood function. The latter is then maximised and fit with a parabola. This is explained in detail below.

3.3.1 Cross-correlation

The method that we used for the cross-correlation is based on Zucker (2003). The method, assumptions and limitations are briefly discussed here. For a more thorough derivation we refer to Zucker (2003). The observed spectrum is denoted by $f(n)$ and is assumed to be Doppler shifted with respect to the ‘template’ of zero-shift, denoted by $g(n)$. Both the spectrum and the template are described as a function of pixel, n , such

that a Doppler shift results in a uniform, linear shift in the spectrum (Tonry & Davis 1979).

In this work, the observed spectrum is assumed to be reproducible by scaling the template with a constant (a_0) and shifting it by a certain number of pixels (p_0). The noise in the observed spectrum is assumed to be Gaussian with a fixed standard deviation (σ_0), so that:

$$f(n) = a_0 g(n - p_0) + d_n, \text{ with} \quad (3.1)$$

$$d_n \sim N(0, \sigma^2). \quad (3.2)$$

The spectra (or specific masks) are assumed to be ‘continuum-subtracted’, such that they have a zero mean:

$$\sum_n f(n) = 0, \text{ and} \quad (3.3)$$

$$\sum_n g(n) = 0. \quad (3.4)$$

The last assumption that the number of pixels, N , is constant breaks down. For very small velocity shifts, the edge effects are negligible. However, for velocities of the order of 1000 km s^{-1} , the assumption is not applicable and hence, we use a rolling function to carry out the shift in pixels. This does not have any impact on the computation of the CCF or the determination of the peak.

In order to express the CCF in terms of a log-likelihood function, for a given shift of p pixels we first define the cross-covariance function,

$$R(p) = \frac{1}{N} \sum_n f(n)g(n - p). \quad (3.5)$$

The standard deviation of the spectrum (s_f) and template (s_g) can be expressed as

$$s_f^2 = \frac{1}{N} \sum_n f^2(n), \text{ and} \quad (3.6)$$

$$s_g^2 = \frac{1}{N} \sum_n g^2(n). \quad (3.7)$$

Following this, we define the CCF of f and g as

$$C(p) = \frac{R(p)}{s_f s_g}. \quad (3.8)$$

This CCF can be written in the form of a log-likelihood function. We denote a shift \hat{p} that maximises the CCF. The errors can then be derived from the covariance matrix following maximum log-likelihood theory and can be expressed as

$$\sigma_p^2 = - \left[N \frac{C''(\hat{p})}{C(\hat{p})} \frac{C^2(\hat{p})}{1 - C^2(\hat{p})} \right]^{-1}, \quad (3.9)$$

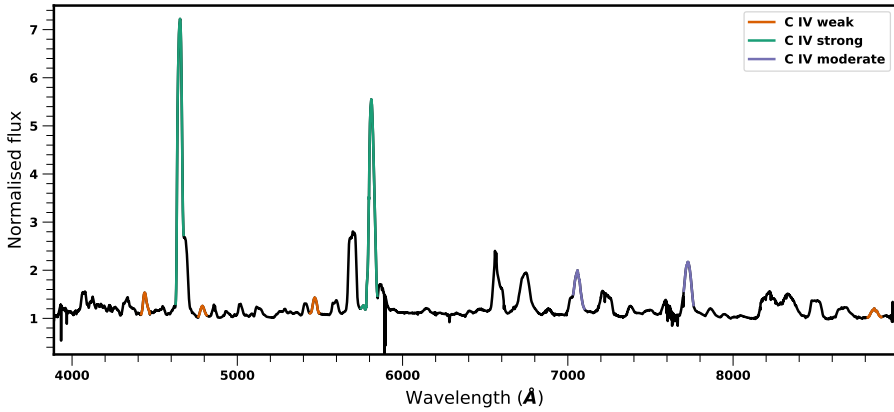


Figure 3.3: Spectrum of WR 137, rebinned for clarity, with different masks of C iv indicated (see legend). This process is repeated for all other ions, producing a plethora of masks.

where $C''(p)$ is the second derivative of the CCF. Equation 3.9 shows that the errors depend on the number of pixels N , the sharpness of the peak $C''(\hat{p})/C(\hat{p})$ and the line S/N ratio $C^2(\hat{p})/(1 - C^2(\hat{p}))$.

The success of the cross-correlation depends on the accuracy and stability of the template. This is due to the fact that the template is implicitly assumed to represent the data accurately. In practice, the template is chosen to be the observations with the highest S/N. A parabola is fit to the top of the CCF in order to determine the peak and the related derivatives. The errors from the least-squares fitting of the parabola agree with those derived from Eq. 3.9, giving confidence in the validity of the method. Once the RVs and measurement uncertainties are derived, a weighted average of the shifted spectra is used to derive a co-added spectrum that has a higher S/N. This is then used as a template to re-derive the relative RVs and, thus, in an iterative fashion, an ideal mask and a final measurement are converged upon. We note that the RVs derived are relative to a particular observation in time, and that the velocities measured are, by no means, absolute values. In order to compare with those in the literature or to the rest frame, a uniform shift must be imposed.

3.3.2 Mask selection

After addressing the choice of the template, the question of which spectral lines or wavelength ranges (henceforth ‘masks’) to be used for the RV measurements arises. Most traditional methods of measuring RVs are applied to the strongest lines, as they

contain the most signal. On the other hand, different lines originate in different ions and form in different regions in the wind. Therefore, by comparing the RVs measured using different sets of lines, we can both probe different parts of the wind as well as identify the most reliable mask to represent the motion of the star.

However, with high-resolution and good S/N, weak lines also contain significant amounts of information that can be used. As the WR spectra contains much broader (and stronger) spectral features, using the entire spectrum in the cross-correlation process can mitigate the problem of contamination from the secondary ([David-Uraz et al. 2012](#)). To investigate which masks are the most appropriate and if individual lines are better than the full spectrum, RVs are first measured using a variety of masks. These masks are created by selecting lines of different strengths and different ions, as well as with the full spectrum.

For WC stars, most lines originate from carbon (C II, C III and C IV), oxygen (O II, O III, O V, O VI) and helium (He I, He II). Naturally, the strength of the lines of various ions depends on the temperature (among other things) of the WR star, and are identified star-by-star using PoWR models with parameters from [Sander et al. 2012](#). For each star in the sample, this results in ‘strong’, ‘moderate’ and ‘weak’ masks for different ions. An example of C IV masks for WR 137 is shown in Fig. 3.3.

The motivation for using lines of the same ion in the same mask is straightforward, while that for using only strong or weak lines is a bit more complex. Lines of the same ion are thought to have formed in the same region of the wind and should thus provide the same RV measurement. Moreover, it is useful to use only strong lines to measure RVs in order to compare the results of this work to what is available in the literature. The errors from the CCF (Eq. 3.9), additionally, depend inversely on the S/N in the line, which is higher for strong lines. However, weak lines of highly ionised ions are formed closer to the surface and thus are thought to be less susceptible to wind variability, making them a logical choice for a mask. It is further essential to isolate and quantify the effects of wind variability on WR spectra. Once this is accounted for, we can decide which masks are the most appropriate to detect genuine RV variability. This is addressed in the following section.

3.3.3 Uncertainties from systematic sources and wind-variability: A proto-study of the binary WR 137

In this section, we investigate the effect of systematic sources and wind variability on RV measurements. To understand the extent to which wind variability can affect our measured RVs, WR 137 (WC7pd + O9 V) is an ideal candidate to examine. It is a well-studied long-period binary system with an orbital period of 13.05 years ([Lefèvre et al. 2005; Richardson et al. 2016](#)). We obtained 16 spectra over the course of 15

days during August 2019, significantly away from its periastron passage (which will happen in 2022). Therefore, we can neglect the effects of orbital motion and wind-wind collision (e.g. Lührs & Moffat 2002) due to binary interaction on the RV measurements for the purpose of this short-cadence study.

The RVs were measured as described in the previous subsection with different masks, with the additional condition that lines contaminated by absorption from the companion were excluded. The RV measurements using different masks with strong C iv lines, weak He II lines and the full spectrum can be seen in Fig. 3.4. Given RV measurements ($v_i \pm \sigma_i$), we calculated the weighted mean (μ_{RV}) and standard deviation (σ_{RV}) as:

$$w_i = \frac{1}{\sigma_i^2}, \quad (3.10)$$

$$\mu_{RV} = \frac{\sum_i w_i v_i}{\sum_i w_i}, \quad (3.11)$$

$$\sigma_{RV} = \left(\frac{\sum_i w_i (v_i - \mu_{RV})^2}{\sum_i w_i} \right)^{\frac{1}{2}}, \quad (3.12)$$

where σ_{RV} is a measure of the real dispersion in the data. Since we have already ruled out orbital and wind-wind collision effects, this dispersion can be assumed to represent the statistical error (σ_p) along with some contribution from systematic sources and wind variability (σ_w). These errors are not expected to be correlated and are therefore added in quadrature, such that they can be expressed as follows:

$$\sigma_{RV} = \sqrt{\sigma_p^2 + \sigma_w^2}. \quad (3.13)$$

Accounting for the wind variability provides us with an estimate on the effective uncertainty on the RV measurements (σ_{RV}). As σ_p is already derived, σ_w can be calculated for different ions and different line strengths, giving us a direct probe of how wind variability affects these lines. For now, however, it is sufficient to inspect σ_{RV} for different ions. Figure 3.5 depicts this comprehensively, plotting the RVs measured by each mask over the short cadence period, with σ_{RV} indicated at the bottom of the plot.

Upon examination, two observations can be made based on Fig. 3.5. The first is that for masks with He II lines, a large scatter is seen independent of the strength of the lines. The second is that across other ions, masks with strong lines perform better than those with weak lines. It is not trivial to explain these observations, as there are multiple factors that are at play for each line (e.g. oscillator strength, number populations of the particular state, line-formation region, etc.).

In order to ascertain that the statistical errors do not bias our mask selection, we calculated values for σ_w using Eq. 3.13. The results are twofold - masks with ions

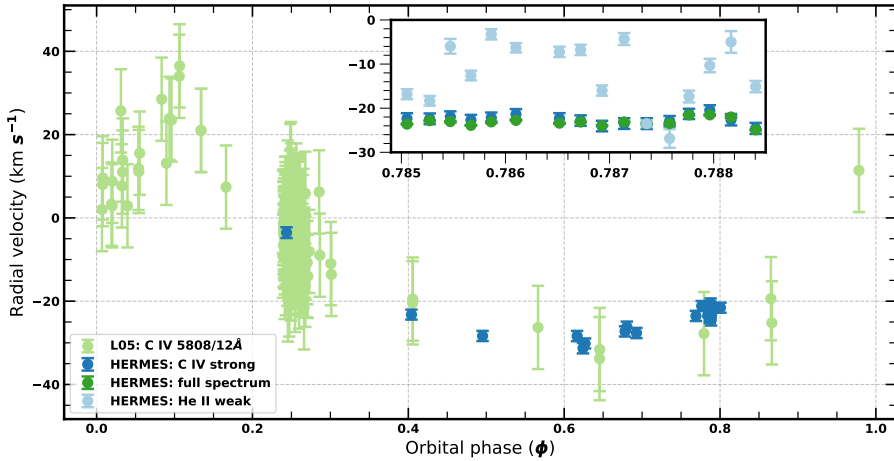


Figure 3.4: Phased RV plot for WR 137. Archival RV measurements are shown in blue and are taken from [Lefèvre et al. \(2005\)](#). The RV measurements from HERMES using the strong C iv lines are shown in red. Along with these measurements, the inset shows the short cadence measurements with the full spectrum (green) and weak He ii lines (purple). All HERMES RV measurements have been shifted by -23.5 km s^{-1} in order to convert relative RV measurements to absolute values.

of a higher ionisation state are the least affected by wind variability and strong lines are affected less than weak lines. Finally, by comparing the absolute values of σ_w in Fig. 3.5, the full spectrum mask is least affected by wind variability. For strong C iv lines, the average σ_p is larger than the corresponding value of σ_{RV} , implying that the wind variability is within the statistical error (and hence $\sigma_w = 0$). Given that the winds of all WC stars do not necessarily exhibit the same characteristics, this exercise has to be conducted for each object individually in order to select a specific ion to use. Upon inspection, diagnostic plots such as Fig. 3.5 for each object indicate that the full spectrum shows the least scatter. Considering the fact that the WR component dominates the spectrum for all of our objects, we decided to use the full spectrum to measure RVs.

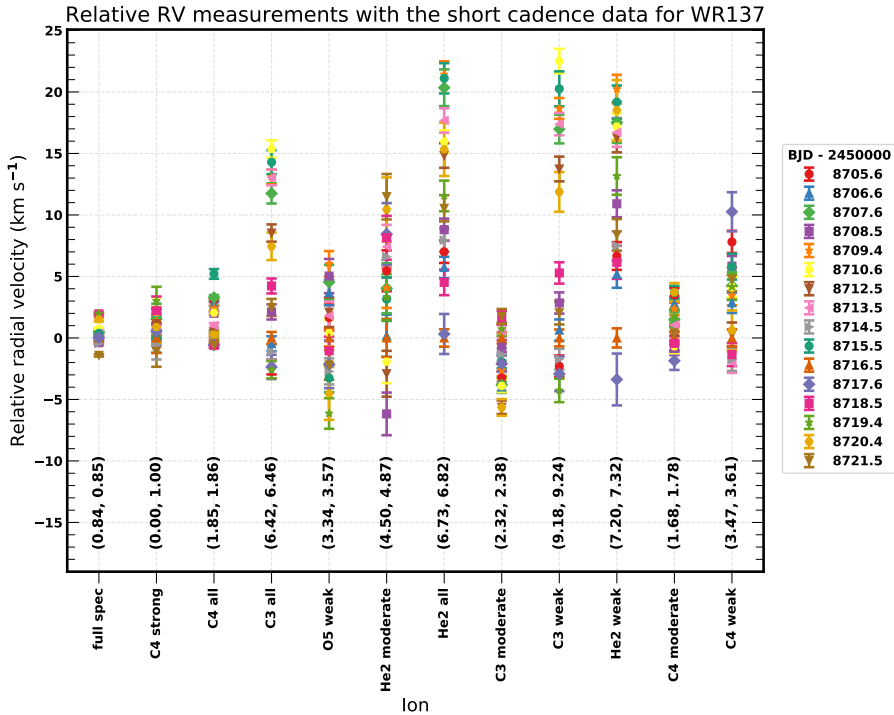


Figure 3.5: RV measurements for WR 137 during the short cadence study. At the bottom of the plot are the values of (σ_w, σ_{RV}) (km s^{-1}) for each mask. It is observed that the helium lines (and weak lines in general) have large dispersions. The masks least affected by wind variability are ‘full spec’, ‘C4 strong’, ‘C4 moderate’, and ‘C4 all’ (determined by their values of σ_w).

3.4 Results and discussion

3.4.1 Observed spectroscopic binary fraction

For all the objects in our sample, RVs were measured using multiple masks. The tests described in the previous section reveal that the measurements using the full spectrum are the most reliable and we adopt those in the following section. These are given in Appendix A.2. To identify objects with significant RV variation, we look at the maximum RV variation for each star, given by

$$\Delta RV = \max(|v_i - v_j|), \quad (3.14)$$

where v_i and v_j are the RV measurements for two epochs $i - j$ for a given star. One then imposes a minimum amplitude threshold C for RV variations computed from any individual pair of epochs to be ‘significant’.

$$\Delta\text{RV} \geq C. \quad (3.15)$$

Unlike in [Sana et al. \(2013\)](#), we do not enforce a significance criteria for each pair of RV measurements (Eq. 4 in [Sana et al. 2013](#) compared to Eq. 3.15 above). This is due to the fact that the values for σ_p are typically very small (sub-km s⁻¹) and underestimate the true error (see Sect. 3.3.3).

Given this criterion, the observed fraction of RV variable objects ($f_{\text{obs}}^{\text{WC}}$) can be calculated as a function of threshold C (Fig. 3.6). It is encouraging to see all the known binary systems group together on the right side of the plot. We can now take advantage of the fact that a subset of our sample are confirmed binaries to constrain a suitable value for C .

Two kinks can be seen, in the ranges of 5 to 10 km s⁻¹ and of 12 to 19 km s⁻¹. A threshold value of 10 km s⁻¹ leads to an observed binary fraction of $f_{\text{obs}}^{\text{WC}} = 0.58$, and that of 15 km s⁻¹ results in $f_{\text{obs}}^{\text{WC}} = 0.33$. To include the known and candidate binaries in our binary fraction, we choose the former threshold of 10 km s⁻¹.

3.4.2 Comparison with the literature

Although the magnitude-limited sample of WC stars in this study is small, the even distribution across spectral types (Fig. 3.1) omits any selection bias. With this in mind, two important conclusions can be drawn from Fig. 3.6. The first is that our value of f_{obs} is comparable to the value of 0.56 observed for main-sequence O-type stars by [Sana et al. \(2012\)](#).

The second is that there seems to be a lack of short-period ($P < 100$ d) binaries compared to the overabundance of short-period systems observed for main-sequence O-type stars ([Sana et al. 2012](#)). This is especially surprising given that the observational bias favours the detection of short-period WR binaries, which are expected to exhibit high RV amplitudes. Of the known binaries in our sample, orbits are derived only for WR 137, WR 140 and WR 113, with only WR 113 being part of a short-period binary system ($P \sim 29.7$ d). This low fraction of detected short-period binary systems (0.08) is in stark contrast to what has been found for main-sequence O-type stars.

In order to investigate the observed lack of short-period WC binary systems, we scoured the literature in order to expand our small sample. The GCWR reports 237 WC stars in

²David-Uraz

Table 3.2: Results of the RV measurements for the sample of WC stars. ΔRV (Eq. 3.14) and σ_{RV} (Eq. 3.13) are calculated in this work with the full spectrum as a mask and are used to classify the objects as binaries or single stars. We do not include the archival period of 2,4096 d for WR 4 due to the fact that we rule out short-scale variations (Appendix A.1). RV plots for the known binaries can be found in Figs. 3.4 and 3.7.

WR#	Spectral Type (GCWR)	Binary Status		Period (d)	e	ΔRV (km s $^{-1}$)	σ_{RV} (km s $^{-1}$)
		GCWR	This work				
4	WC5 + ?	SB1, no d.e.l.	binary	-	-	10.4	2.5
5	WC6	-	single	-	-	4.9	1.7
111	WC5	-	single	-	-	4.9	1.6
113	WC8d + O8-9IV	SB2	binary	29,700 \pm 0.001 ^(a)	0 (fixed) ^(a)	282.6	93.9
117	WC9d	-	single	-	-	4.5	1.5
119	WC9d	-	binary	-	-	11.0	3.2
135	WC8	-	single	-	-	4.7	1.6
137	WC7pd + O9	SB2	binary	4766 \pm 66 ^(b)	0.18 \pm 0.04 ^(b)	25.2	4.6
140	WC7pd + O4.5	SB2, VB	binary	2895.68 \pm 0.17 ^(c)	0.8996 ^{+0.0008(c)} _{-0.0008}	21.6	6.5
143	WC4 + Be	d.e.l.	binary	-	-	11.2	4.0
146	WC6 + O8	SB2, VB	binary	-	-	18.9	5.9
154	WC6	-	single	-	-	3.4	1.3

^(a) David-Uraz et al. (2012)

^(b) Lefèvre et al. (2005)

^(c) Thomas et al. (2021)

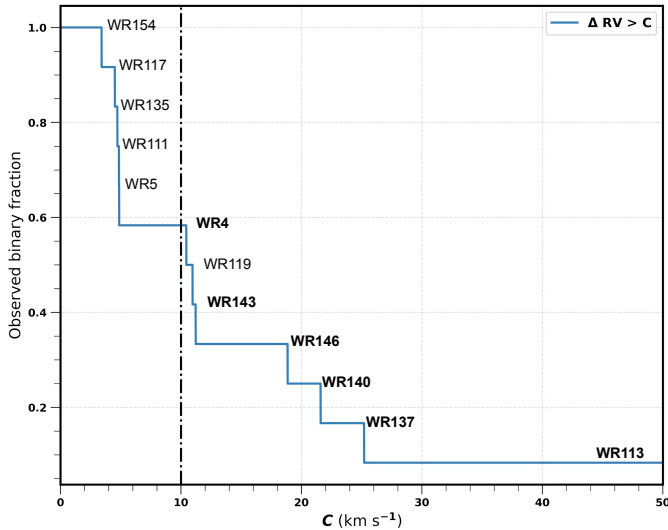


Figure 3.6: Observed binary fraction ($f_{\text{obs}}^{\text{WC}}$) as a function of the threshold C . The adopted threshold is the vertical dotted-dashed line at 10 km s^{-1} , resulting in $f_{\text{obs}}^{\text{WC}}=0.58$. The objects are labelled as and when they are classified as binaries based on ΔRV . Names in bold are known binaries.

the Galaxy, of which 87 were included in [VDH01](#). For the sake of considering WC stars that were thoroughly studied for binarity, we focus on this subset of 87 stars.

Of this subset, 37 WCs are classified as detected or probable binaries, resulting in an observed Galactic WC binary fraction of 0.41. However, this fraction is severely biased towards short-period systems. This is because historical studies were mainly sensitive to short-period systems, given typical RV measurement uncertainties of the order of $\sim 20 \text{ km s}^{-1}$. Despite the large bias towards detecting short-period systems, 15 report periods shorter than 100 d, seven of which have derived orbits. Therefore, the fraction of Galactic WC stars that are conclusively in short-period binary systems is only 0.09, which is consistent with the findings of this study.

3.4.3 Intrinsic multiplicity properties

Binary detection probability

To estimate the sensitivity domain of our survey, we perform MC simulations following the method described in [Patrick et al. \(2019\)](#). In short, for a grid of orbital period and

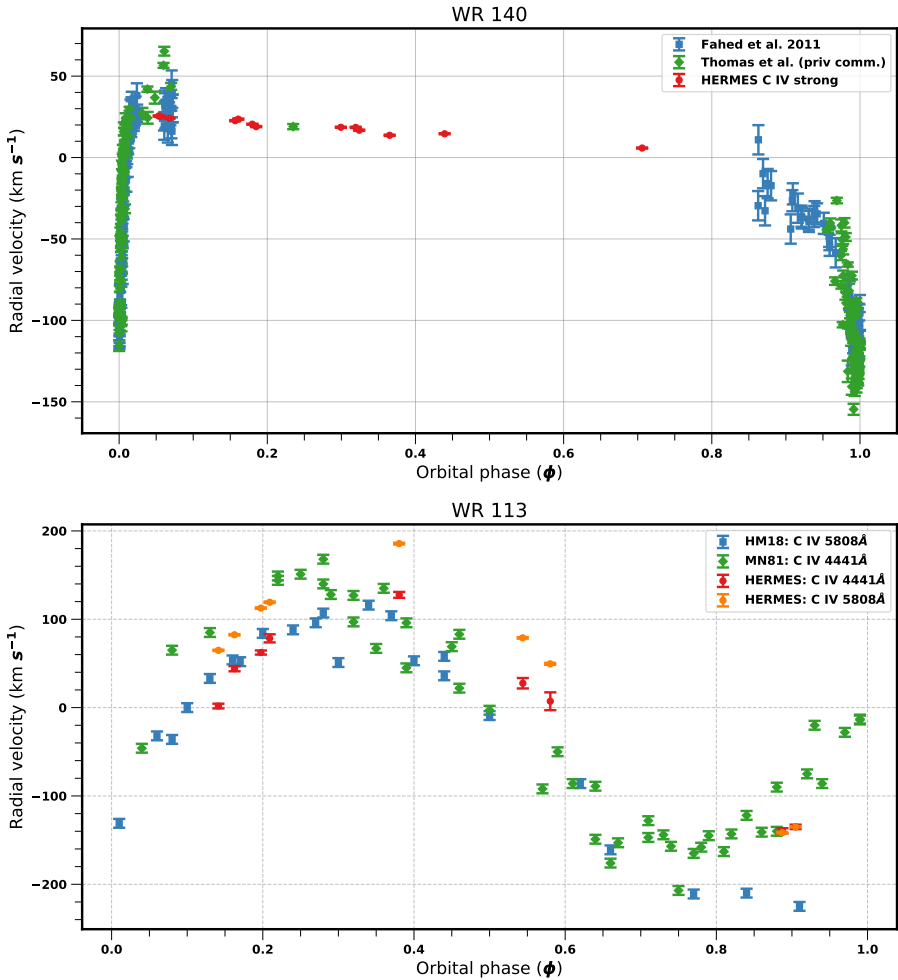


Figure 3.7: **Top:** Phased RV plot for WR 140. Archival RV measurements are shown in blue (Fahed et al. 2011) and green (Thomas et al. 2021). The RV measurements from HERMES (red) using C iv strong lines have been shifted by 19 km s^{-1} in order to convert relative RV measurements to absolute ones. **Bottom:** Same for WR 113. Archival RV measurements are shown in blue (Hill et al. 2018) and green (Massey 1981). The RV measurements from HERMES (red and yellow) have been shifted by -135 km s^{-1} in order to convert relative RV measurements to absolute values.

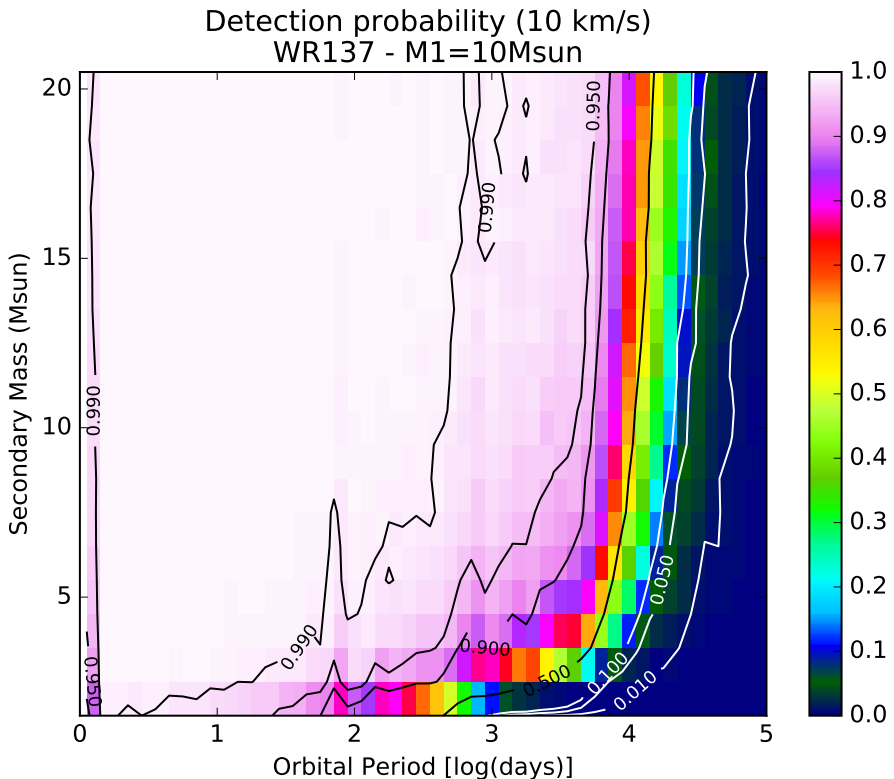


Figure 3.8: Detection probability for WR 137 as a function of the orbital period and secondary mass. A representative primary mass $10 M_{\odot}$ has been adopted for the WR star.

secondary masses ranging from 1 to 10^5 d and 1 to $20 M_{\odot}$ respectively, we adopt a flat eccentricity distribution between 0.0 and 0.9, a random orientation of the orbital planes in the three-dimensional space, random times of periastron passage, and RV measurements uncertainties of 1.6 km s^{-1} that are taken from the single stars in Table 3.2. Simulated RV time series of 2500 systems are computed at each $\log P - M_2$ grid cells, with steps of $\Delta \log P = 0.1$ and $\Delta M_2 = 1 M_{\odot}$, allowing us to compute the probability that the given orbital configuration would yield a RV signal passing our detection threshold, i.e. $\max(\Delta \text{RV}) > 10 \text{ km s}^{-1}$, given the observational sampling corresponding to each specific object. WC primary masses of $10 M_{\odot}$ are adopted throughout the simulations (average of the sample is $\sim 13 M_{\odot}$ [Massey 1981](#); [Lefèvre et al. 2005](#); [Sander et al. 2019](#); [Thomas et al. 2021](#)). An example of the resulting detection probability maps is given in Fig. 3.8. Plots for all other sources in our sample

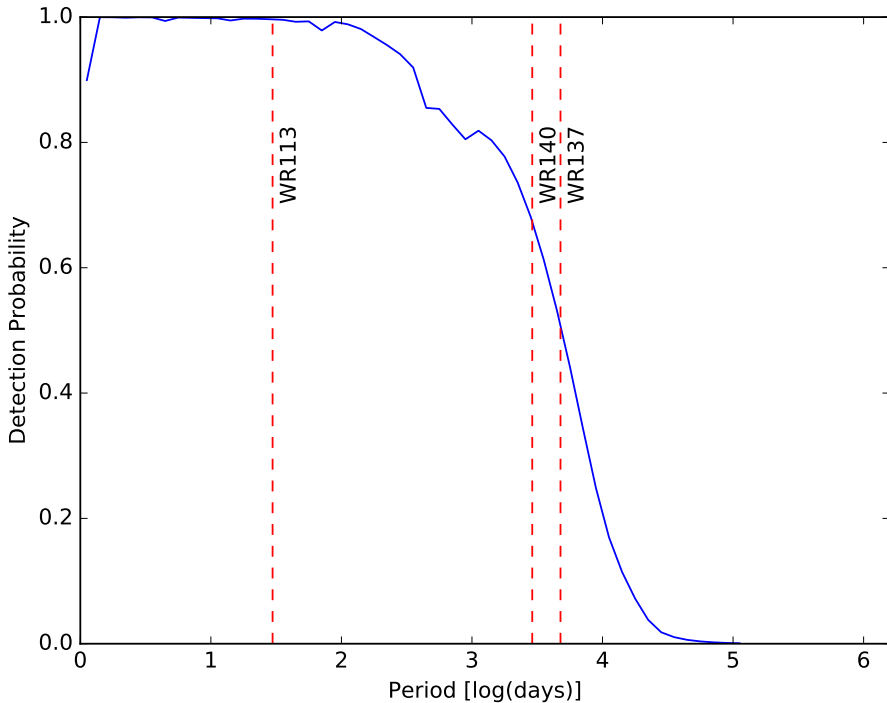


Figure 3.9: Average detection probability curve of our campaign as a function of the orbital period and assuming a flat mass-ratio distribution between 0.5 and 2.0. Known orbital periods of WC stars in our sample are indicated by vertical lines.

are included in Figs. A.1 and A.2. Detection probabilities well over 90% are reached up to periods of $10^{2.5}$ to $10^{3.5}$ d (i.e., 1 to 10 years) depending on the object, except at very low-mass companion masses. Figure 3.9 shows the combined detection probability as a function of the orbital period assuming a flat mass-ratio distribution between 0.5 and 2.0 (e.g., as in Langer et al. 2020) and indicates excellent detection rates close to 100% up to periods of 100 d, above 80% up to 1000 d, then dropping to 20% at 10 000 d.

Intrinsic multiplicity properties

The observed binary fraction is a minimum estimate on the number of true WC binaries in our sample. The number of undetected binary systems depends on our time sampling, our RV measurement accuracy, and the intrinsic distribution of orbital parameters. Given our limited sample size, it is beyond the scope of this paper (and probably

unrealistic) to perform a self-consistent derivation of the distributions of orbital parameters, and of the binary fraction (as in, e.g., [Sana et al. 2012, 2013](#)). Nevertheless, it is still possible to obtain useful information on the multiplicity properties of the parent population. In this context, we adopt two different and complementary approaches, both using MC simulations and the same underlying assumptions as in Sect. 3.4.3.

As a first step, we attempt to constrain the true binary fraction among our sample of WC stars. A simple approach would be to correct the number of detected binaries using a detection probability factor that depends on the orbital period of the detected binaries. This probability can be readily read from Fig. 3.9. Unfortunately, only three of the objects above our binary threshold have known orbital periods (see Table 3.2). Lacking further information, we conservatively adopt the detection probability corresponding to period of $10^{3.5}$ d (approximately 10 years) for the remaining objects (shorter periods can be excluded on the basis of the previous step, as they would have yield a RV-amplitude larger than 30 km s^{-1} in over 90% of the cases). Under these hypotheses, the obtained correction factor is found to be of the order of 3/2, suggesting an intrinsic binary fraction of about 0.9 for the objects in our sample in the considered parameter space (P up to 10^5 d and mass-ratios up to 3.0).

To test these intriguing results, we set up a last experiment where we test different period distributions and intrinsic binary fractions with the same assumptions on q , i , and e as in Sect. 3.4.3. We reject combinations of orbital configurations and binary fractions that cannot reproduce a simple observational fact: six objects are observed with values of ΔRV between 10 and 30 km s^{-1} within $1-\sigma$ (Fig. 3.6)¹. We constructed two experiments based on:

- a uniform log P distribution with variable minimum and maximum boundaries, and
- a normal log P distribution with variable central period and 1σ -dispersion.

For these experiments, we removed WR 113 from the sample as its significantly different orbital period would require more complicated functional forms than those adopted here. In that case, we also request that no system with an RV variation amplitude above 30 km s^{-1} be found.

In both cases, parent distributions with intrinsic binary fractions larger than 90% performed significantly better than those with lower binary fractions. This is in line with our above estimate based on the detection probability.

¹Similar results were obtained when trying to reproduce the number of stars with RV amplitude between 15 and 30 km s^{-1} .

Intrinsic binary fraction of the parent WC population

Overall, the results of these MC experiments suggest that WC stars in our sample have a large binary fraction and are dominated by long-period systems. The present sample was selected based on declination and magnitude limits and should not contain any specific selection bias. Therefore, it should remain representative of the entire WC population. Under these considerations, a test-of-hypothesis at the 10%-significance level allows us to reject parent binary fractions smaller than 0.72². This suggests that, with a 90% confidence limit, the true binary fraction of the carbon-sequence WR population in the Milky Way lays in the range 0.72 to 1.00. In contrast to the results in Sect. 3.4.3, the latter value does account for the sample size.

3.5 Evolutionary implications and conclusions

With a small, magnitude-limited sample of northern Galactic WC stars, we demonstrated that using cross-correlation with high-resolution spectra allows us to derive accurate RV measurements of WR stars, and to even quantify the wind-variability. With a sample of 12 stars spread evenly over different spectral-types, we find an observed binary fraction of 0.58. Using MC simulations, we attempt to gain information about the parent WC population and conclude that the fraction of Galactic WC stars that are part of a binary system is at least 0.72, significantly larger than the literature value of ~ 0.4 .

Our observations clearly show that there is a deficiency in the number of short-period WC binaries in the Galaxy. Furthermore, our MC simulations indicate that Galactic WC stars primarily exist in long-period binaries ($P > 100$ d). Increasing the sample and comparing these results to the populations of WN and main-sequence O-type binaries can help us put constraints on the viable evolutionary channels for WC stars and on the forward evolution of massive binaries. In Chapter 4, we analyse the 16 WNE stars in our sample compare the intrinsic multiplicity properties with those of the WC population.

²Specifically, binomial chances to draw 11 or more binaries in a sample of 12 (corresponding the retrieved intrinsic binary fraction in the sample of > 0.9) drops below 10% for parent binary fraction smaller than 0.72.

Chapter 4

Multiplicity properties of the Galactic WNE population

The work presented in this chapter is based on:

A spectroscopic multiplicity survey of Galactic Wolf-Rayet stars: II. The northern WNE sequence

K. Dsilva, T. Shenar, H. Sana and P. Marchant

Accepted for publication in ASTRONOMY AND ASTROPHYSICS,

Originally published as:

arXiv:2204.12518 [astro-ph]

Author contributions: K. Dsilva performed the data reduction and computed the radial velocities in this chapter with the guidance of H. Sana and T. Shenar. The Monte-Carlo simulations were run by H. Sana. The Bayesian framework was developed by P. Marchant and H. Sana. All the authors assisted with the evolutionary interpretations of the presented results and contributed significantly to the text, which was written by K. Dsilva.

Original abstract:

Most massive stars reside in multiple systems that will interact over the course of their lifetime. This has important consequences on their future evolution and their end-of-life products. Classical Wolf-Rayet (WR) stars represent the final end stages of stellar evolution at the upper-mass end. While their observed multiplicity fraction is reported to be ~ 0.4 in the Galaxy, their intrinsic multiplicity properties and the distributions of their orbital parameters remain insufficiently constrained to provide a reliable anchor to compare to evolutionary predictions.

As part of a homogeneous, magnitude-limited ($V \leq 12$) spectroscopic survey of northern Galactic WR stars, this paper aims to establish the observed and intrinsic multiplicity properties of the early-type nitrogen-rich WR population (WNE), including estimates of the multiplicity fraction and the shape of their orbital period distribution. Additionally, we compare these with the properties of the carbon-rich WR population (WC) stars obtained in the first paper of this series.

We obtained high-resolution spectroscopic time series of the complete magnitude-limited sample of 16 WNE stars observable with the 1.2 m Mercator telescope at La Palma, typically providing a time base of about two to eight years. We measured relative radial velocities (RVs) using cross-correlation and used RV variations to flag binary candidates. Using an updated Monte Carlo method with a Bayesian framework, we calculated the three-dimensional likelihood for the intrinsic binary fraction ($f_{\text{int}}^{\text{WNE}}$), the maximum period ($\log P_{\text{max}}$), and the power-law index for the period distribution (π) for the WNE population with P_{min} fixed at 1 d. We also used this updated method to re-derive multiplicity parameters for the Galactic WC population.

Adopting a peak-to-peak RV variability threshold of 50 km s^{-1} as a criterion, we classify 7 of the 16 targets as binaries. This results in an observed multiplicity fraction ($f_{\text{obs}}^{\text{WNE}}$) of 0.44 ± 0.12 . Assuming flat priors, we derive the best-fit multiplicity properties $f_{\text{int}}^{\text{WNE}} = 0.56_{-0.15}^{+0.20}$, $\log P_{\text{max}} = 4.60_{-0.77}^{+0.40}$, and $\pi = -0.30_{-0.53}^{+0.55}$ for the parent WNE population. We explored different mass-ratio distributions and note that they did not change our results significantly. For the Galactic WC population from Chapter 3, we re-derive $f_{\text{int}}^{\text{WC}} = 0.96_{-0.22}^{+0.04}$, $\log P_{\text{min}} = 0.75_{-0.60}^{+0.26}$, $\log P_{\text{max}} = 4.00_{-0.34}^{+0.42}$, and $\pi = 1.90_{-1.25}^{+1.26}$. The derived multiplicity parameters for the WNE population are quite similar to those derived for main-sequence O binaries but differ from those of the WC population. The significant shift in the WC period distribution towards longer periods is too large to be explained via expansion of the orbit due to stellar winds, and we discuss possible implications of our results. Analysis of the WNL population and further investigation of various

evolutionary scenarios is required to connect the different evolutionary phases of stars at the upper-mass end.

4.1 Introduction

According to the Conti scenario, single O stars will strip themselves of their envelope through their stellar winds and evolve spectroscopically into WN, WC and if massive enough, WO stars before ending their lives via core-collapse. However, the effect of multiplicity on this scenario and in general, massive star evolution, is not well constrained. While the intrinsic multiplicity properties of the main-sequence O population are well known, those for the WR population remain largely unconstrained. To remedy this, we undertook a spectroscopic monitoring campaign of 39 Galactic northern WR stars. In this chapter, we improve the methods explained in Chapter 1 and analyse the 16 WNE stars in our sample. We also revisit the 12 WC stars from Chapter 1, and discuss evolutionary consequences based on our results.

4.2 Sample and data reduction

4.2.1 Sample

We define the sub-class WNE as WN stars with spectral types equal to or earlier than WN5. In cases where objects are classified as ‘WN5-WN6’ in the GCWR, we consider them as WN5 for simplicity. As in Chapter 3, we used $V \leq 12$ or $v \leq 13$ and declination $\delta \geq -30^\circ$ as our selection criteria. This resulted in a magnitude-limited sample of 16 WNE stars whose known properties are summarised in Table 4.2. Their spectral-type distribution is shown in Fig. 4.1. We obtained at least six epochs of each of the target stars. When available, we used archival HERMES observations in the RV analysis, which reach a typical time base of two to eight years. The number of spectra and the sampling time of the observations are shown in Table 4.1. **The division of the sample into WNE and WNL (WN6 and later) parts fits in the Conti scenario, which predicts evolution from WNE to WNL spectral types. However, analysis based on the morphology of the spectra, i.e. strong- and broad-lined versus weak- and narrow-lined WN stars is an alternative partitioning of the WN sample which we do not explore.**

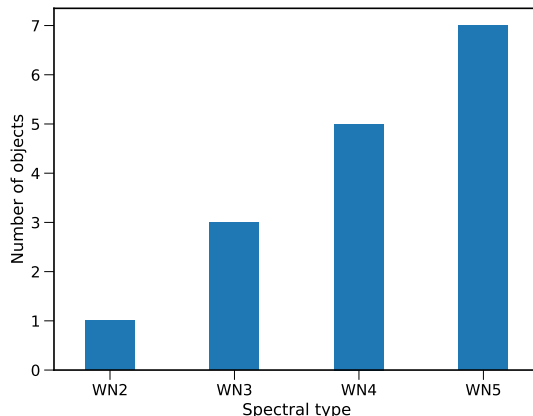


Figure 4.1: Distribution of spectral types within the present WNE sample.

4.2.2 Data reduction and normalisation

The data reduction procedures for our spectra are comprehensively described in Chapters 1 and 3. After this step, what remains is the effect of interstellar reddening superimposed on the continuum from the wind. The normalisation of the spectra was performed in a similar manner to Chapter 3.

We used a model of a normalised spectrum of a WNE star from the Potsdam Wolf-Rayet code (PoWR; [Gräfener et al. 2002](#); [Hamann & Gräfener 2003](#); [Hamann & Gräfener 2004](#); [Todt et al. 2015](#)) to identify pseudo-continuum regions, in the blue around 5300 Å and in the red around 8100 Å. We then anchored the stellar continuum model for the same WNE star to the red point and applied a reddening to fit the slope. We explored various reddening laws and R_V values and realised that they did not significantly impact the homogeneity of the normalisation process. Therefore, as in Chapter 1, we used the reddening law from [Fitzpatrick \(2004b\)](#) and R_V of 3.1, the average for the galaxy.

4.3 Measuring radial velocities

Deriving RVs of WR stars is not a trivial process given their strong, broad emission lines that form in their outflowing winds. Of the methods that are used extensively in the community, we used cross-correlation as our tool of choice, with a statistical framework that allows us to derive meaningful uncertainties on our RV measurements ([Zucker 2003](#), see Chapter 3 for more details). As mentioned in Chapter 3, we focus on the RVs of the WR star even in SB2 systems to maintain homogeneity in the analysis

Table 4.1: List of WNE stars in our RV monitoring campaign, providing the number of spectra, time coverage, and average signal-to-noise (S/N) per resolution element at 4400 Å ($\Delta\lambda \approx 0.05$ Å).

WR#	Spectra	Time coverage (d)	Average S/N
1	27	1264	40
2	18	1085	45
3	8	120	70
6	28	1025	120
7	7	642	45
10	6	678	60
110	11	1142	50
127	11	2646	80
128	10	1120	80
133	21	2890	200
138	40	2898	100
139	34	2954	150
141	14	2140	50
151	6	924	20
152	7	921	40
157	12	2168	70

and to focus on binary detection instead of orbital analysis. We briefly describe the formulation and assumptions of the CCF.

4.3.1 Cross-correlation and mask selection

The CCF is the convolution of a chosen template to the data to measure the velocity shift. It is represented by a log-likelihood function, where the maximum is the RV of the spectrum. The uncertainty on the RV measurement can then be derived from maximum log-likelihood theory. An implicit assumption of the method is that the template accurately reproduces the data. Because WR models often do not accurately represent the shape of both strong and weak lines simultaneously, we chose the highest signal-to-noise (S/N) epoch as the template. The measured RVs were then used to construct a weighted co-added spectrum of a higher S/N. This process was iterated until the derived RVs no longer changed significantly within the measurement errors, at which point the final template and measurements were converged. The S/N of the template contributes significantly to the measured uncertainty, and this was minimised by creating a high S/N co-added spectrum. A caveat is that the RVs derived in this

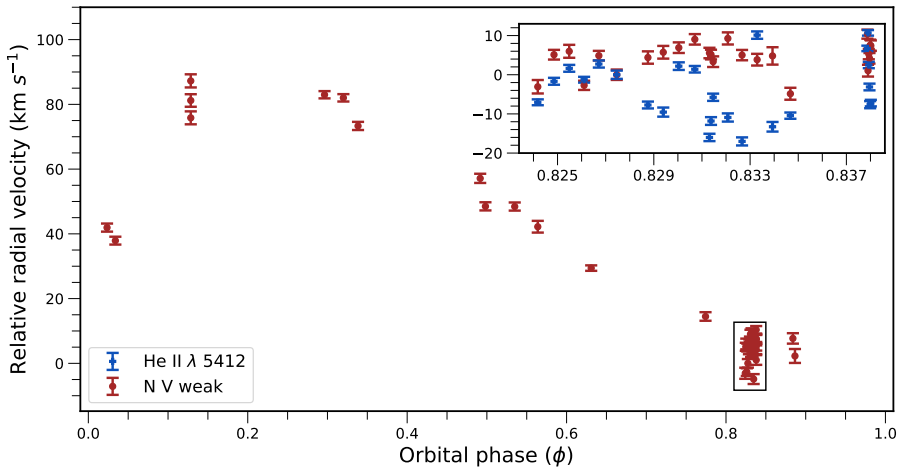


Figure 4.2: Phased RV plot for WR 138 with HERMES data. The inset shows the high-cadence measurements (black box) with the N v weak lines and the He ii $\lambda 5412$ line. The ephemeris used for the periastron passage was JD 2445284 ([Annuk 1990](#)), with the period of 1521.2 ± 35 d from [Palate et al. \(2013\)](#).

fashion are relative RVs. While this is sufficient for binary detection, an absolute shift must be applied when comparing to RVs from the literature.

When compared with the WC stars analysed in Chapter 3, the WNE stars in our sample exhibit stronger line-profile variability in their spectra **on average, although WR 6 is an example of an outlier**. Therefore, the assumption that the template accurately represents the data often breaks down for variable stars. This directly results in larger uncertainties on the derived RVs. In order to ensure that the templates can represent the data as accurately as possible, for each star we selected encompassing spectral lines that are least affected by line-profile variability. Depending on how variable the stars are, we used lines of N iv, N v, He ii, and when possible, Balmer lines. In cases of strong line-profile variability, we tend to only use N v lines and occasionally N iv lines because they are thought to form in the hotter, inner regions of the stellar wind. We used a combination of all the different lines of various strengths and ions used to measure RVs and call this mask ‘full spec’ (e.g. a combination of N v, N iv, and He ii lines).

Relative RV measurements with the high cadence data for WR138

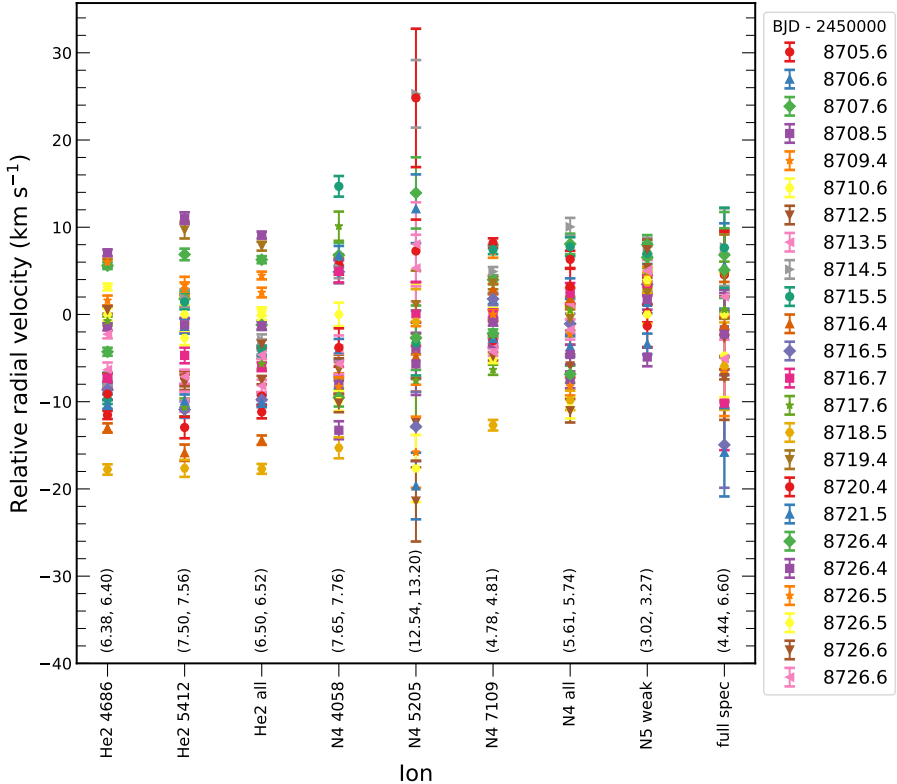


Figure 4.3: High-cadence relative RV measurements for WR 138 using different masks. At the bottom of the plot are the values of (σ_w, σ_{RV}) (km s^{-1}) for each mask. As mentioned in the text, ‘full spec’ is a combination of all the masks to its left and not the entire spectrum. The N IV line at 5205 \AA is very weak, which explains its high scatter.

4.3.2 Studying the long-period binary system WR 138 to quantify wind variability

In Chapter 3, we analysed high-cadence data of the long-period binary system WR 137 in order to understand the effect of wind variability and other systematic effects on the RV measurements. As a nitrogen-rich analogue, we studied the long-period binary WR 138 (WN5o + O9V) with a period of 4.16 yr and a low eccentricity of 0.3 (Palate et al. 2013; Annuk 1990; Richardson et al. 2016). Palate et al. (2013) also studied the system in X-rays, concluding that its emission is normal for a colliding-wind WR + OB binary system, although the sampling of their data did not allow them to check for the

existence of phase-locked variability of the X-ray emission.

With this in mind, we collected high-cadence HERMES data in August of 2019 (with the periastron passage in June 2020). In total, we obtained 18 spectra over 16 consecutive nights and 6 spectra over one night a few days later (Table B.11). The phased RV plot of WR 138 is shown in Fig. 4.2 with an emphasis on the high-cadence data over different masks. Because the high-cadence data were collected at the orbital phase of 0.8, the effect of wind-wind collision (e.g. Lührs & Moffat 2002) on the measured RVs could be significant. Using the systemic and stellar parameters (Annuk 1990; Richardson et al. 2016), we computed the cooling parameter χ (Stevens et al. 1992) and found the shocked region to be adiabatic. As the cooling timescale is longer than the escape timescale, the contribution to recombination lines in the optical is minimal. Therefore, the contribution of wind-wind collision to the RV measurements should not change significantly over the timescale of the high-cadence observations. Even if wind-wind collision were to contribute significantly to the RV measurements, the derived scatter in the high-cadence study would be an upper limit on the intrinsic wind variability of the WR star.

For the high-cadence data, the contributions to the uncertainties in the measured RVs are statistical (i.e. from the method, σ_p) and physical (i.e. from the wind physics, σ_w). The weighted standard deviation of the high-cadence measurements are indicative of the true error, which we denote by σ_{RV} . Assuming σ_p and σ_w are uncorrelated, they can simply be added quadratically as described in Eq. 3.13.

For each mask, σ_p is calculated from the co-variance matrix of the CCF (Eq. 3.9). Using Eq. 3.13 along with the calculated values of σ_p and σ_{RV} , we obtain an estimate for σ_w . The high-cadence data therefore allow us to isolate and quantify the effect of wind variability on the RV measurements. The lines that are least affected by wind variability are N v weak lines (Appendix. B.1, $\sigma_w \sim 5 \text{ km s}^{-1}$). Lines of He ii and N iv lines are found to be more variable ($\sigma_w \sim 10 \text{ km s}^{-1}$). As their formation regions can be spatially different, these measurements can be helpful probes of turbulence and other physical processes. The difference in dispersion for lines of N iv arise from the different line strengths and since the S/N in the blue is much lower than in the red. The mask ‘full spec’ is a combination of the N iv, He ii, and N v lines. The mask ‘N4 7109’ covers the triplet N iv $\lambda\lambda 7103, 7109, 7123$. Ultimately, we chose to measure RVs for WR 138 using weak N v lines, namely a combination of N v $\lambda\lambda 4604, 4620$, and N v $\lambda 4945$.

Although we observed that weak N v lines showed the least intrinsic variability for WR 138, this cannot necessarily be generalised for all WNE stars. However, for all the objects in our sample, we realised that the N v lines indeed had the least RV dispersion, and we therefore used them to measure RVs. For stars with strong line-profile variability (WR 2, WR 6, WR 7, and WR 110), we used the combination of all masks (‘full spec’) to measure RVs (Appendix. B.1). The full journal of RV measurements for each object with their respective masks is given in Appendix. A.2.

Table 4.2: Overview of the known multiplicity properties of our sample of WNE stars together with the results of our RV measurements. ΔRV and σ_{RV} are calculated in this work and are used to identify tentative spectroscopic binaries. The spectral types are taken from the GCWR unless indicated otherwise. The binary status of this work is reported based on the spectroscopic observations.

WR#	Spectral Type (GCWR)	Binary Status (GCWR)	Period (d)	e	ΔRV (km s $^{-1}$)	σ_{RV} (km s $^{-1}$)	$\Delta RV > C$
1	WN4	SB1?	-	-	37.5	8.6	no
2	WN2	VB	VB ⁽ⁱ⁾	-	36.9	8.3	no
3	WN3ha	SB2	-	- ^(a)	5.0	1.8	no
6	WN4b	SB1	SB1	3.8 ^(b)	0.1 ^(b)	170.0	40.3
7	WN4b	-	-	-	33.3	10.8	no
10	WN5h	VB	VB ⁽ⁱ⁾	-	9.9	3.6	no
110	WN5b	-	-	-	31.8	11.3	no
127	WN3b + O9.5V	SB2	SB2	$9.5550 \pm 0.0002^{(c)}$	$0.04 \pm 0.02^{(c)}$	332.0	108.9
128	WN4(h)	SB2?, VB	VB ⁽ⁱ⁾	-	9.7	2.8	no
133	WN5o + O9I	SB2, VB	SB2, VB ⁽ⁱ⁾	$112.780 \pm 0.036^{(d)}$	$0.3558 \pm 0.0050^{(d)}$	111.6	25.8
138	WN5o + O9V ^(e)	SB2, VB	SB2, VB ⁽ⁱ⁾	$1521.2 \pm 35^{(f)}$	$0.3^{(g)}$	92.1	29.4
139	WN5o + O6III-V	SB2	SB2	$4.212435^{(h)}$	$0.036 \pm 0.009^{(h)}$	618.3	168.9
141	WN5o + O5V-III	SB2	SB2	$21.6895 \pm 0.0003^{(i)}$	$0.018 \pm 0.035^{(i)}$	209.8	66.5
151	WN4o + O5V	SB2	SB2	$2.12691 d^{(j)}$	0 (fixed) ^(k)	650.0	220.7
152	WN3(h)	-	-	-	8.3	2.6	no
157	WN5o + (B0.7II + B1III) ^(k)	VB	SB3, VB ⁽ⁱ⁾	-	11.8	3.6	no

^(a) Moffat et al. (1986) reported a period of 46.8 d, but it is not supported by our analysis (App. B.1),

^(b) Koenigsberger & Schmutz (2020),
^(c) de La Chevriote et al. (2011),

^(d) Richardson et al. (2021),
^(e) Richardson et al. (2016),

^(f) Palate et al. (2013),
^(g) Annuk (1990), ^(h) Marchenko et al. ((1994)[fixed P; 4.212435 d]),

⁽ⁱ⁾ Marchenko et al. (1998a), ^(j) Hutton et al. (2009), ^(k) Maiz Apellániz et al. (2021), ^(l) VB status carried over from the GCWR.

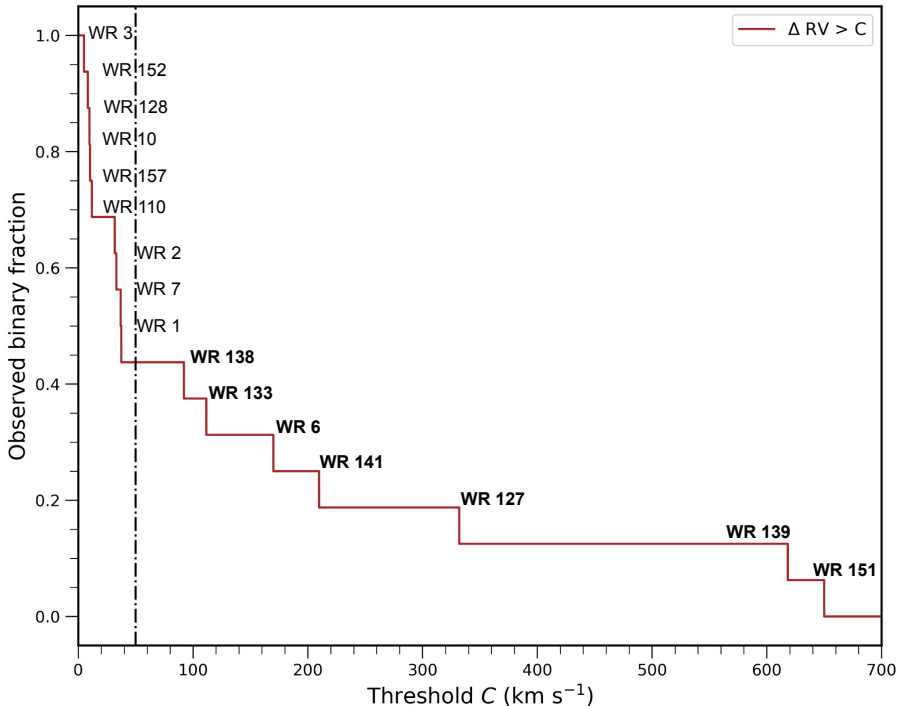


Figure 4.4: Non-parametric threshold plot showing the inverse cumulative distribution of peak-to-peak RV variability in our sample, which is equivalent to the observed binary fraction ($f_{\text{obs}}^{\text{WNE}}$) as a function of the adopted peak-to-peak RV variability threshold C . Names in bold are known binaries with established spectroscopic periods for the WR components.

4.4 Observed binary fraction

For each star in our sample, we measured the RVs and obtained their peak-to-peak variability amplitude (ΔRV). We then selected a threshold to determine the boundary beyond which the RV amplitude would be dominated by orbital motion in a binary system. We plot the binary fraction as a function of this threshold in a non-parametric threshold plot (Fig. 4.4). By moving the threshold from higher to lower RV values (right to left in Fig. 4.4), we classify more stars as RV variable, hence putative spectroscopic binaries. A summary of the characteristics of the WNE stars in our sample can be found in Table 4.2. As we cannot verify the status of objects classified as visual binaries (VB) in the GWCR, we simply carry over their status in our classification.

The next step was to choose an adequate value for the threshold C such that stars with $\Delta RV \geq C$ were classified as binaries. It is important that the chosen threshold avoids false positives, in particular, those that are erroneously classified as binaries due to strong intrinsic variability. The high-cadence study of WR 138 is a useful guideline to ensure this. The peak-to-peak RV amplitude measured due to wind variability was observed to be 15 km s^{-1} for the N v lines (Fig. 4.3). We therefore chose a conservative threshold larger than three times this value, that is, 50 km s^{-1} . This results in 7 of the 16 observed binaries in the sample, $f_{\text{obs}}^{\text{WNE}} = 0.44$ with a binomial error of ± 0.12 . Interestingly, all the known spectroscopic binaries in our sample with an established orbital solution are properly identified with the adopted threshold. For objects with $\Delta RV < 50 \text{ km s}^{-1}$ and a large enough RV time series (WR 1 and WR 2), we investigated possible periodicities using a Lomb-Scargle periodogram (Lomb 1976; Scargle 1982), but found no coherent periodicity.

4.5 Intrinsic multiplicity properties

4.5.1 Detection probability

In order to determine the intrinsic multiplicity fraction of Galactic WNE stars, $f_{\text{int}}^{\text{WNE}}$, it is important to understand the observational biases of the RV campaign. The number of detected binaries is merely a minimum estimate of the true number of WNE binaries in our sample. Physical and orbital properties of the systems, geometrical effects, time coverage, and sampling of the RV study all affect the binary detection probability. As in Chapter 3, we modelled the detection probability, estimated the number of undetected binaries, and constrained some of the properties of the parent WNE population.

Using MC simulations, we determined the sensitivity of our survey with the method explained in Patrick et al. (2019). We constructed a grid with different orbital periods (P) and secondary masses (M_2) between 1 and 10^5 d and 1 and $40 M_\odot$, respectively. The grid was evenly spaced with steps of $\Delta \log(P/\text{d}) = 0.1$ and $\Delta M_2 = 1 M_\odot$. For each grid point of $\log P$ and M_2 , we simulated RV time series for 40 000 binary systems assuming a primary mass of $20 M_\odot$, which is **the average value for the stars in our sample with values reported through model atmospheric analysis** (Hamann et al. 2019). The eccentricities were drawn from a flat distribution between 0.0 and 0.9. We assumed random orientations of the orbital plane in three-dimensional space and random times of periastron passage.

The RV time series at each grid point were simulated according to the observational sampling (number of epochs, time base) for each object. This allowed us to compute the probability that a given orbital configuration in $\log P$ and M_2 would give us an RV signal that would pass our detection threshold (i.e. $\Delta RV \geq C = 50 \text{ km s}^{-1}$). An

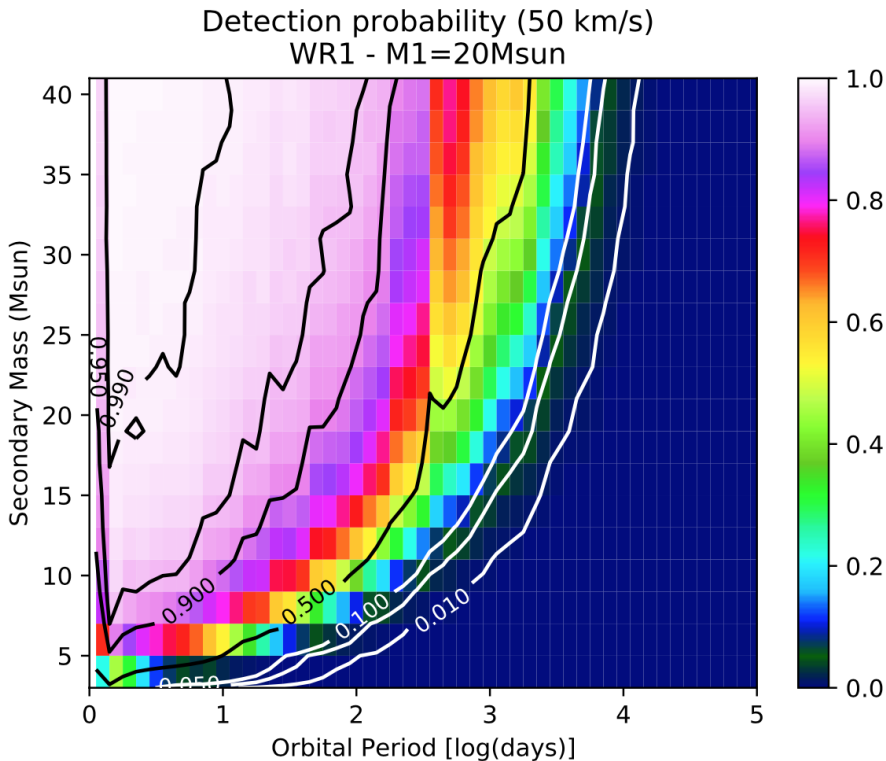


Figure 4.5: Binary detection probability for WR 1. It is computed assuming $M_1 = 20 \text{ M}_\odot$ and other conditions described in Sect. 4.5.1. We have a detection probability of $\geq 90\%$ up to periods of 10^2 d at $M_2 \geq 20 \text{ M}_\odot$ and $> \sim 20\%$ at a period of 10^3 d .

example of such a probability detection plot is shown in Fig. 4.5. After we determined the probability detection plots for each object, we computed the average over the grid of $\log P$ and M_2 . Assuming a flat mass-ratio between 0.1 and 2.0 with a primary mass of $M_1 = 20 \text{ M}_\odot$, we averaged over the secondary mass to calculate the average detection probability as a function of orbital period (Fig. 4.6). In Chapter 3, we adopted $C = 10 \text{ km s}^{-1}$, so that the efficiency of detecting WC binaries dropped below $\sim 80\%$ at orbital periods of 1000 d (Fig. 3.9). Here, due to a larger adopted threshold C for our WNE sample, this efficiency drops below 80% already at periods of $\sim 100 \text{ d}$ (Fig. 4.5).

Figure 4.6 shows the global detection probability of our RV campaign as a function of the orbital period. As a first approach, the observed binaries in our sample can be corrected with their respective detection probability, and thus the number of true binaries in our sample can be estimated. We ignored WR 3 in this exercise as we did

not classify it as a RV variable system (Fig. 4.4), and we ignored WR 6 since we are unable to confirm the orbital period with our data (Appendix B.1). After defining a quantity $p(P)$ to be the detection probability for each binary detected with a given orbital period P , we expect our sample to contain $1/p(P)$ binary systems. The largest correction factor comes from WR 138, which has a detection probability of ~ 0.33 . We therefore expect three similarly long period binaries ($1/0.33$) to be present in our sample on average. Given the six detected binaries in our sample, we expect about nine binaries in the sample, corresponding to an $f_{\text{int}}^{\text{WNE}}$ of 0.56. This straightforward counting correction is only possible because the orbital periods of the binary systems are known, but it can be strongly affected by small sample statistics.

4.5.2 Adopting a Bayesian approach

Because $p(P)$ is a strong function of P , the bias-corrected binary fraction depends on the underlying period distribution. Here, we adopt a more formal approach to determine both within a Bayesian framework. The model parameters of a population with binaries include those that describe the period distribution, binary fraction, inclination, eccentricity, mass ratio, orientation of the orbital plane, time of periastron passage, and so on. Ideally, we would like to calculate the likelihood of observing the RV time series for each object given these model parameters. However, this is computationally too intensive, and thus we adopted a different strategy. We divided the 16 WNE stars into four ΔRV bins: $\Delta\text{RV} \leq 50 \text{ km s}^{-1}$ (nine objects), $50 < \Delta\text{RV} \leq 250 \text{ km s}^{-1}$ (four objects), $250 < \Delta\text{RV} \leq 650 \text{ km s}^{-1}$ (three objects) and $\Delta\text{RV} > 650 \text{ km s}^{-1}$ (no objects).

The shape of the period distribution is parametrised by its power-law index π as follows:

$$p(\log P) \sim (\log P)^\pi. \quad (4.1)$$

The period distribution further has lower and upper bounds, called $\log P_{\min}$ and $\log P_{\max}$. Along with $f_{\text{int}}^{\text{WNE}}$, we explored π , $\log P_{\min}$, and $\log P_{\max}$ as model parameters. Because very short period WNE binaries are present in our sample, we fixed $\log P_{\min} = 0.15 \text{ [d]}$. We explored $\log P_{\max}$ in the range of 3.0 to 5.0 in steps of 0.1. We explored values of π from -1.0 to 1.0 in steps of 0.1, and $f_{\text{int}}^{\text{WNE}}$ from 0.3 to 1.0 in steps of 0.02. For each bin in this three-dimensional parameter space, we simulated 40 000 sets of 16 WNE stars, that is, over 6×10^8 populations. The assumptions for the eccentricity, inclination, and so on are the same as the MC simulations above (Sect. 4.5.1). Based on our prior knowledge of the known orbital periods (Table 4.2), when possible, we enforced that our simulations had at least seven binaries in period bins: $P > 1 \text{ d}$ (seven systems), $P > 10 \text{ d}$ (four systems), $P > 100 \text{ d}$ (two systems), and $P > 1000 \text{ d}$ (one system).

We then proceeded to compute the three-dimensional likelihood of observing the different numbers of objects in ΔRV bins as a function of $\log P_{\max}$, π and $f_{\text{int}}^{\text{WNE}}$ (Fig. 4.7). Assuming flat priors for each of the three parameters, we computed the

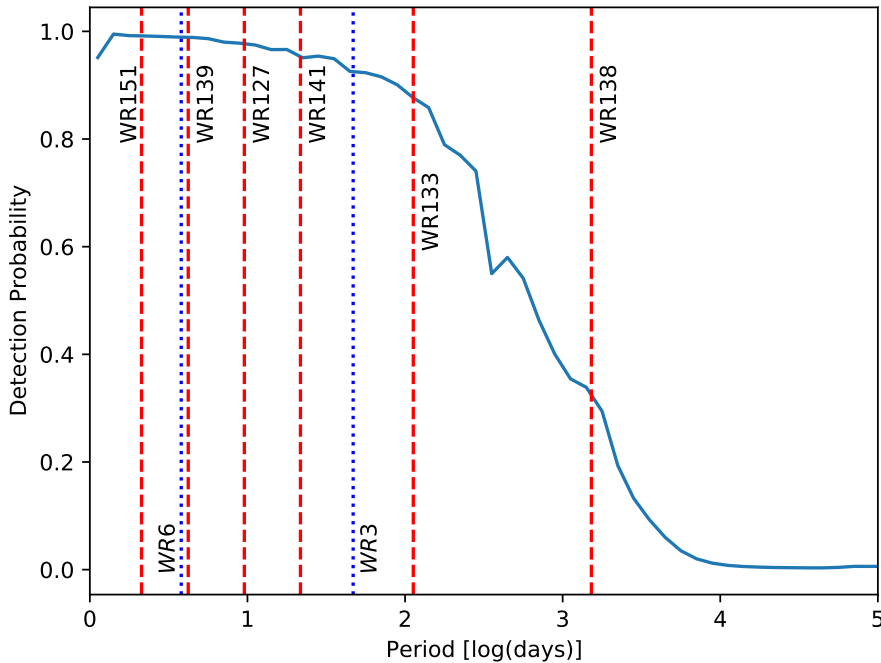


Figure 4.6: Binary detection probability of our campaign, assuming a flat mass-ratio distribution between 0.1 and 2.0 with a primary mass of $20 M_{\odot}$ and a flat eccentricity distribution between 0.0 and 0.9. The known binaries are marked with dashed red lines. WR 3 and WR 6 are marked with dashed blue lines because their reported periods cannot be verified with the available data.

marginalised posterior likelihood for the individual parameters. For each posterior, we report the mode and the 68% highest-density interval (HDI68). Our computations yield HDI68s of $f_{\text{int}}^{\text{WNE}} = 0.56^{+0.20}_{-0.15}$, $\log P_{\text{max}} = 4.60^{+0.40}_{-0.77}$, and $\pi = -0.30^{+0.55}_{-0.53}$. The upper bound of $\log P_{\text{max}}$ is poorly constrained and is set by the maximum of the grid (5.00). However, an increase in $\log P_{\text{max}}$ would simply result in an increase in $f_{\text{int}}^{\text{WNE}}$ in order to maintain the fraction of binaries at shorter periods, which is required to reproduce our observations (Fig. 4.4). A negative value for π indicates a slight preference for an overabundance of shorter-period systems. The obtained values are consistent with the values estimated for main-sequence O stars ($f_{\text{bin}} = 0.69 \pm 0.09$, $\pi = -0.55 \pm 0.22$: Sana et al. 2012). Similarly, our best-fit results suggest a long-period tail in the period distribution that extends to at least 20 yr and probably more.

One of the caveats of our simulations is the assumption on the mass ratio distribution. We have assumed a flat distribution between 0.1 and 2. However, this need not be the

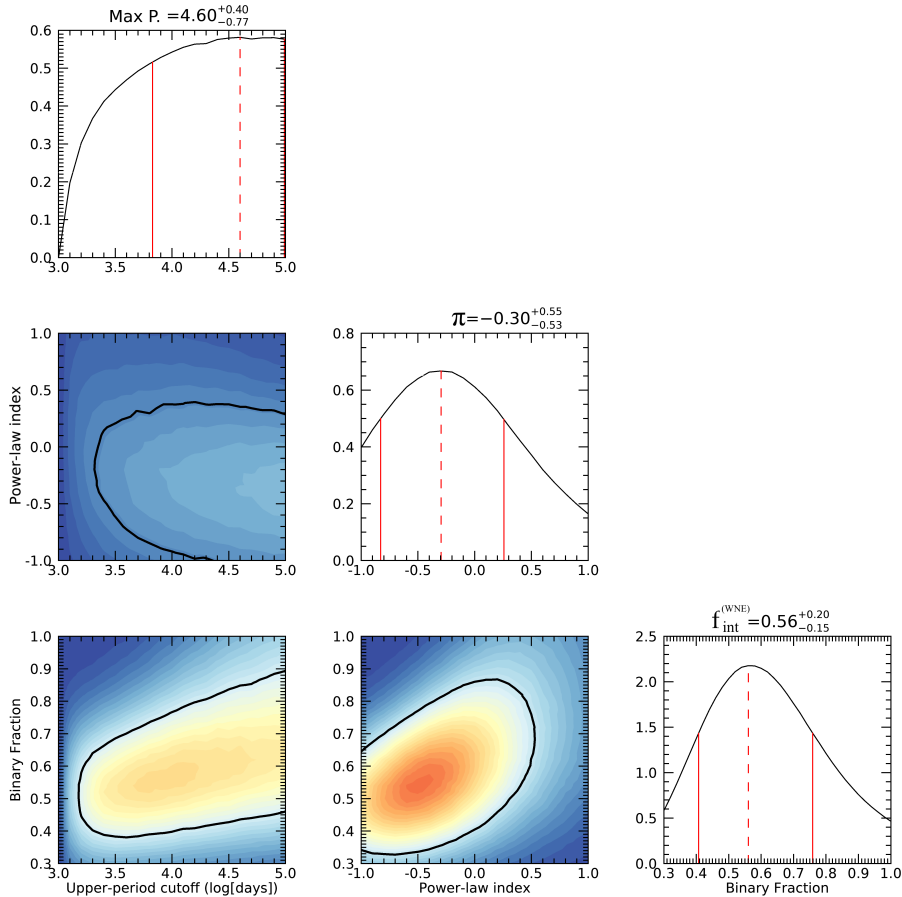


Figure 4.7: Three-dimensional likelihood over $\log P_{\text{max}}$, $f_{\text{int}}^{\text{WNE}}$, and π . Assuming flat priors, the one-dimensional posteriors are also shown. For each posterior, the solid red lines show HDI₆₈, and the dashed red line shows the mode.

case in nature, as the outcome of binary interaction scenarios is an important variable. Table 4.2 shows that known companions around WNE stars are main-sequence O stars (i.e. more massive companions). However, this result may suffer from a bias because binaries with low-mass companions will be much harder to detect. This is because the WR companion will not show much RV variation, and the brightness ratio will make it hard to detect any spectral features of the companion. We therefore decided to explore various power-law indices for the mass ratio distribution (κ). With the same setup as above, we assumed $\kappa = +1.0$ and -1.0 for the mass-ratio distribution and computed the

same three-dimensional likelihood (Figs. B.2 and B.3, respectively). The conclusions from Fig. 4.7 did not change significantly, with $\kappa = -1.0$ yielding more short-period binaries ($\pi = -0.6$) alongside a larger $f_{\text{int}}^{\text{WNE}}$ of 0.66, and $\kappa = +1.0$ yielding more massive companions with a slightly lower $f_{\text{int}}^{\text{WNE}}$ of 0.54. In all cases, the constraint on the minimum extent of the period distribution remained similar with $\log P_{\max} > 3.8$.

4.5.3 Revisiting the WC sample

We reanalysed our results from Chapter 3 using the improved statistical framework presented in Sect. 4.5.2. We calculated the four-dimensional likelihood and posteriors for $\log P_{\min}$, $\log P_{\max}$, $f_{\text{int}}^{\text{WNE}}$ and π in order to provide a fair comparison. Unlike in the WNE sample, we did not fix P_{\min} because we do not have many observational constraints. We explored $\log P_{\min}$ from 0.15 up to values of 2.95 and $\log P_{\max}$ from 3.0 to 5.0, both in steps of 0.1. In order to fit the absence of short P systems, a low number of intermediate P and a large number of long P binaries, we explored values of π from -1.0 to $+4.0$ in steps of 0.1. We also explored values of $f_{\text{int}}^{\text{WC}}$ from 0.30 to 1.00 in steps of 0.02. As in Sects. 4.5.1 and 4.5.2, we assumed a flat distribution for the eccentricity between 0.0 and 0.9, random orientations of the orbital plane in three-dimensional space, and random times of periastron passage.

The WC sample was separated into four ΔRV bins: $10 \leq \Delta\text{RV} \leq 30 \text{ km s}^{-1}$ (six objects), $30 \leq \Delta\text{RV} \leq 250 \text{ km s}^{-1}$ (no objects), $250 < \Delta\text{RV} \leq 300 \text{ km s}^{-1}$ (one object) and $\Delta\text{RV} \geq 300 \text{ km s}^{-1}$ (no objects). We then determined the likelihood of observing the same binned distribution for given values of the four model parameters. We also enforced that our simulations have binaries in the following period bins: $P > 20 \text{ d}$ (three systems), $P > 2000 \text{ d}$ (two systems). Assuming a primary mass of $10 M_{\odot}$, we simulated 10 000 populations of 12 WC stars for each bin in this four-dimensional parameter space, hence $\sim 1.1 \times 10^{10}$ populations. Fig. 4.8 shows the four-dimensional likelihood plots along with the one-dimensional posteriors assuming flat priors. The white areas of the plot have a computed likelihood of zero, meaning that none of the 10 000 populations computed for this set of parameters matched the observations. The HDI68 values are $f_{\text{int}}^{\text{WC}} = 0.96^{+0.04}_{-0.22}$, $\log P_{\min} = 0.75^{+0.26}_{-0.60}$, $\log P_{\max} = 4.00^{+0.42}_{-0.34}$, and $\pi = 1.90^{+1.26}_{-1.25}$. The values of $f_{\text{int}}^{\text{WC}}$ and π are in agreement with the results of Chapter 3, where we found the majority of WC binaries with $P > 100 \text{ d}$ and $f_{\text{int}}^{\text{WC}} > 0.72$.

Based on the above analyses, the visualisation of the intrinsic period distributions of the WC and WNE populations is presented in Fig. 4.9. The period distribution for the WNE population using the best-fit values of $\log P_{\max}$ and π , with P_{\min} fixed at 1 d, is shown in red. The solid blue line shows the period distribution for the WC population using the best-fit values of $\log P_{\min}$, $\log P_{\max}$, and π . In an attempt to express the uncertainties of these parameters on the period distribution, we sampled their posteriors 10 000 times and over-plot the resulting constructed period distributions. The dark and light

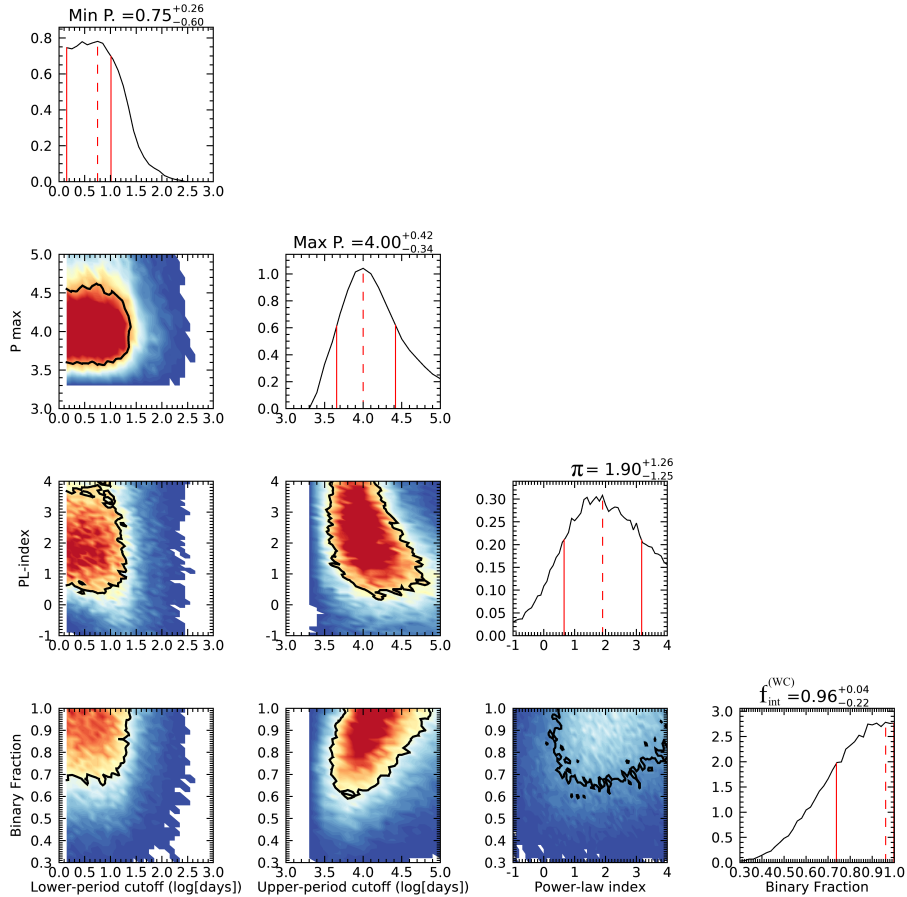


Figure 4.8: Four-dimensional likelihood over $\log P_{\min}$, $\log P_{\max}$, $f_{\text{int}}^{(\text{WC})}$, and π for the WC sample. Assuming flat priors, the one-dimensional posteriors are also shown. For each posterior, the solid red lines show the HDI68, and the dashed red line shows the mode.

shaded areas show 68% and 95% of the highest density covered by the distributions, respectively. For the sake of comparison, the distribution for main-sequence O stars from Sana et al. (2012) is also shown (dashed black line).

The derived multiplicity properties might be affected by spectral variability in WR stars on the RV measurements and by the relatively small sample of stars we used. While wind variability in WR stars has a significant effect on the measured RVs, we thoroughly quantified this using our high-cadence studies (Sect. 4.3.2 and Chapter

3) and statistically accounted for it, using a variability threshold that is high enough to avoid false positives. Similarly, the Bayesian framework presented here accounts for the small sample size. Unless our sample is significantly biased and does not (in a statistical sense) reflect the properties of the parent WNE and WC populations, our conclusions that the WNE and WC stars have different period distributions should hold. We further elaborate on these two aspects in Sects. 4.6.1 and 4.6.2.

4.6 Discussion

4.6.1 Comparison of the binary properties with the literature

In order to assess whether our results might be biased by the small sample, we explored the literature for statistics on the WNE binary fraction. The GCWR has a total of 387 WN stars, of which 97 are classified as WNE¹. Most of the WR stars in the past decades have been detected through infrared surveys as they are embedded in dust and/or suffer from substantial reddening or extinction, and their multiplicity properties are poorly studied. In order to discuss $f_{\text{obs}}^{\text{WNE}}$ in the context of a comparable sample that has been well studied for multiplicity, we considered the stars in VDH01. The catalogue reports a total of 127 WN stars, of which 49 are of the WNE subtype. Of this subset of 49 stars, 13 are WNE binaries with derived spectroscopic orbital solutions. The observed spectroscopic multiplicity fraction for WNE stars in VDH01 is then 0.27.

Table 4.2 shows that most of the WNE binary systems in our sample with known periods have periods of a few days to a hundred days. WR 138 is the only long-period binary system with a period of about four years. In VDH01, all of the other WNE binaries with derived spectroscopic orbital solutions have orbital periods shorter than 15 d (Fig. 1.7). Therefore, the observed period distribution of the WNEs in our sample seems to be confirmed with the threefold larger literature-based sample. In contrast to the WC stars studied in Chapter 3 and a similar literature search VDH01, there seems to be a systematic skew in the observed period distribution, with a higher frequency of short-period WNE binaries than long-period ones, even in logarithmic space. There is thus no indication that our sample is biased, nor that the results of Sect. 4.5 are contradicted by known WR properties from the existing literature at large.

4.6.2 Observational biases due to the magnitude limit

Considering a population of Galactic WR stars within a certain volume, it is reasonable to assume that the WR stars in binaries will be brighter than the single WR stars

¹As indicated previously, we do not consider WN6 stars to be WNE stars.

([Vanbeveren & Conti 1980](#)). This implies a potential bias due to our selection criterion, which will be larger or smaller depending on the contrast in brightness between the binaries and the single stars. Because most known WR binaries comprise OB-type companions, we made the simplifying assumption that WR binaries are twice as bright as single WR stars on average (e.g. [Shenar et al. 2019](#)). This implies that to avoid this bias, we should include single WR stars in the V -band magnitude range 12.0 to 12.7 mag.

In order to investigate this, we explored the GCWR for WNE stars within this magnitude range. For stars with missing V -band magnitudes, we searched for v -band magnitudes between 13.0 and 13.7, similar to our approach in Sect. 4.2. For the WNE sample, we found two entries, both presumably single stars, WR 126 (WC5/WN) and WR 129 (WN4o). When we conservatively adopt these two targets as single WNE stars, $f_{\text{int}}^{\text{WNE}}$ changes from 0.56 (9 out of 16) to 0.50 (9 out of 18). This difference is smaller by a factor of three than our errors and is hence negligible.

For the WC sample, we found four new entries in the GCWR. Of these, WR 114 (WC5 + OB?: [van der Hucht 2001](#)) and WR 132 (WC6 + ?: [Bisiacchi et al. 1983](#)) are candidate binaries, WR 125 (WC7ed + O9III: [Williams 2019](#); [Arora et al. 2021](#)) is a confirmed binary, and WR 150 (WC5) is a presumably single star. As was the case with the WNEs, accounting for these objects results in $f_{\text{int}}^{\text{WC}}$ that is well within the derived uncertainties.

Therefore, the effect of this bias is not significant given our derived values. This can be understood through multiple reasons. **First, there is a void of massive star-forming regions at distances between about 3 and 8 kpc.** While we may be able to detect WRs in the Carina star-forming region (~ 2.7 kpc), we are unable to detect them in Westerlund 1 (~ 3.8 kpc) because they suffer from large interstellar extinction ([Clark et al. 2005](#)). Second, a notable fraction of WC binaries are dust-producing systems ([Williams 1995](#)) and hence could experience increased circumstellar reddening. This would cause them to be fainter in the V band, which could balance out the increase in brightness due to additional companions.

4.6.3 Implications for binary evolution

According to our current understanding of stellar evolution ([Conti 1976](#); [Meynet & Maeder 2003](#); [Crowther 2007](#)), depending on their initial mass, main-sequence O stars evolve into either cool supergiants or luminous blue variables (LBVs) before becoming WR stars by losing their envelope. Because the spectra of WR stars are thought to reflect the products of fusion in the stellar interiors, the Conti scenario ([Conti 1976](#); [Crowther 2007](#)) proposes a spectroscopic evolution from O stars to the WNL, WNE, WC, and, if they are massive enough, WO phases before these stars end their lives as

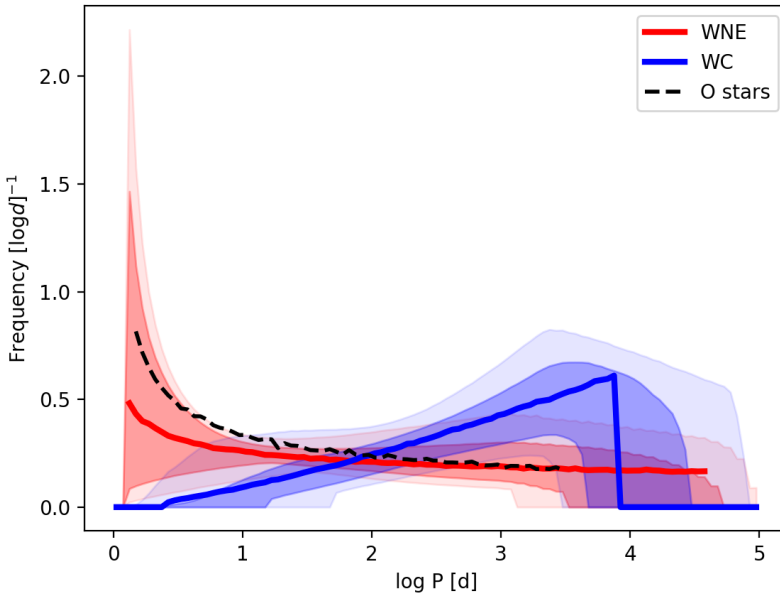


Figure 4.9: Period distributions for main-sequence O stars (dashed black line, from [Sana et al. \(2012\)](#)), WNE stars (red), and WC stars (blue). The WNE and WC distributions are calculated from the posteriors of the MC simulations (Sect. 4.5.2). The posteriors for the WC sample are shown in Fig. 4.8.

compact objects. The focus of this section is to use our new multiplicity constraints on the WC (Chapter 3) and WNE stars to investigate the evolutionary connections between these various categories of objects.

Following the Conti scenario, WNE stars are thought to have evolved from main-sequence O stars via the WNL phase by wind stripping. As discussed before, the multiplicity parameters of the populations of WNE and O stars are congruous within errors (Sect. 4.5.2 and Fig. 4.9). If the population of binary WNE stars is the product of mass stripping in OB star binaries, similarities between their distributions are to be expected. For example, if a $40 M_{\odot}$ star becomes a $20 M_{\odot}$ WNE after transferring its envelope to a companion, the ratio of the pre- and post-interaction period (P_f/P_i) can be determined analytically given assumptions on mass-transfer efficiency and its companion ([Soberman et al. 1997](#)). For the case of a $20 M_{\odot}$ accretor and conservative mass transfer, $P_f/P_i = 1$, while for fully non-conservative mass transfer (assuming material is ejected with the specific angular momentum of the accretor), we have

$P_f/P_i \simeq 0.9$. As an example of a system with an initial mass ratio closer to unity, if the accretor has $35 M_\odot$ at the onset of mass transfer, then $P_f/P_i \simeq 2.1$ for conservative mass transfer, while $P_f/P_i \simeq 2.7$ for the non-conservative case. Therefore, mass transfer will not significantly modify the period distribution of O stars as they evolve into WNEs, which is compatible with the results of Fig. 4.9.

If WC stars are direct descendants of WNE stars, the orbital evolution from the WNE to the WC phase is expected to be mainly governed by mass loss due to their stellar winds. This results in the widening of the orbit, so that a shift to longer orbital periods is expected. To quantify this shift, we considered a $20 M_\odot$ WNE star in a binary system with a $30 M_\odot$ main-sequence O star. Even if the WNE star loses $15 M_\odot$ by the time it becomes a WC star, the orbital period of the system would only change by a factor of two. Therefore, only for WNE binaries in the long-period tail ($P > 500$ d) of the inferred distribution can mass loss lead to orbital periods compatible with the peak of the WC distribution ($P > 1000$ d). If indeed WC stars originate from WNE stars losing mass, then explaining the distributions shown in Fig. 4.9 requires that preferentially longer-period WNE binaries evolve into WC stars, while the shorter-period ones avoid that outcome.

A possibility for the longer-period regime is that we simply do not detect WNE binaries with periods greater than a few thousand days in this current RV campaign. This is shown in Fig. 4.6, where our detection probability drops to 40% at $P \sim 1000$ d and 0% at $P > 10000$ d. The presence of an undetected long-period population of WNE binaries would indeed provide natural progenitors to the long-period WC binary population. The value of $f_{\text{int}}^{\text{WNE}}$ would then be much higher than reported here, however. Almost all of the apparently single WNE stars would be in long-period binaries, resulting in a $f_{\text{int}}^{\text{WNE}}$ close to 1.00.

4.7 Conclusions

We have established the observed and intrinsic multiplicity properties of a complete magnitude-limited sample of 16 northern Galactic WNE stars using data from the HERMES spectrograph since 2017. We measured the RVs using cross-correlation with a statistical framework that allowed us to derive meaningful uncertainties. Adopting a peak-to-peak variability threshold C of 50 km s^{-1} , which is more than three times the observed short-term variability for WR 138, we derived an observed spectroscopic binary fraction, $f_{\text{obs}}^{\text{WNE}}$, of 0.44 ± 0.12 .

Using MC simulations, we determined constraints on a parametrised model of the distribution of orbital parameters. In particular, we considered a distribution described by a power-law index π and upper and minimum values $\log P_{\text{min}}$ and $\log P_{\text{max}}$ for the period distribution, as well as the intrinsic binary fraction $f_{\text{int}}^{\text{WNE}}$. Assuming flat priors

for these model parameters, we found $f_{\text{int}}^{\text{WNE}}$ to be $0.56^{+0.20}_{-0.15}$. The power-law index for the period distribution, π , was found to be $-0.30^{+0.55}_{-0.53}$. Both these values are consistent with what was derived for main-sequence O stars by [Sana et al. \(2012\)](#). Furthermore, the period distribution also favours the majority of systems at orbital periods shorter than 100 d. This is in stark contrast to what we found for the Galactic WC population ($f_{\text{int}}^{\text{WC}} = 0.96^{+0.04}_{-0.22}$, $\pi = 1.90^{+1.26}_{-1.25}$), where the majority of binaries had orbital periods of a few 1000 days. The 68% highest-density interval values of π for the WC and WNE populations do not overlap.

Considering the fact that WNE stars do go on to strip their envelopes and form WC stars ([Meynet & Maeder 2003](#)), understanding the orbital evolution of the WNE population as the stars evolve to the WC phase is critical. The change in the orbital period from the WNE to the WC phase is governed by mass-loss through stellar winds, which is of a factor $\sim 1\text{--}2$. While the long-period WNE binaries could evolve via the LBV phase to form WCs, the descendants of short-period WNE binaries is still a mystery.

The existing multiplicity properties gathered from the literature on a larger sample and the smaller but statistically better-characterised sample presented here seem to indicate that the underlying period distributions for WC and WNE populations are different. This can offer substantial diagnostics on the evolution of these systems. However, owing to the significant evolutionary implications from the above discrepancy, it is critical to increase the sample size of such magnitude-limited studies.

Chapter 5

Multiplicity properties of the Galactic WNL population

The work presented in this chapter is based on:

A spectroscopic multiplicity survey of Galactic Wolf-Rayet stars: III. The northern WNL sequence

K. Dsilva, T. Shenar, H. Sana and P. Marchant

Soon to be submitted to ASTRONOMY AND ASTROPHYSICS.

Author contributions: K. Dsilva performed the data reduction and computed the radial velocities in this chapter with the guidance of H. Sana and T. Shenar. The Monte-Carlo simulations were run by H. Sana. The Bayesian framework was developed by P. Marchant and H. Sana. All the authors assisted with the evolutionary interpretations of the presented results and contributed significantly to the text, which was written by K. Dsilva.

Original abstract:

Massive stars are powerful cosmic engines that have a huge impact on their surroundings and host galaxies. The majority of massive stars will interact with a companion star during their evolution. The effects of this interaction on their end-of-life products are currently poorly constrained. In the phases immediately preceding core-collapse, massive stars in the Galaxy with $M_i \gtrsim 20$ may appear as classical Wolf-Rayet (WR) stars. The multiplicity properties of the WR population are thus required to further our understanding of stellar evolution at the upper-mass end. As the final contribution of a homogeneous radial velocity (RV) survey, this work aims to constrain the multiplicity properties of northern, Galactic, late-type nitrogen-rich Wolf-Rayet (WNL) stars. We compare their intrinsic binary fraction and orbital period distribution to the carbon-rich (WC) and early-type nitrogen-rich (WNE) WR populations from previous works.

We obtained high-resolution spectra of the complete magnitude-limited sample of 11 Galactic WNL stars with the Mercator telescope on the island of La Palma. We used cross-correlation with a log-likelihood framework to measure relative RVs and flagged binary candidates based on the peak-to-peak RV dispersion. By using Monte-Carlo sampling and a Bayesian framework, we computed the three-dimensional likelihood and one-dimensional posteriors for the upper period cut-off ($\log P_{\max}^{\text{WNL}}$), power-law index (π^{WNL}) and intrinsic binary fraction ($f_{\text{int}}^{\text{WNL}}$).

Adopting a threshold C of 50 km s^{-1} , we derived $f_{\text{obs}}^{\text{WNL}} = 0.36 \pm 0.15$. Our Bayesian analysis produces $f_{\text{int}}^{\text{WNL}} = 0.42^{+0.15}_{-0.17}$, $\pi^{\text{WNL}} = -0.70^{+0.73}_{-1.02}$ and $\log P_{\max}^{\text{WNL}} = 4.90^{+0.09}_{-3.40}$ for the parent WNL population. The combined analysis of the Galactic WN population results in $f_{\text{int}}^{\text{WN}} = 0.52^{+0.14}_{-0.12}$, $\pi^{\text{WN}} = -0.99^{+0.57}_{-0.50}$ and $\log P_{\max}^{\text{WN}} = 4.99^{+0.00}_{-1.11}$. The observed period distribution of reported orbital periods of Galactic WN and WC binaries is in agreement with these results. The period distribution of Galactic WN binaries peaks at $P \sim 1 - 10 \text{ d}$ while that of the WC population at $P \sim 5000 \text{ d}$, a shift that cannot be reconciled by orbital evolution due to mass loss or mass transfer. At long periods, the evolutionary sequence O (\rightarrow LBV) \rightarrow WN \rightarrow WC seems feasible. The high frequency of short-period WN binaries compared to WC binaries suggests that they either tend to merge, or that the WN components in such binaries rarely evolve into WC stars in the Galaxy.

5.1 Introduction

Classical WN stars with very thick, dense winds can appear as WNL stars. However, very-massive main-sequence stars can also appear as WNL sub-types.

Table 5.1: The 11 WNL stars in our RV monitoring campaign with the number of spectra, time baseline of coverage and average S/N per resolution element at 5100 Å.

WR#	Spectra	Time coverage (d)	S/N
108	11	1140	125
120	7	385	30
123	8	387	60
124	10	577	50
134	15	2901	170
136	39	2907	280
148	20	1161	110
153	49	2858	200
155	85	3075	140
156	18	797	70
158	13	1031	70

Late-type Wolf-Rayet stars of the nitrogen sequence (WNL) stars can either be classical (hydrogen-depleted, post main sequence) or very-massive main sequence (hydrogen burning) stars. It is challenging to differentiate between the two, although the main-sequence WNL stars are generally more luminous (and more massive) than classical WNL stars (Hamann et al. 2019). In this chapter, we focus on the analysis of the remaining 11 WNL stars in our sample. We find that the multiplicity properties of the WNL population are consistent with the WNE population from Chapter 4, and so we perform a combined analysis by comparing the multiplicity properties of the Galactic WN population to those of the WC population from Chapter 3. The sample, data reduction and normalisation are briefly explained in Sect. 5.2. The RV analysis is discussed in Sect. 5.3. Our results are presented in Sect. 5.4 and discussion in Sect. 5.5. We present our conclusions in Sect. 5.6.

5.2 Sample and data reduction

We select WNL stars observable with the Mercator telescope ($\delta > -30^\circ$ and $V \leq 12$ mag). As a reminder, entries in the GCWR listed as ‘WN5-6’ were considered to be WN5 for simplicity. The data reduction procedure for our spectra is described in detail in Chapters 2 and 4. We discuss the selection biases in Sect. 5.5.2. The number of spectra and time coverage for the 11 WNL stars in our sample is shown in Table 5.1.

The normalisation process is described in Chapters 3 and 4. In order to normalise the spectra in a homogeneous fashion and to minimise the human systematics, we used a normalised WNL model spectrum from the Potsdam Wolf-Rayet code (Gräfener et al.

2002; Todt et al. 2015) to identify pseudo-continuum regions around 8100 Å in the red and 5100 Å in the blue. We then anchored a continuum WNL model to the red and applied a reddening to fit the spectrum in the blue. After exploring various reddening laws, we concluded that they did not affect the homogeneity of the normalisation process. We therefore decided to use the reddening law from Fitzpatrick (2004a).

5.3 Radial velocity measurements

As in Chapters 3 and 4, we decided to use cross-correlation to measure RVs for the stars in our sample. An implicit assumption of cross-correlation is that the template is an accurate representation of the data. Therefore, the choice of template is of importance. Because stellar atmospheric models usually do not accurately reproduce the complex line profiles of WR spectra, and the line profiles cannot be reproduced by Gaussian or Lorentzian functions, we decided to construct and use a high signal-to-noise (S/N) spectrum as a template. We briefly go over the methodology and assumptions below.

5.3.1 Cross-correlation to measure radial velocities

The cross-correlation function (CCF) is a convolution of the template with the data, and is described using a log-likelihood function. The RV of an epoch is measured by maximising this function, and the uncertainty can be derived from maximum log-likelihood theory. The measured RVs are then used to create a co-added spectrum, which is in the rest frame of the initial template. The co-added spectrum is then used to re-measure the RVs. This iterative process is continued until the measured RVs do not change within their measurement errors. One caveat of this method is that the measured RVs are relative to an epoch, and not absolute. This is not a problem when probing RV variations to identify binary candidates (as in this work) but an absolute shift must be applied when combining them with RVs from the literature.

5.3.2 Wind variability and its effect on radial velocity measurements

Comparing the WNL stars in our sample to the WCs (Chapter 3) and WNEs (Chapter 4), we observe significantly more variability in the WNL line profiles. This is not unexpected, since strong line-profile variability has been observed in WNL stars before (St-Louis et al. 2009; Chené & St-Louis 2011; Michaux et al. 2014; Chené et al. 2020). This directly increases the measurement uncertainties on the RVs, as the assumption of the template reproducing the data partially breaks down. Aside from correcting for

observational biases, it is also important to understand the effect of such variability on the RV measurements.

In order to reduce the effect of wind-variability on RV measurements, we selected spectral lines that were the least affected by spectral variability for each star. We used lines of He II, N III, N IV and in some cases, N V to measure RVs. Additionally, for each star we used the combination of all the above-mentioned masks and called it ‘full spec’. The final masks for each object are indicated in Appendix. C.2. In Chapters 3 and 4, we obtained high-cadence data of the long period binaries WR 137 and WR 138 away from their periastron passages. This allowed us to quantify the amplitude of such variability on the RV measurements in WC and WNE stars, which were found to be ~ 5 and $\sim 15 \text{ km s}^{-1}$ respectively.

In this work, we focused on WR 136 which has a spectral type of WN6b(h). Although it is classified as a SB1? system in the GCWR with a period of 4.5 d (Koenigsberger et al. 1980; Aslanov & Cherepashchuk 1981), there is no derived orbit for this system. Further studies with photometry (Moffat & Shara 1986) and polarimetry (Robert & Moffat 1989) failed to confirm this period. We chose WR 136 for this purpose **due to the lack of a long-period binary** in our sample. Assuming it is a single star, we obtained high-cadence data with HERMES over two periods. We first procured 18 spectra over 16 days in August of 2019. Second, we obtained between three and six epochs within a night on seven occasions between August and October of 2019. This resulted in a total of 87 high-cadence spectra.

We used lines of He II, N III, N IV, N V and Balmer lines to measure RVs for WR 136. The RV dispersion can be seen in Fig. 5.1. The observed RV dispersion comprises of a statistical part (i.e. the measurement errors, σ_p) and contribution from wind-variability (σ_w , see Eq. 3.13). By measuring σ_{RV} and σ_p , we get an upper limit on the wind variability. For each mask, values of $(\sigma_{\text{RV}}, \sigma_w)$ are indicated in Fig. 5.1. We find that **RVs measured using** lines of He II are less affected by wind variability as compared to N V $\lambda 4945$. One possible reason is that the N V $\lambda 4945$ line is a very weak line in the spectrum of WR 136, limiting its RV accuracy. In any case, the trend of He II lines showing greater stability than lines of nitrogen is unusual, demonstrating that each WR star is unique. The RV amplitudes for the masks are similar to what was found in Koenigsberger et al. (1980), although we do not find the same period reported by them after analysing the data with a Lomb-Scargle periodogram (Lomb 1976; Scargle 1982). **Due to the small RV amplitude and lack of coherent periods, we consider WR 136 to be a single star.** We use diagnostic plots such as Fig. 5.1 for each object to select an appropriate mask to measure RVs. These are indicated in Appendices C.1 and C.2.

Table 5.2: Radial velocity measurements for our sample of WNL stars together with an overview of their known multiplicity properties. ΔRV and σ_{RV} are calculated in this work and are used to identify tentative spectroscopic binaries. The spectral types are taken from the GCWR unless indicated otherwise, with ‘d.e.l.’ implying the dilution of emission lines and ‘a’ indicating the presence of absorption lines. The binary status of this work is reported based on the spectroscopic observations.

WR#	Spectral Type (GCWR)	Binary Status (GCWR)	Binary Status This work	Period (d)	e	ΔRV (km s $^{-1}$)	σ_{RV} (km s $^{-1}$)	$\Delta RV > C$
108	WN9ha	a, d.e.l.	-	-	-	15.7	5.0	no
120	WN7o	-	-	-	-	40.5	15.7	no
123	WN8o	SB1?, no d.e.l.	SB	-	-	57.1	18.2	yes
124	WN8h	SB1?, no d.e.l.	-	-	-	19.3	5.9	no
134	WN6b	SB1?, no d.e.l.	-	-	-	29.6	9.3	no
136	WN6b(h)	SB1?, no d.e.l.	-	-	-	15.4	3.0	no
148	WN8h+	SB1, d.e.l.	SB	4.317336 \pm 0.000026 d ^(a)	0 (fixed) ^(a)	171.8	54.5	yes
153	WN6o/CE+O3-6 + B0:I+B1:V-III	SB2 + SB2	SB	6.6887 ^(b)	0.0 ^(b)	576.6	150.3	yes
155	WN6o+O9II-1b	SB2	SB	1.6412436 ^(c)	0.034 \pm 0.008 ^(c)	609.5	212.0	yes
156	WN8h	d.e.l.	-	-	-	16.1	4.4	no
158	WN7h	d.e.l.	-	-	-	15.0	4.1	no
3.6	no							

^(a) (Muñoz et al. 2017), ^(b) fixed from photometry, Demers et al. (2002), ^(c) Marchenko et al. (1995) fixed period

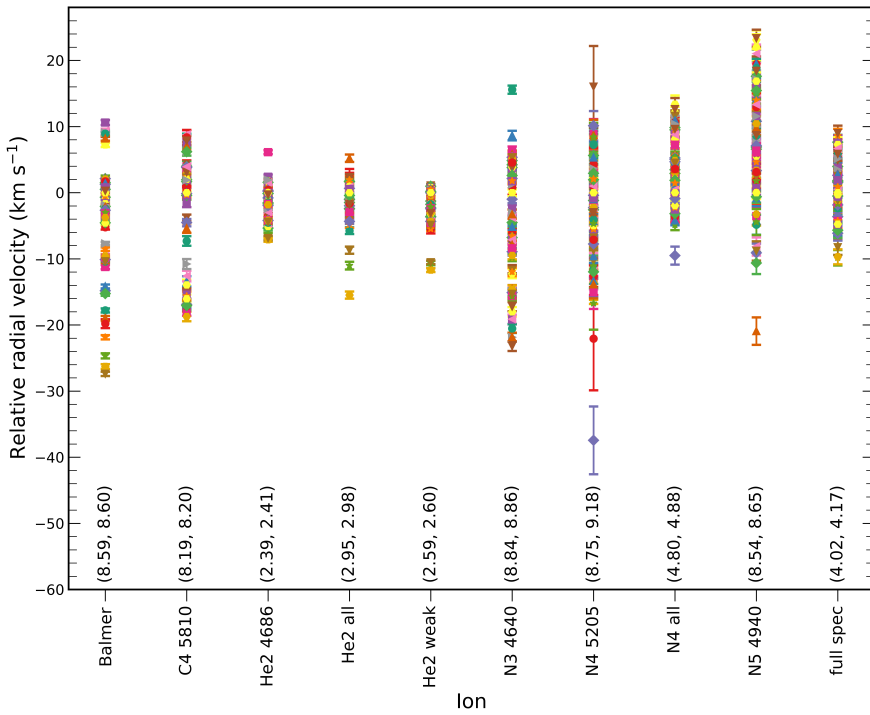


Figure 5.1: High-cadence RV measurements for WR 136 over a variety of masks. In brackets at the bottom are values of (σ_w, σ_{RV}) (km s^{-1}). As there are 87 data points for each mask, the legend has been omitted for clarity.

5.4 Results

5.4.1 Observed binary fraction and detection probability

After measuring the RVs, we computed the peak-to-peak amplitude (ΔRV) for each object. We chose a threshold C above which we attributed the observed ΔRV to Doppler motion in a binary system. Figure 5.2 is a non-parametric threshold plot that shows the observed binary fraction as a function of the chosen threshold. By moving right to left, we attribute the RV amplitude of these stars to Doppler motion, and classify them as candidate spectroscopic binaries.

In principle, the chosen threshold should be high enough to avoid false positives due to intrinsic variability. The high-cadence study on WR 136 demonstrated that with the

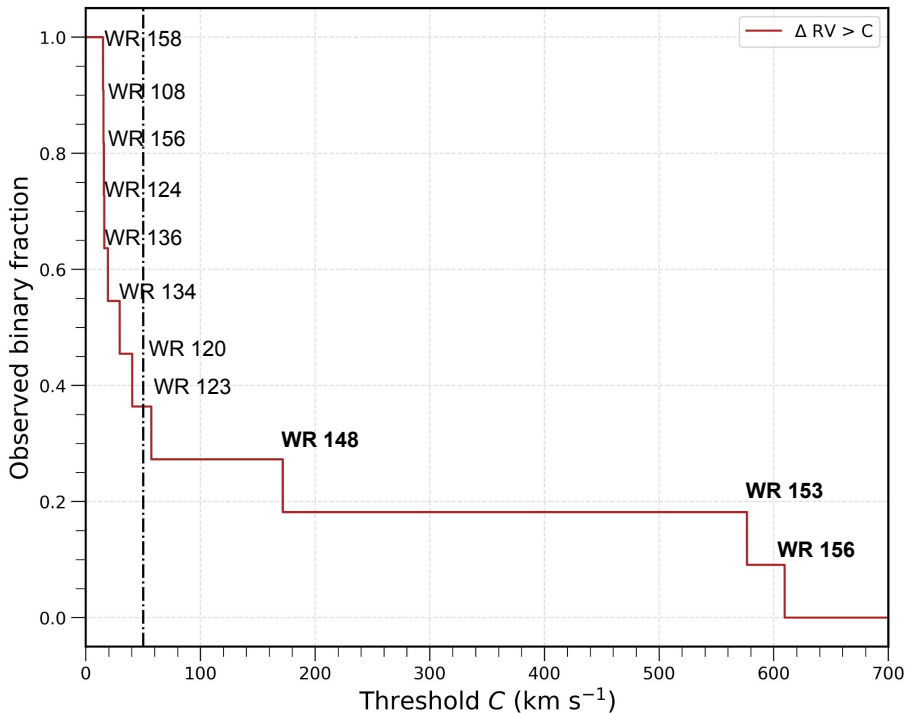


Figure 5.2: Non-parametric threshold plot showing the observed binary fraction as a function of the threshold C . The adopted threshold of 50 km s^{-1} is shown by the dotted-dashed vertical line. The entries in bold are confirmed spectroscopic binaries in the literature.

appropriate mask, the measured peak-to-peak RV amplitude due to intrinsic variability is $\sim 15 \text{ km s}^{-1}$. This is similar to what was found for the N v lines in WR 138 (Chapter 3). Therefore, we adopt a similar strategy and chose a threshold that is at least three times larger than the peak-to-peak intrinsic variability, at $C = 50 \text{ km s}^{-1}$. This results in the classification of 4 out of 11 stars as RV variable objects for which binarity is likely the cause. This corresponds to an observed binary fraction ($f_{\text{obs}}^{\text{WNL}}$) of 0.36 ± 0.15 .

5.4.2 Multiplicity properties: WNL population

We perform a Bayesian analysis with MC simulations with a method developed in Chapter 4 to formally account for the observational biases. The ideal solution is to calculate the likelihood of the observed RV time series for each object based on

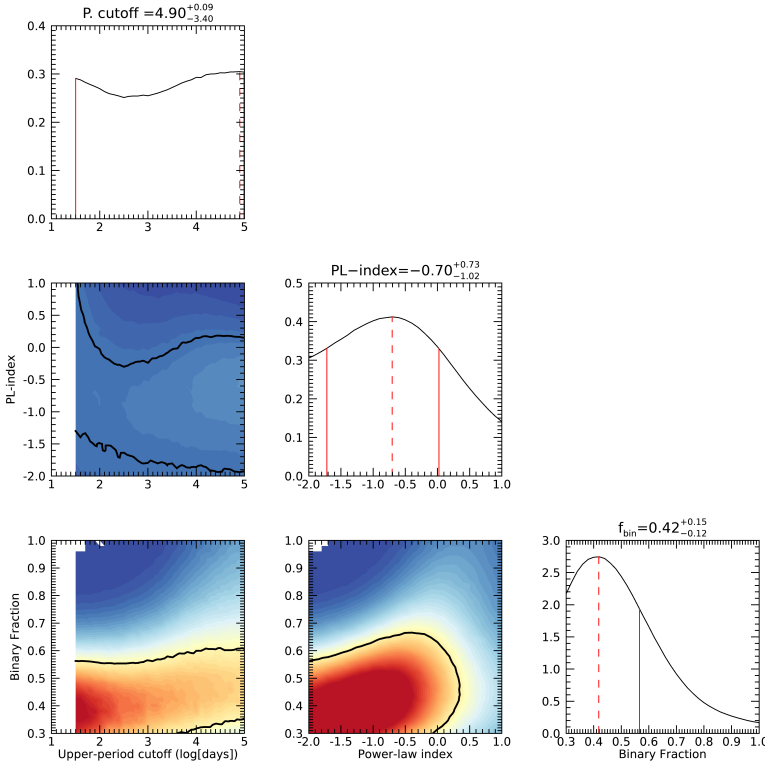


Figure 5.3: Three-dimensional likelihood over $\log P_{\max}^{\text{WNL}}$, $f_{\text{int}}^{\text{WNL}}$, and π^{WNL} for the Galactic WNL population. Assuming flat priors, the one-dimensional posteriors are also shown. For each posterior, the solid red lines show HDI68, and the dashed red line shows the mode.

the sampling and possible binary properties of the system. However, this is too computationally intensive, and instead we divide the objects into multiple ΔRV bins and try to reproduce them with our simulations. The ΔRV bins are: $\Delta\text{RV} < 50 \text{ km s}^{-1}$ (7 objects), $50 \leq \Delta\text{RV} < 250 \text{ km s}^{-1}$ (2 objects), $250 \leq \Delta\text{RV} < 650 \text{ km s}^{-1}$ (2 objects), $\Delta\text{RV} \geq 650 \text{ km s}^{-1}$ (no objects).

The parameters included in the model for the population with binaries are the period distribution, intrinsic binary fraction, inclination, eccentricity, mass ratio, time of periastron passage and the orientation of the binary system in three-dimensional space. The period distribution is characterised by the minimum period ($\log P_{\min}^{\text{WNL}}$), maximum period ($\log P_{\max}^{\text{WNL}}$) and the power-law index (π^{WNL}). The power-law index π determines the shape of the distribution of binaries with orbital periods P as follows

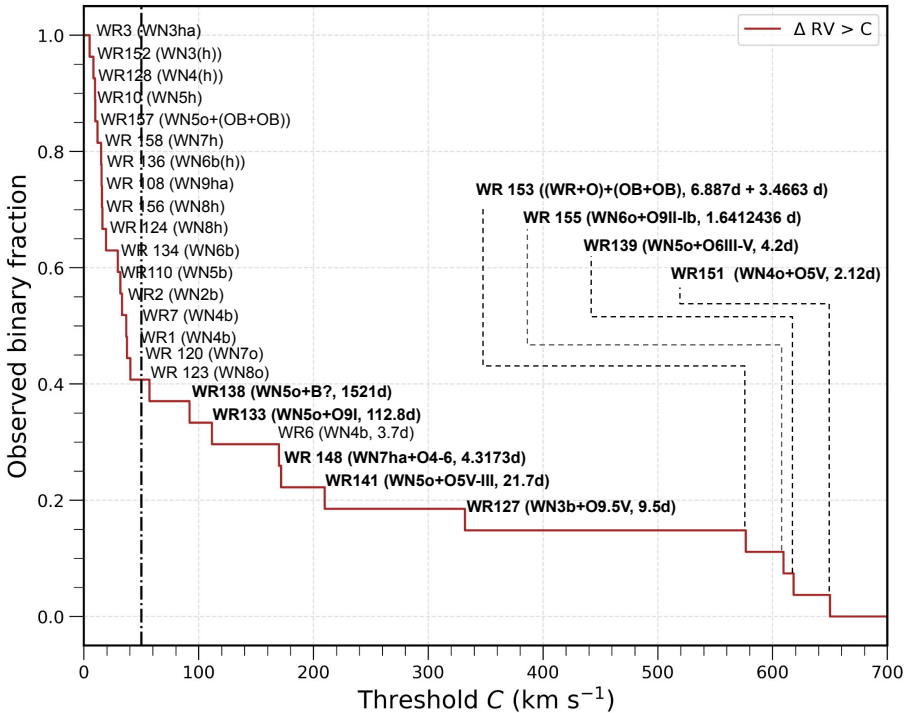


Figure 5.4: Same as Fig. 5.2 but for the 27 WN stars (16 WNE + 11 WNL) in our sample. The threshold $C = 50 \text{ km s}^{-1}$ is shown by the vertical dotted-dashed line. Entries in bold represent confirmed spectroscopic binaries in the literature.

$$p(\log P) \sim (\log P)^\pi. \quad (5.1)$$

Along with the period distribution, we include the intrinsic binary fraction, $f_{\text{int}}^{\text{WNL}}$, as a model parameter. The eccentricities are drawn from a flat distribution between 0.0 and 0.9, with random inclinations, times of periastron passage and three-dimensional orientations of the orbital planes. Given the presence of very short-period binaries in the WNL sample, we fixed the value of $\log P_{\text{min}}^{\text{WNL}}$ at 0.15 [d] (approximately 1 d). We explored values of $\log P_{\text{max}}^{\text{WNL}}$ from 1.5 to 5.0 [d] in steps of 0.1 dex, π^{WNL} from -2.0 to 1.0 in steps of 0.1 and $f_{\text{int}}^{\text{WNL}}$ from 0.30 to 1.00 in steps of 0.02. We also use prior information on the known orbital periods for those classified as binaries (Table 5.2), and require at least three objects with $1 < P < 10 \text{ d}$.

With the framework set up, we simulated 10 000 sets of 11 WNL stars for each $P - M_2$ grid point, resulting in almost 4×10^8 populations. We calculated the three dimensional

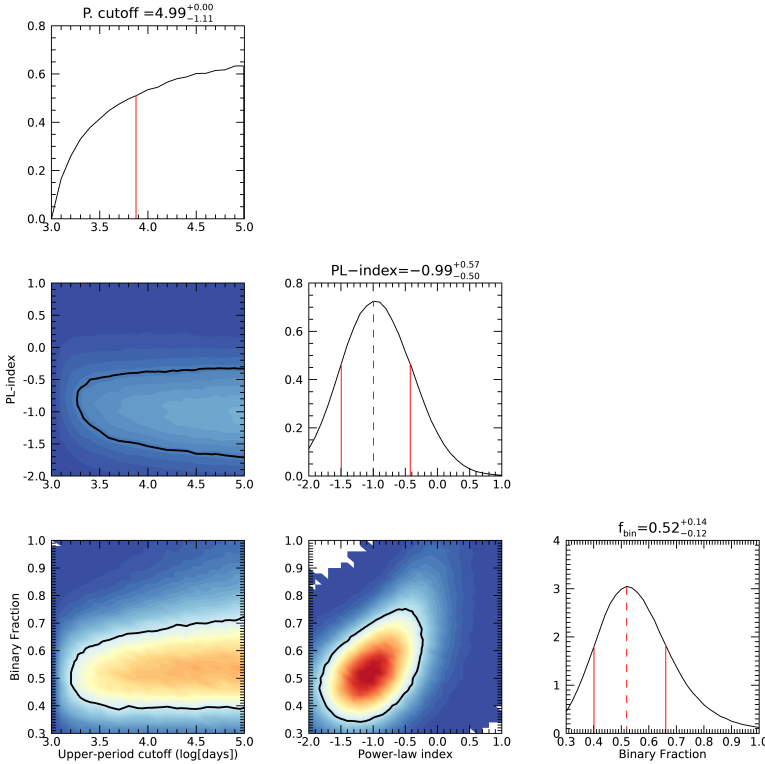


Figure 5.5: Same as Fig. 5.3 but for the combined (WNE + WNL) Galactic WN population.

likelihood of reproducing the observed distribution of objects in ΔRV bins. Assuming flat priors on $\log P_{\max}^{\text{WNL}}$, π^{WNL} and $f_{\text{int}}^{\text{WNL}}$, we computed their marginalised posterior likelihoods (Fig. 5.3). We computed the 68% credible intervals for each posterior (the highest density interval, HDI68). For the three model parameters, our posteriors yield values of $f_{\text{int}}^{\text{WNL}} = 0.42^{+0.15}_{-0.12}$, $\pi^{\text{WNL}} = -0.70^{+0.73}_{-1.02}$ and $\log P_{\max}^{\text{WNL}} = 4.90^{+0.09}_{-3.40}$ [d] for the parent WNL population. The value of $\log P_{\max}^{\text{WNL}}$ is set by the upper limit of the grid due to the lack of long-period constraints introduced by the orbital bins, as a result of no confirmed WNL binaries at $P > 10$ d.

The derived multiplicity properties are in agreement with those of the Galactic WNE population (Chapter 4). An interesting difference is that of the upper-period cutoff, which is better constrained for the WNE population ($\log P_{\max}^{\text{WNE}} = 4.60^{+0.40}_{-0.77}$) given the prior information on the presence of long-period binaries. We do not have such constraints for the WNL population, with the only orbital periods that are constrained

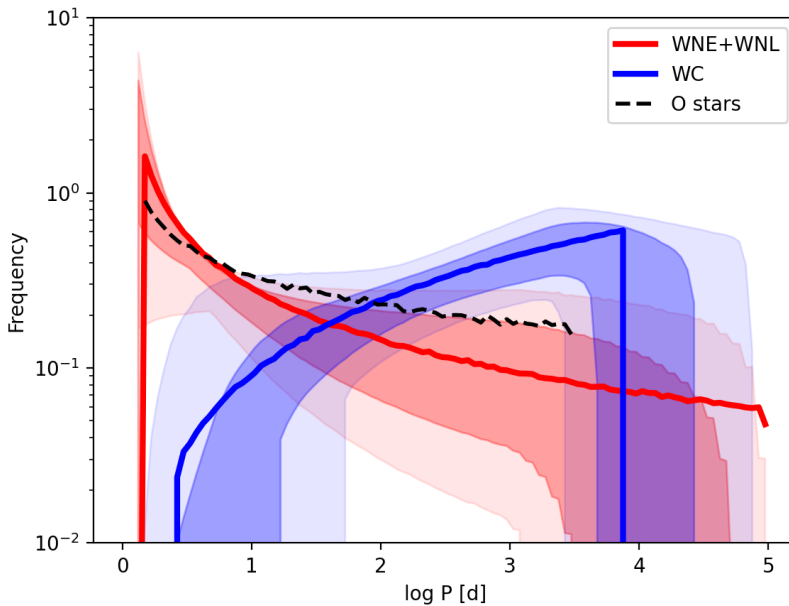


Figure 5.6: Visualisation of the 10^7 period distributions created by sampling the posteriors from Fig. 5.5. The light- and dark-red regions depict 95% and 68% of all distributions. The solid red line is the distribution created with the best-fit values from the posteriors. The blue regions and lines are the same for the WC population from Chapter 4. The dashed black line is the period distribution for O stars from Sana et al. (2012).

in the literature are less than 10 days (Table 5.2). This results in a large HDI₆₈ for $\log P_{\max}^{\text{WNL}}$, which is reconcilable with $\log P_{\max}^{\text{WNE}}$ within the credible intervals.

The negative power law index for the WNL sample indicates a preference for binary systems with shorter orbital periods. This is similar to what was found for the WNE (Chapter 4) and O-type populations (Sana et al. 2012). The lower cut off for the orbital period distribution ($\log P_{\min}^{\text{WNL}}$) is fixed at 0.15 [d] in order to account for the presence of binaries with periods as short as 1.6 d in our sample. The similarities with respect to the WNE population are indicative that the overall multiplicity properties of the Galactic WN population are consistent. We therefore combine the WNE and WNL populations and perform a similar Bayesian analysis.

5.4.3 Multiplicity properties: combined WN population

After merging the data sets of the 16 WNE stars in Chapter 4 and the 11 WNL stars in this paper, we ended up with 27 Galactic WN stars. Based on their ΔRV values, we created Fig. 5.4, similar to Fig. 5.2, depicting $f_{\text{obs}}^{\text{WN}}$ as a function of the threshold C . The characteristic kink in the curve can be seen around 50 km s^{-1} , differentiating RV variation due to Doppler motion and intrinsic variability, thereby reaffirming our choice of threshold. We therefore constrained the observed binary fraction for the WN sample to be $f_{\text{obs}}^{\text{WN}} = 0.41 \pm 0.09$.

We performed a Bayesian analysis on the combined WN sample with the same underlying assumptions for the distributions stated in Sect. 5.4.2. We divided the sample into various ΔRV bins as follows: $\Delta\text{RV} < 50 \text{ km s}^{-1}$ (16 objects), $50 \leq \Delta\text{RV} < 250 \text{ km s}^{-1}$ (6 objects), $250 \leq \Delta\text{RV} < 650 \text{ km s}^{-1}$ (6 objects), $\Delta\text{RV} \geq 650 \text{ km s}^{-1}$ (no objects). Similarly, we also defined minimum orbital period bins based on what is known for the sample: $P > 1 \text{ d}$ (10 objects), $P > 10 \text{ d}$ (3 objects), $P > 100 \text{ d}$ (2 objects) and $P > 1000 \text{ d}$ (1 object). The three-dimensional likelihood, along with the one-dimensional posteriors computed by assuming flat priors are shown in Fig. 5.5. As compared to Fig. 5.3, the power-law index (π^{WN}) becomes more negative and $f_{\text{int}}^{\text{WN}}$ on the WN population increases due to the contribution from the WNE sample.

The derived multiplicity properties for the WN sample were used to construct a visualisation of the period distribution. Similar to Chapter 4, we sampled 10^7 sets of parameters from the posteriors in Fig. 5.5 and used them to create orbital period distributions. The density cloud representing these distributions can be seen in red in Fig. 5.6. The period distribution constructed using the best-fit parameters is shown with a solid red line. We also plotted the density cloud of distributions for the Galactic WC population in blue (Chapter 4). The period distribution for main-sequence O stars is shown with a dashed-black line (Sana et al. 2012).

5.5 Discussion

5.5.1 Comparison with the literature

In order to verify if what is observed is in agreement with our results, we investigated the literature to consider WR stars beyond those included our sample. Since the objects from VDH01 have been thoroughly analysed for binarity, we focus on this subset of WR stars. The catalogue contains 87 WC stars and 127 WN stars, of which 78 are WNL stars. Of these 78 objects, 21 are classified as spectroscopic binaries and 14 currently have orbital solutions. Of these, only one has a period larger than 100 days.

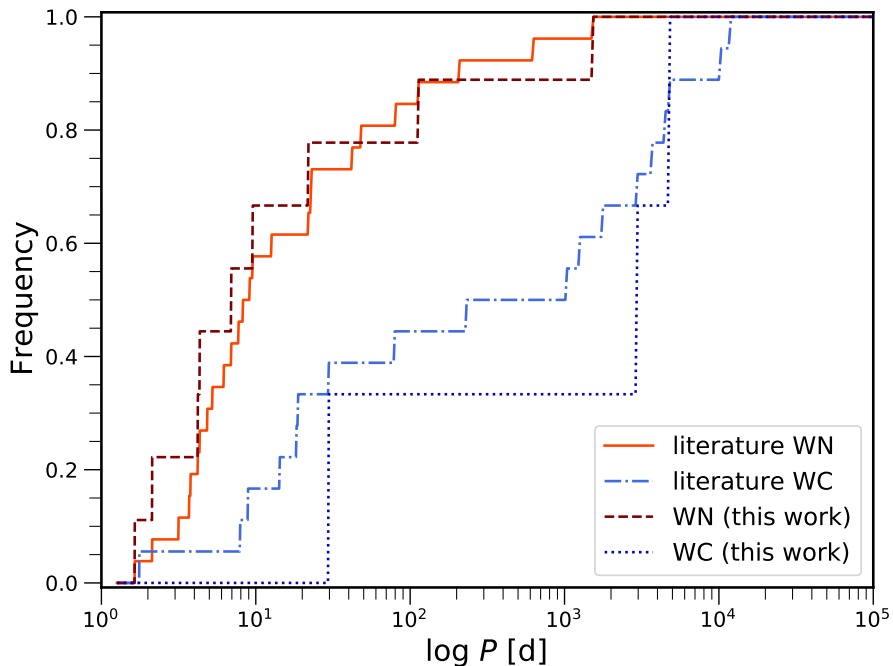


Figure 5.7: Cumulative distribution of the reported orbital periods from the literature for the Galactic WN (solid red) and WC (dashed-dotted blue) populations. The observed distributions based on spectroscopic periods from our sample are also plotted, with the WN (dashed red) and WC (dotted blue) binaries.

The total number of Galactic WN binaries with known orbital periods is 28. Combining this with the 18 known orbital periods for Galactic WC binaries, we constructed the cumulative observed orbital period distribution with the distribution from our sample over-plotted (Fig. 5.7). While a few WC binaries have periods shorter than 10 d, this fraction is still much smaller than that of short-period WN binaries. This shows that the analysed samples are representative of the Galactic WR population.

5.5.2 Observational biases due to the limiting magnitude

Another potential observational bias introduced by the conditions of the RV campaign is that of the limiting magnitude. Because WR stars are generally faint in the optical, the selection criteria of $V \leq 12$ inherently favours binaries. [Vanbeveren & Conti \(1980\)](#)

demonstrated this clearly for the Large Magellanic Cloud, although this effect is not dominant in the Galaxy due to the large spread in the distances.

Similar to what was done in Chapter 4, we assumed that the companion contributes to around 50% of the flux in WR + OB system (e.g., [Shenar et al. 2019](#)). Therefore, WR binaries would be twice as bright as single WR stars on average. To account for this bias, we need to account for single WR stars between 12.0 and 12.7 mag. In cases where the V -band magnitude was missing, we searched for v -band magnitudes between 13.0 and 13.7.

We found five single WNL entries in that range: WR 58 (WN4b/CE), WR 63 (WN7o + OB), WR 82 (WN7(h)), WR 130 (WN8(h)), and WR 131 (WN7h+abs). Although WR 63 and WR 131 could be considered candidate binaries, no evidence of a companion has been found in the literature, and hence we conservatively consider them to be single stars. Including these stars in our sample would change the intrinsic binary statistics, from 5 binaries out of 11 WNL stars to 5 binaries out of 16 WNL stars. This would result in a binary fraction of 0.31, which is within our credible interval.

5.5.3 Consequences on binary evolution

Depending on their mass, main-sequence O stars are thought to evolve into either red supergiants or luminous blue variables (LBVs) before becoming WR stars, after which they are expected to collapse to form compact objects ([Conti 1976](#); [Meynet & Maeder 2003](#); [Crowther 2007](#); [Langer 2012](#)). In this section, we use our derived multiplicity properties for the Galactic WN and WC populations to infer possible connections between the evolutionary stages before collapse. As the multiplicity properties of the WNL and WNE populations are compatible, we discuss the WN population as a whole.

Linking the O and WN populations

As indicated in Fig. 5.6, the orbital period distributions of O stars and WN stars is in excellent agreement. This is not surprising, given that WN stars can be formed by the envelope stripping of the primary by the secondary in an OB binary. Using the analytical expressions from [Soberman et al. \(1997\)](#), it is possible to calculate the change in the orbital period due to mass transfer. Depending on the mass-ratio of the OB binary, mass transfer does not increase the orbital period by more than a factor of three, irrespective of the mass-ratio and the conditions for mass transfer. For example, conservative mass transfer in a $40 + 30 M_{\odot}$ binary where the primary transfers $20 M_{\odot}$ would have an increase in the period (P_f/P_i) of factor 1.7. Therefore, the increase in the orbital period would not shift the distribution drastically, which is in accordance with what we find.

A possible exception where binary interaction can significantly reduce the orbital period is common envelope evolution, triggered by mass transfer in systems with extreme mass ratios or after the donor has developed a deep convective envelope (see, e.g. the review by [Ivanova et al. 2013](#)). However, envelope ejection is energetically disfavored unless interaction happens after the star becomes a red supergiant (e.g. [Klencki et al. 2021](#)), but this phase is potentially not reached by the most massive stars as it would require evolution beyond the Humphreys-Davidson limit ([Humphreys & Davidson 1979](#); [Davies et al. 2018](#); [Gilkis et al. 2021](#)).

Depending on their initial mass, massive stars are also thought to go through the LBV phase during their transition from main sequence O stars to the WN phase. Multiplicity studies on the LBV population indicate a binary fraction of 0.70 ± 0.09 , with the majority of them at periods of a year or longer ([Mahy et al. 2022](#)). The multiplicity properties of the LBVs seem inconsistent with the large number of short period WN binaries that is found both in our sample and in the GCWR (Fig. 5.7). However, this could just be a consequence of shorter period systems being too compact to fit an LBV star, leading an O star to fill its Roche lobe before reaching that evolutionary phase. This would imply that the progeny of the LBV binary population are the WN binaries with $P > 1$ yr.

Evolution from the WN to WC populations

The biggest discrepancy between the orbital period distributions for both the observed (Fig. 5.7) and intrinsic (Fig. 5.6) populations is the glaring lack of WC binaries at short periods. Because WN stars are expected to evolve into WC stars by further stripping their envelope, the change in their orbital parameters is governed by wind or binary mass loss. This results in an increase of the orbital period by a factor of $\sim 1.5\text{--}2$. Therefore, this implies that only WN binaries with $P > 100$ d would preferentially evolve into WC binaries. In the short period regime of $P < 10$ d, only a small fraction of WN binaries might become WC binaries.

One possibility for WNE stars in short period binaries to avoid evolving into WC binaries requires that they are unable to strip their envelopes further before reaching core collapse, for example, due to reduced mass loss rates (possible implications from [Neijssel et al. 2021](#)). Why would this only affect WN binaries with short periods and not the entire population is unclear. Another possibility is that short period WN binary systems undergo interaction before they can reach the WC phase. The cause of this interaction could potentially be the expansion of the WN star due to inflation ([Gräfener et al. 2012](#); [Sanyal et al. 2015](#); [Grassitelli et al. 2018](#); [Ro 2019](#)). While it is unclear if inflation happens in nature, and how an inflated donor star would respond to mass transfer, an unstable mass transfer phase resulting in a merger could prevent short period WN stars from evolving into WC binaries. Conversely, if such mass transfer

episodes are stable, they would result in further stripping, leading to more short period WC stars and worsening the discrepancy in the period distributions.

Additionally, in systems undergoing wind-wind collisions, slowed outflows may potentially interact with the binary and be ejected with additional angular momentum, leading to a contraction of the orbit and possibly a merger. For example, MacLeod & Loeb (2020) showed how the interaction of colliding winds with the stars in equal mass main sequence binaries could lead to a shrinkage of the orbit. Depending on the ratio of the orbital velocity to the wind velocity, this effect could also occur to WN binaries. Whether this scenario provides a valid explanation remains to be shown.

A final possible scenario could be that the O star companion fills its Roche lobe before the WN evolves into a WC, but the likelihood of it happening during the short-lived WNE phase is too small for this to be the predominant explanation for the lack of short period WC systems.

Due to the duration and sampling of the RV campaign, it is also possible that there is a population of long-period binaries ($P > 1000$ d) that we do not detect. This is because the intrinsic variability of WN stars is larger than that of the WC, making it challenging to detect low RV amplitudes. Therefore, it could be that the progenitor population of long-period WC binaries is simply undetected. However, this would imply that for the Galactic WN population the value of $f_{\text{int}}^{\text{WN}}$ is close to 1.00, as most (all?) the apparently single WN stars would then reside in long-period binary systems.

A large fraction of the main sequence O population are in hierarchical triple systems (e.g., Sana et al. 2014; Moe & Di Stefano 2017). Mass loss due to stellar winds or binary stripping, among other things, will cause the ratio of the inner and outer separation to change. If the stripping of the primary by the secondary resulted in a WN + OB binary, then the nature of mass transfer and evolution of the inner orbit determines the stability of the triple. When this ratio changes beyond a critical point, the system becomes dynamically unstable. This could result in the disruption of the triple, or a merger of the inner binary (Toonen et al. 2020).

In the case of mass loss through stellar winds, the dynamically unstable phase can last from thousands to millions of years (Toonen et al. 2022). Although the most common outcome predicted is the preservation of the triple hierarchy, it is also common for the system to be disrupted with one of the stars ejected. In case of an ejection, the resulting orbit has a period of the order of 10^3 - 10^5 d (Toonen et al. 2022). As an example in a hierarchical triple, if the inner WN + OB binary was formed through a combination of stripping via stellar winds and mass transfer, it could be dynamically unstable. An ejection could result in the formation of a WN + OB binary in a wide orbit, where the WN star would go on to evolve and become a wide WC + OB binary. Detailed simulations involving the formation of the WR star, mass transfer and stellar winds are required to investigate the frequency and feasibility of this channel.

5.6 Conclusions

With a homogeneous, magnitude-limited spectroscopic monitoring of 11 northern Galactic WNL stars, we measured relative RVs using cross-correlation and found $f_{\text{obs}}^{\text{WNL}} = 0.36 \pm 0.15$. Using a Bayesian framework around MC simulations, we derived a fraction corrected for observational biases ($f_{\text{int}}^{\text{WNL}} = 0.62^{+0.16}_{-0.17}$). We observed that the computed intrinsic multiplicity properties for the Galactic WNL population are congruous with those derived for the WNE population in Chapter 4.

We combined the WNE and WNL samples and simulated $\sim 15 \times 10^9$ populations of 27 WN stars. We found the intrinsic multiplicity properties for the Galactic WN population to be similar to those derived for main-sequence O stars in Sana et al. (2012). We constructed the orbital period distribution for Galactic WNs and noted the peak at $P < 5$ d. The abundance of short period WN binaries can be explained through Case A or Case B mass transfer in O binaries. Short-period WN binaries can also form via common envelope evolution through late Case B or Case C mass transfer, irrespective of the mass-ratio. However, it is observationally non-trivial to distinguish between the multitude of channels.

From the intrinsic multiplicity properties of the Galactic WC population (Chapter 3), we see a clear lack of short-period WC binaries, with the orbital period distribution peaking at $P \sim 5000$ d. The lack of short-period WC binaries is also supported by the literature. While there are a few known, their number is lacking compared to their WN counterparts, despite the fact that the number of WNs and WCs in the Galaxy are similar. The discrepancy in distributions is not only found in our simulations (Fig. 5.6) but can also be seen in the observed period distribution of Galactic WR binaries (Fig. 5.7). Orbital evolution via mass loss from the WN to WC phase cannot explain the shift towards longer periods.

The multiplicity properties of Galactic LBVs (Mahy et al. 2022) seems to be in agreement with that of the long-period O, WN and WC binary populations. This could imply that, at long periods, the evolutionary channel of O \rightarrow LBV \rightarrow WN \rightarrow WC might exist. However, the evolution of the short-period WN binaries is still an enigma. Invoking exotic channels such as common-envelope evolution and dynamical interactions in triples could explain their evolution, but they are highly uncertain. Further observational and theoretical studies are required to understand their importance in the grand scheme of binary evolution.

As the immediate progenitors of black holes, the multiplicity properties of WR stars directly affect those for black hole binaries (e.g. through black-hole kicks in a core-collapse scenario), and hence the predictions for gravitational-wave progenitors. Expanding the sample size of magnitude-limited studies is critical to understand the binary evolution of massive stars.

Chapter 6

Summary and future work

6.1 Summary

In this thesis, we investigated the intrinsic multiplicity properties, namely the binary fraction and properties of the orbital-period distribution for the Galactic WN and WC population. We did this by undertaking a spectroscopic monitoring campaign over about five years for a magnitude-limited sample of northern, Galactic WR stars using the HERMES spectrograph mounted on the Mercator telescope on the island of La Palma. For the HERMES spectrograph, we developed a method to correct the pipeline-produced scientific spectra for the instrumental response. Furthermore, we measured RVs for the objects in our sample using a cross-correlation method allowing us to properly quantify the uncertainty on the measurements. We further investigated the effects of wind-variability on RV measurements for different spectral sub-types of WR stars. We quantified the observed binary fraction for the WC, WNE and WNL objects in our sample by measuring their RV variability amplitudes. Finally, we used Monte-Carlo simulations with a Bayesian framework to correct for observational biases and constrain the intrinsic multiplicity properties of the parent population.

In Chapter 2, we developed the instrumental response correction for the HERMES spectrograph as an improvement to the current data-reduction pipeline. We first used the publicly-available code Molecfit to correct the calibration spectra for telluric contamination. Following this we divided it by a model SED from GSSP and applied a median filter to get the instrumental response. We corrected all of the WR spectra for telluric contamination with Molecfit and applied the correction for the instrumental response. The shape of the resulting spectra then resembled the spectral energy distribution. We used scaled continuum models from the model-atmosphere code

PoWR and applied an interstellar reddening to then normalise the spectra. In this way the normalised spectra, and hence RV measurements, were not affected by human systematics.

In Chapter 3, we analysed spectroscopic time series of 12 Galactic WC stars with at least six epochs obtained over 2-8 years. We measured relative RVs using cross-correlation with a maximum log-likelihood framework in order to derive accurate uncertainties on our measurements. Furthermore, we measured RVs using high-cadence data for WR 137, a known long-period binary, away from periastron to quantify the effect of intrinsic variability. Using C IV lines, we found an upper limit of 3 km s^{-1} due to variability in the wind. After measuring the values of ΔRV , we found 7 out of 12 stars showing RV variations more than 10 km s^{-1} and classified them as candidate binaries, resulting in an observed binary fraction of 0.58 ± 0.14 . Finally, we showed using MC simulations that the intrinsic multiplicity of Galactic WC stars is at least 0.72 with periods up to 10^5 d .

In Chapter 4, we analysed the 16 WNE stars in our sample with at least six epochs obtained over 3-8 years. We found that the spectra of WNE stars have larger line-profile variability than WC stars on average. Based on the high-cadence data of the long-period binary WR 138, we were able to quantify the peak-to-peak variability using N V lines to be 15 km s^{-1} . Furthermore, we used lines of N V to measure RVs for most of the objects in our sample and derived ΔRV values for them. We chose a threshold of 50 km s^{-1} and found an observed binary fraction of 0.44 ± 0.12 . We developed a Bayesian framework around MC simulations to correct for observational biases and found that the majority of WNE binaries have orbital periods between 1 and 10 days with a binary fraction of $0.56_{-0.15}^{+0.20}$. Moreover, the derived multiplicity properties are similar to what is found for Galactic O stars and can be explained with our current understanding of binary evolution. We also revisited the 12 WC stars from Chapter 3 and found that the majority of WC binaries exist with orbital periods between 1000 and 10 000 days with a binary fraction of $0.96_{-0.22}^{+0.04}$. The multiplicity properties of both the WC and WNE populations are consistent with what is observed in the Galaxy, reaffirming that our selected samples are representative of the whole population.

Finally, in Chapter 5, we analysed a sample of 11 WNL stars with at least six epochs obtained over 4-8 years. As observed in the literature, we found that WNL stars have larger line-profile variability than WNE and WC stars. Due to the lack of a long-period binary in our sample, we analysed the apparently single star WR 136 with high-cadence data to study the effects of wind variability on RV measurements. We found an amplitude of 15 km s^{-1} by measuring RVs using lines of He II. WR 136 is the only object in our entire sample of 39 WR stars where the variability in He II is less than other lines of higher ionisation, demonstrating once again that every WR star is unique. We adopted a threshold of 50 km s^{-1} and found the observed binary fraction to be 0.36 ± 0.15 . After correcting for observational biases, we find the intrinsic binary fraction to be $0.42_{-0.17}^{+0.15}$. The properties of the period distribution are consistent with

what is found for the WNE sample, allowing us to perform a combined analysis of the WN sample. We found the intrinsic binary fraction to be $0.52^{+0.14}_{-0.12}$ with a majority of binaries having periods less than 10 days. This is in contrast with the Galactic WC population with very long period binaries. According to the Conti scenario, WN stars are the descendants of WC stars and so these binary populations must also be connected. The high-frequency of short-period WN binaries and lack of WC counterparts suggests that these systems avoid evolving into WC binaries. Two possible explanations for this are mergers, or that the WN star does not reach the WC phase in such systems. Similarly, the apparent lack of long-period WN binaries raises the question about the progenitors of long-period WC binaries. As orbital evolution from the WN to the WC phase is governed by mass-loss, this change in the period is irreconcilable. A tempting explanation is that we do not detect long-period WN binaries, their natural progenitors, because low-amplitude RV variations are masked by wind-variability. If this were the case, then the intrinsic binary fraction of the WN population would jump to ~ 1.00 , similar to that of the WC population.

Before proceeding to the future work, let us take a moment to reexamine the questions posed in Sect. 1.3. We found that the binary fraction of the Galactic WN population is $0.52^{+0.14}_{-0.12}$, while that of the Galactic WC population is $0.96^{+0.04}_{-0.22}$. These populations both have binaries with periods up to 10^5 d. The discrepancy in the observed period distributions in the Galaxy seems to be real, since even after correcting for observational biases, we find the majority of WNs to reside in short-period binaries and that of WCs to reside in long-period binaries. If all short-period WNs were to fail to become WCs, then the Conti scenario is strongly affected by multiplicity. However, the role of mergers, particularly further evolution of the merger product, is unclear.

6.2 Future work

6.2.1 Expanding the sample

The work presented in this thesis is the largest homogeneous analysis for multiplicity in Galactic WR stars. Given the extremely short lifetime of the WR phase, expanding such studies to a larger fraction of the 667 Galactic WR stars is crucial to understand the effects of multiplicity on the evolution of these stars. In order to probe long-period binaries, part of the sample presented in this work will be monitored on a long-term basis with HERMES.

The southern Galactic sample

The natural follow-up to this study would be to complement it with a sample of southern Galactic WR stars. Given how optically faint most WR stars are, using facilities with the capability to probe fainter V -band magnitudes would be a logical next step. To prepare for this, we have already acquired between 3 and 6 epochs of spectra for 63 WR stars in the southern hemisphere using the High Resolution Spectrograph mounted on the South-African Large Telescope (SALT). A similar analysis can be performed on this data-set, although one point of concern would be the homogeneity of the normalisation and its impact on RV measurements, since the method developed here cannot be applied to SALT data in a straightforward manner.

Interferometry to probe longer periods

One of the potential explanations for the progenitors of long-period WC binaries is the presence of undetected long-period WN binaries. Given the period regime, interferometry is a better-suited technique to hunt for these systems (Sect. 1.2.2). We have already applied for a large programme at the European Southern Observatory (ESO) to acquire a snapshot of southern Galactic WR stars. This data can be complemented with a similar data-set from the northern hemisphere. For this purpose, we have acquired data of 6 WR stars with the Center for High Angular Resolution Astronomy (CHARA) array. Analysis of these data-sets and correcting them for observational biases is the next step forward.

6.2.2 An improved Bayesian analysis

The Bayesian analysis in this work attempts to find the likelihood of reproducing the objects in our sample in various ΔRV bins based on certain input parameters. A first step could be to incorporate the mass-ratio as an additional parameter, but this would currently take too much computational time. Other parameters can also be included in such a way, given an increase in the sample. However, for each object one would ideally calculate the likelihood of observing a particular RV timeseries based on various input parameters. This would provide a deeper insight onto the possible orbital configurations and mass-ratios of the WR binary population.

6.2.3 Orbital analysis of WR binaries

Aside from expanding monitoring surveys, efforts must be made to increase the number of WR binaries with derived orbital solutions. Orbital analysis allows us to infer

dynamical masses and radii of the components in a model-independent manner. This is a powerful technique which can be combined with model-atmospheric analysis to lift some of the degeneracy (e.g. in Richardson et al. 2016; Richardson et al. 2021). The eccentricity of such binary systems can also be derived, which is a critical quantity when trying to understand formation scenarios and further evolution. The goal of the long-term HERMES monitoring programme is also to sample the known binaries appropriately in phase such that their orbits can be improved.

Lastly, Gaia DR3 and DR4 will detect a large number of astrometric binaries and provide accurate astrometric solutions. For example, almost 200 OB + BH binaries expected to be detected with Gaia DR3 (Janssens et al. 2022). Therefore it is possible that a few tens of WR binaries are also detected.

In conclusion, the work presented in this thesis attempts to address some of the open questions with respect to the effects of multiplicity on massive star evolution. The results presented in this thesis raise many questions on the evolutionary connection between WN and WC binaries. The upcoming future is promising, with a lot of different perspectives with which the multiplicity of WR stars can be probed.

Appendix A

Appendix for Chapter 3

A.1 Comments on specific objects

WR 4: According to the seventh catalogue of WR stars (van der Hucht 2001), WR 4 is classified as a WC5+?, an SB1 with no observable line dilution or absorption effects. Photometric variability with a period of 4.3 days (Moffat & Shara 1986) was determined. Rustamov & Cherepashchuk (1989) found both a photometric and spectroscopic period of 2.4096 days with a peak-to-peak amplitude of $\sim 60 \text{ km s}^{-1}$, but we can safely reject the presence of such large amplitude RV variation in our data set (Table 3.2) questioning the fact that the 2.4 d period traces an orbital motion. We therefore do not include WR 4 in the list of short-period binaries in our literature study (Sect. 3.4.2).

In a study of co-rotating interaction regions (CIRs), St-Louis et al. (2009) classified WR 4 as ‘Not Variable’ in the weak C iv 5016 Å line. Chené & St-Louis (2011) further elaborated that the maximum line-profile variability was 1.2% of the level of flux in the line, hence making it ineligible to be a CIR candidate. In this work, we obtained 22 epochs over a time coverage of 890 days, out of which about 12 were observed within two nights, attempting a probe on shorter periods. Although we do not report a short period, the adopted choice of our threshold allows us to classify it as a binary (Table 3.2). Further monitoring of this system is required to determine the orbital period of this system.

WR 5: van der Hucht (2001) reports WR 5 as a single star with spectral type of WC6. No emission was found in the X-rays (Skinner et al. 2006; Güdel & Nazé 2009). In this work, WR 5 is found to have a ΔRV of 4.9 km s^{-1} over 718 days with a σ_{RV} of 1.7 km s^{-1} for RVs measured using the full spectrum. It does not pass our binary

detection criterion and is, therefore, classified as presumably single.

WR 111: WR 111 is a presumably single WC5 star (Niemela et al. 1999; van der Hucht 2001). It has been studied with spectral analyses and hydrodynamical studies (Gräfener et al. 2002; Gräfener & Hamann 2005; Sander et al. 2012), and was used to show for the first time that WC winds can be explained through radiation-driven mass loss. In this work, WR 111 shows a peak-to-peak variability of 4.5 km s^{-1} over 742 days with a σ_{RV} of 1.5 km s^{-1} . It does not pass our binary detection criterion and is therefore classified as a presumably single star.

WR 113: WR 113 is a WC8d+O8-9 binary system first identified by Massey & Niemela (1981) with a period of about 29.707 days in a circular orbit. A debate about the eccentricity arose when Niemela et al. (1996) derived similar orbital parameters with a significant eccentricity ($e = 0.19$). The matter was resolved by David-Uraz et al. (2012), who showed that the two were indistinguishable solutions and adopted a circular orbit and was later confirmed by Hill et al. (2018) with a period of 29.700 ± 0.001 d. In this work, WR 113 has the largest ΔRV and σ_{RV} of 282.6 and 93.9 km s^{-1} respectively, passing our binary detection criterion. The RV measurements phased with the orbital period are shown in Fig. 3.7.

WR 117: According to the GCWR, WR 117 is classified as a WC9d, which is a dust producing star. Sander et al. (2012) find it to be a bit too hotter than most WC9 counterparts, even suggesting it might be in the WC8 parameter regime. Williams et al. (2005) did not find any evidence for an OB-type companion, and hypothesize that WR 117 might be an evolved WC9 star. A large scatter in photometric magnitudes was observed by Williams (2014) with possible 0.5 mag eclipses due to dust. In this work, WR 117 shows a ΔRV of 4.9 km s^{-1} and a σ_{RV} of 1.9 km s^{-1} over a coverage of 488 days and is hence classified as a presumably single star.

WR 119: WR 119 is classified as a single WC9d star according to the GCWR. Fahed et al. (2009) studied it using V and I band photometry, finding a larger than normal variability in these bands. Desforges et al. (2017) performed a temporal variance spectrum analysis over timescales of days to weeks and found significant variability in the C III 5696 Å line. In this work, we find values of ΔRV and σ_{RV} of 11.0 and 3.2 km s^{-1} respectively, resulting in WR 119 being classified as a binary.

WR 135: WR 135 is an apparently single WC8 star (GCWR). Previous RV studies have failed to determine any variability (Niemela et al. 1999), nor even photometric variability (Moffat & Shara 1986). In this work, we find a ΔRV of 4.7 km s^{-1} and σ_{RV} of 1.6 km s^{-1} over a baseline of 2660 days, classifying it as a presumably single star.

WR 137: WR 137 is a well-studied, long-period binary system with a late-type WC star and a late-type O star (WC7pd + O9 V; p: peculiar, d: dust producing). Marchenko et al. (1999) reported dust production in 1997 September - 1998 May and Williams et al. (2001) derived a period of 13.05 ± 0.15 years by tracking the periodic dust formation.

This period was verified by the orbital analysis using RVs by Lefèvre et al. (2005), who found the maximum emission from dust to occur just after the periastron passage. The orbit was recently resolved using interferometry with CHARA (Richardson et al. 2016), reiterating the importance of long term RV monitoring campaigns in identifying WR binaries. The broad emission lines of the WR star are superimposed by a narrow emission and an absorption component, making the companion star a prime candidate to be an Oe star. The RVs measured in this campaign are in agreement with those obtained from the literature (Fig. 3.4).

WR 140: WR 140 is classified as a (WC7pd + O5.5fc) system with a well established spectroscopic (Fahed et al. 2011) and visual (interferometric; Monnier et al. 2011) orbit ($P=7.938$ years, $e=0.8996$). These parameters were derived by combining archival data along with measurements during the 2009 periastron passage. An improved derivation of the masses and orbital parameters using spectroscopic and interferometric data from the 2016 December periastron passage makes it one of the most accurately constrained masses for a WR binary system to date (Thomas et al. submitted). In this work, WR 140 has a ΔRV of 21.6 km s^{-1} and a σ_{RV} of 6.5 km s^{-1} , which passes our binary detection criterion. The RV measurements along with archival data are shown in Fig. 3.7.

WR 143: WR 143 is classified as a binary system (WC4 + Be; Varricatt & Ashok 2006), who detected the presence of hydrogen emission lines and He I lines in the infrared spectrum. In the optical spectra, a hint of this is seen in H α , with features similar to those exhibited by WR 137. We detect significant RV variability over our 76 d baseline and thus classify WR 143 as a binary ($\Delta\text{RV} = 11.2 \text{ km s}^{-1}$, $\sigma_{\text{RV}} = 4.2 \text{ km s}^{-1}$).

WR 146: WR 146 is a visual binary with a spectral classification of WC5 + O8. The components show non-thermal radio emission (Dougherty et al. 1996) and were resolved with HST images (Niemela et al. 1998). The computed mass loss rate for WR 146 is much higher than prototypical WC5 stars, prompting a debate on the multiplicity of the O-star companion (Dougherty et al. 2000). An X-ray study by Zhekov (2017) shows a discrepancy in the mass-loss rate by a factor of 8 to 10. Given the angular separation, Niemela et al. (1998) suggest binary periods of hundreds of years. However, our 847 day baseline with values for ΔRV and σ_{RV} of 18.9 and 5.9 km s^{-1} suggest periods of the order of 3000 d (Fig. A.2) for a massive companion. Further monitoring is required to constrain the orbit.

WR 154: WR 154 is classified as a single WC6 star (GCWR). In this work, we do not detect significant RV variation. However, given the short baseline (24 days), we cannot rule out the possibility of it being a long period binary as the detection probability of our campaign drops significantly for periods above 100 d (Fig. A.2).

A.2 Relative RV measurements

Relative RVs for the objects in our sample, measured with the full spectrum as a mask. The reference epoch is marked with a ‘*’. The Barycentric Julian Date (BJD) is given as the middle of the exposure. The average S/N is given in Table 3.1.

Table A.1: Journal of the HERMES observations for WR 4

BJD – 2450000 (d)	Relative RV (km s^{-1})	σ_p (km s^{-1})
7961.7217	1.39	0.12
8088.5764*	0.00	0.13
8103.4795	-3.18	0.10
8712.7295	2.32	0.10
8719.6991	0.95	0.09
8740.6337	0.08	0.11
8779.4835	0.52	0.09
8779.4945	0.39	0.09
8779.5055	0.57	0.09
8779.5165	1.41	0.09
8779.5275	0.86	0.09
8784.6062	0.99	0.17
8784.6276	1.62	0.16
8784.6490	1.71	0.12
8784.6705	2.20	0.12
8784.6919	2.51	0.12
8796.5122	3.44	0.11
8798.5655	0.02	0.12
8799.5284	-6.57	0.62
8804.6853	-7.21	0.60
8821.4885	3.53	0.12
8852.3716	17.67	0.11

Table A.2: Journal of the HERMES observations for WR 5

BJD – 2450000 (d)	Relative RV (km s ⁻¹)	σ_p (km s ⁻¹)
8086.5338	-2.36	0.11
8103.4889	-4.88	0.09
8721.7268	-1.05	0.08
8742.6913	-0.75	0.11
8756.7129*	0.00	0.08
8789.6356	-4.21	0.28
8804.7296	-1.57	0.09

Table A.3: Journal of the HERMES observations for WR 111

BJD – 2450000 (d)	Relative RV (km s ⁻¹)	σ_p (km s ⁻¹)
7881.5925	2.59	0.06
7900.5403	-0.63	0.07
8249.7094*	0.00	0.04
8276.6582	2.81	0.05
8276.6760	2.27	0.06
8598.6858	4.23	0.05
8621.6290	0.14	0.11
8623.5349	2.93	0.05

Table A.4: Journal of the HERMES observations for WR 113

BJD – 2450000 (d)	Relative RV (km s ⁻¹)	σ_p (km s ⁻¹)
904.7122	265.36	0.46
7909.5689	117.86	1.10
7910.6482	95.97	0.74
8254.6411	249.11	0.23
8255.6767	259.04	0.18
8276.6878*	0.00	0.27
8580.7046	240.54	0.34
8582.7191	262.29	0.26
8632.5666	-17.27	0.29

Table A.5: Journal of the HERMES observations for WR 117

BJD – 2450000 (d)	Relative RV (km s ⁻¹)	σ_p (km s ⁻¹)
8254.7002	2.45	0.44
8255.7058*	0.00	0.33
8701.3976	4.52	0.36
8742.4328	1.86	0.39

Table A.6: Journal of the HERMES observations for WR 119

BJD – 2450000 (d)	Relative RV (km s ⁻¹)	σ_p (km s ⁻¹)
7906.7165	10.97	0.25
7908.6325	6.35	0.26
7911.5561	4.93	0.26
8282.6811*	0.00	0.12
8283.5768	0.74	0.19
8723.4382	7.27	0.22
8727.4160	5.99	0.34

Table A.7: Journal of the HERMES observations for WR 135

BJD – 2450000 (d)	Relative RV (km s ⁻¹)	σ_p (km s ⁻¹)
6119.7192	-2.94	0.06
6119.7247	-2.92	0.06
6119.7301	-2.88	0.06
7309.4567*	0.00	0.04
7310.3944	-1.73	0.05
7900.7233	-1.14	0.04
7935.6002	-1.54	0.05
8197.7621	1.30	0.05
8206.7455	-1.81	0.05
8267.5912	-1.45	0.04
8276.7069	-1.72	0.04
8276.7155	-1.79	0.04
8629.7216	-2.82	0.04
8663.7244	-0.31	0.05
8719.5508	1.60	0.09
8779.4288	-3.12	0.06

Table A.8: Journal of the HERMES observations for WR 137

BJD – 2450000 (d)	Relative RV (km s^{-1})	σ_p (km s^{-1})
6125.6634	17.28	0.17
6889.6039	-1.07	0.13
7324.4165	-5.66	0.12
7902.7153	-4.62	0.16
7938.6925	-7.84	0.16
7951.5912	-6.72	0.18
8195.7661	-4.58	0.17
8206.7607	-3.57	0.16
8265.6372	-5.00	0.16
8629.7139	-0.47	0.13
8664.7263	2.19	0.13
8705.5661	0.02	0.10
8706.6067	0.68	0.09
8707.5508	0.32	0.12
8708.4941	-0.37	0.08
8709.4256	0.24	0.10
8710.5560	0.76	0.10
8712.5473	0.09	0.10
8713.5166	0.35	0.11
8714.4978	-0.27	0.09
8715.5106	0.40	0.12
8716.5440*	0.00	0.12
8717.5925	0.22	0.16
8718.4792	-2.96	0.83
8719.4324	-3.19	0.82
8720.4046	1.66	0.18
8721.5327	-1.56	0.10
8779.4381	0.53	0.15

Table A.9: Journal of the HERMES observations for WR 140

BJD – 2450000 (d)	Relative RV (km s ⁻¹)	σ_p (km s ⁻¹)
6118.7347	-4.89	0.17
6890.5970	-14.41	0.22
7896.7053	6.86	0.13
7902.6990	7.19	0.12
7938.6987	5.63	0.13
8195.7710	3.58	0.13
8207.7645	3.94	0.12
8262.6720	1.16	0.12
8277.7089*	0.00	0.10
8608.7327	-1.83	0.16
8666.6980	-3.24	0.16
8680.5209	-4.25	0.20
8799.4178	-8.28	0.23

Table A.10: Journal of the HERMES observations for WR 143

BJD – 2450000 (d)	Relative RV (km s ⁻¹)	σ_p (km s ⁻¹)
8723.5075	6.39	0.37
8727.5533	6.74	0.41
8759.5106*	0.00	0.43
8775.3291	-1.09	0.59
8775.3505	-1.15	0.62
8799.4685	-4.49	1.53

Table A.11: Journal of the HERMES observations for WR 146

BJD – 2450000 (d)	Relative RV (km s ⁻¹)	σ_p (km s ⁻¹)
7912.6682	-3.55	0.67
7938.7179	-11.18	1.41
7948.7207	-8.07	1.64
8201.7401	-4.40	0.35
8310.6838	7.67	0.75
8740.4677	-1.98	0.40
8741.5211	-1.94	0.40
8759.3867*	0.00	0.38

Table A.12: Journal of the HERMES observations for WR 154

BJD – 2450000 (d)	Relative RV (km s^{-1})	σ_p (km s^{-1})
8762.6141	-2.13	0.10
8763.5412	-3.41	0.11
8775.5248	-1.75	0.11
8786.5511*	0.00	0.13

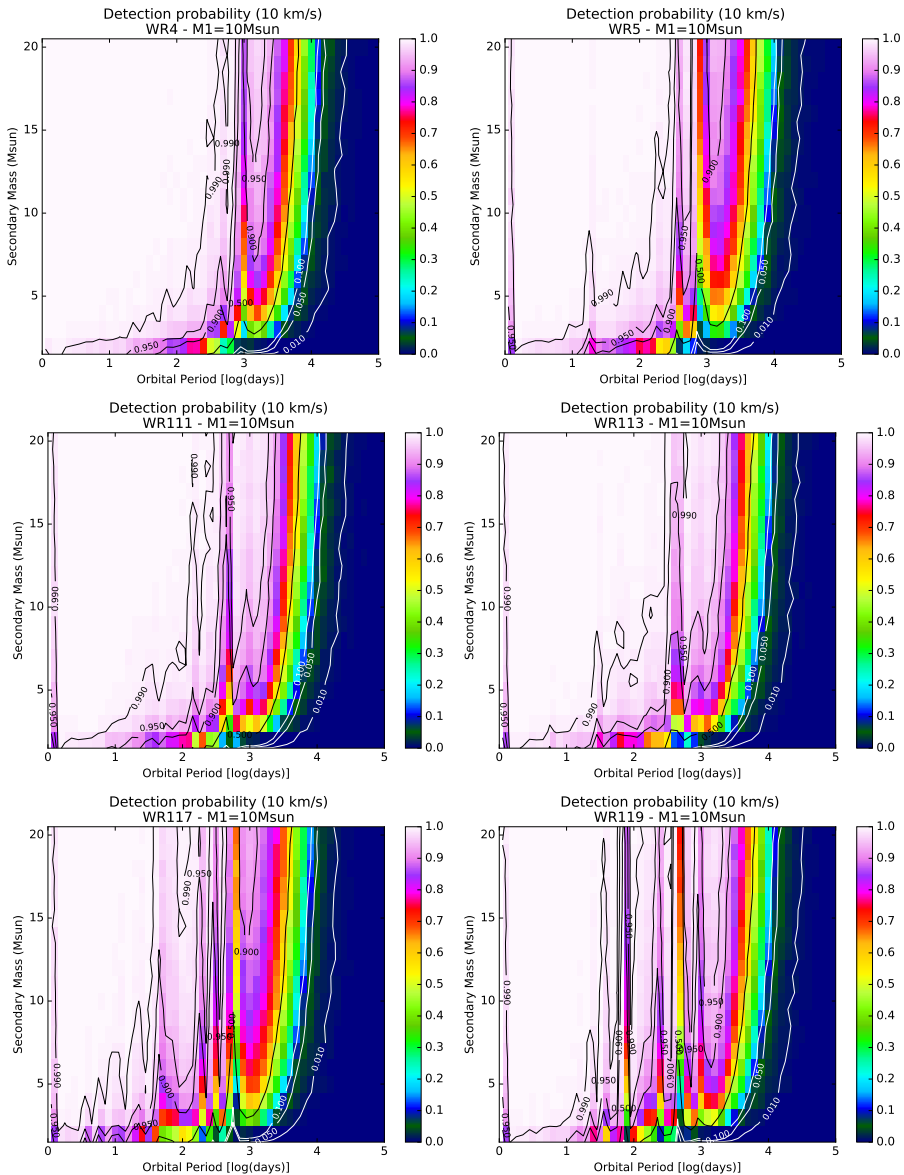


Figure A.1: Binary detection probability of the observational campaign for the various stars in our sample, adopting a minimum RV variability threshold of 10 km s^{-1}

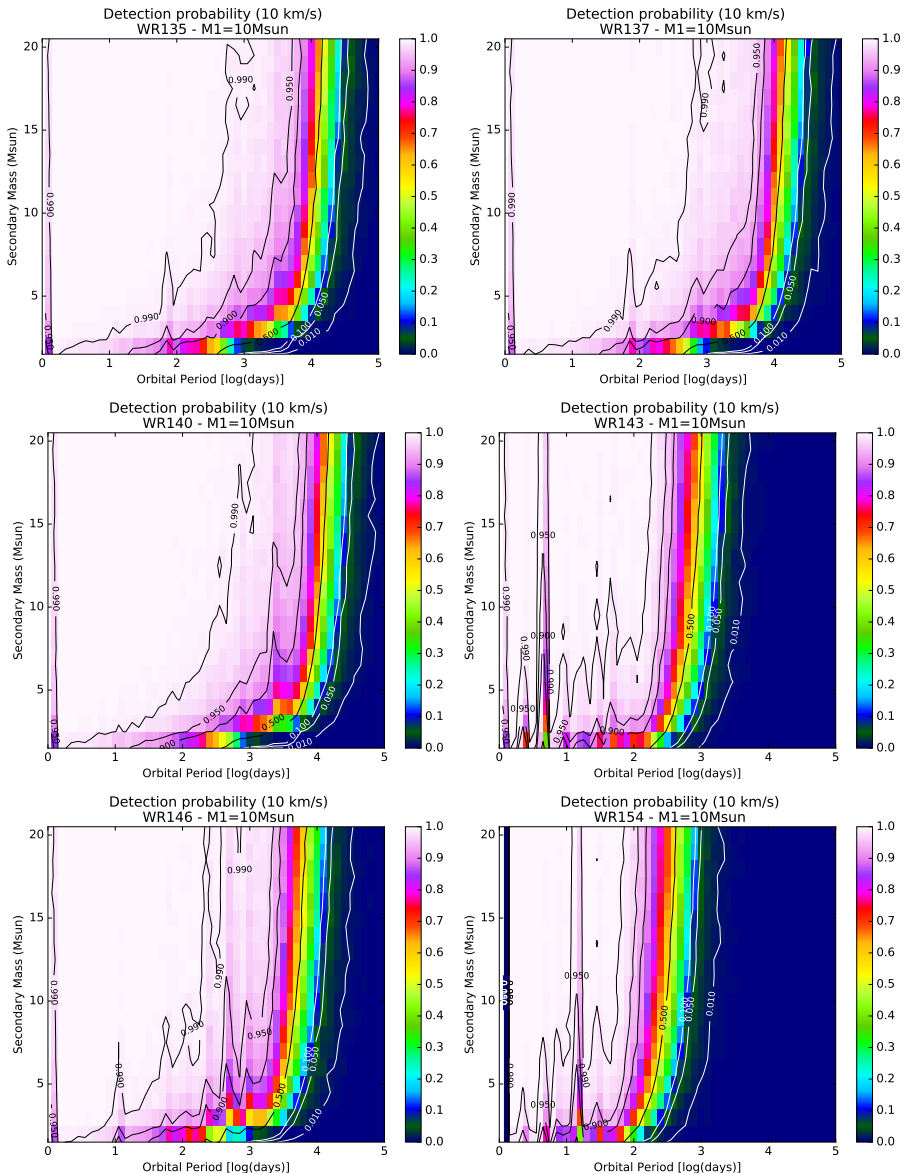


Figure A.2: Binary detection probability of the observational campaign for the various stars in our sample, adopting a minimum RV variability threshold of 10 km s^{-1}

Appendix B

Appendix for Chapter 4

B.1 Comments on specific objects

WR 1: According to the GCWR, WR 1 is classified as an SB1?. [Marchenko et al. \(1998b\)](#) found a variety of photometric periods with Hipparcos, but settled on the ‘best’ value of 11.68 ± 0.14 d. As a follow-up, [Morel et al. \(1999\)](#) studied the variability of the different line profiles and measured centroid velocities of He II $\lambda 4686$. They concluded that a non-degenerate companion causing this line-profile variability on short timescales would have to be luminous enough to be seen in the spectrum (either in spectral lines or through line dilution, which is not the case). They were unable to rule out the possibility of a compact object as a companion. Even though the X-ray emission from WR 1 is variable ([Wessonowski & Niedzielski 1996](#)), the amount of X-rays is normal for its spectral type.

Extensive studies of the line-profile variability were undertaken by [Flores et al. \(2007\)](#) and [Chené & St-Louis \(2010\)](#), who found periods of 7.684 d and $16.9^{+0.6}_{-0.3}$ d, respectively. They both concluded that the periodicity was intrinsic to the stellar wind and not due to orbital motion. [Chené & St-Louis \(2010\)](#) proposed corotating interaction regions (CIRs) as the best scenario to explain their photometric and spectroscopic results. This was further supported by a spectropolarimetric study by [St-Louis \(2013\)](#), who found continuum polarisation at the level of 0.5% for WR 1, indicating a large-scale structure in the wind. In this work, we find WR 1 to have a ΔRV of 37.5 km s^{-1} over ~ 1265 d, which is significantly below the threshold of 50 km s^{-1} , and hence we classify it as a presumably single star.

WR 2: WR 2 is the only WN2 star in the Galaxy. It is classified as a visual binary in the

GCWR and [VDH01](#). The optical spectrum clearly shows absorption lines of a B star in it. With the help of optical spectroscopy, [Chené et al. \(2019\)](#) did not find any significant RV variations over a period of ~ 10 yr. Using direct imaging with assumptions on the stellar parameters, the authors showed that the contribution of the B star to the optical spectrum is smaller than expected by a factor of ten (5% instead of 50% for its distance and absolute magnitude) and is hence likely to be a background object. We measure a ΔRV of 36.9 km s^{-1} for WR 2 over ~ 1085 d and classify it as a single star.

WR 3: According to [VDH01](#), WR 3 is classified as a WN3 + O4 system. [Moffat et al. \(1986\)](#) found a period of 46.85 ± 0.02 d with a mean semi-amplitude of the RV curve, K , of 33 km s^{-1} , using both He II 4686 (emission) and H γ (absorption) lines. However, the RV curves of the absorption and the emission line were found to be roughly in phase (relative phase shift of 0.15 ± 0.03), implying that the absorption lines are intrinsic to the WR star. Given that the line profiles of WR 3 are fairly stable and triangular, [Marchenko et al. \(2004\)](#) hypothesised it to be a single WN3 star with a high hydrogen abundance and were able to model the optical spectrum. The GCWR classifies it as a WN3ha (hydrogen rich with absorption lines). In this work, we find WR 3 to have a ΔRV of 13.1 km s^{-1} over ~ 120 d measured using the N V line at 4945 \AA . We therefore reject the period found by [Moffat et al. \(1986\)](#) and classify it as a single star.

WR 6: The GCWR classifies WR 6 as a SB1? system. The system demonstrates spectacular photometric ([Marchenko et al. 1998b](#), and references therein) and spectral ([Morel et al. 1997; Flores et al. 2007](#)) variability with a period of 3.77 d. Additionally, this periodicity has been shown to vary on longer timescales ([Drissen et al. 1989; Robert et al. 1992](#)). The line-profile variability was thought to be caused by wind-wind collisions with a (compact) binary companion, but [Morel et al. \(1997\)](#) argued that this is rather due to a structured wind.

With uninterrupted photometry over 136 d from the BRITE satellite, [Schmutz & Koenigsberger \(2019\)](#) modelled the light curve and showed that the epoch-to-epoch variability was due to rapid apsidal motion in a binary. [Koenigsberger & Schmutz \(2020\)](#) used archival UV and X-ray data collected over several decades to model the emission peaks of various line profiles and also computed RVs. They were able to explain both the RVs and light curves with rapid apsidal motion in an eccentric binary (WR+B, $e=0.1$). Moreover, the authors also presented arguments for a third companion. In this work, we measure a ΔRV of 170.0 km s^{-1} over ~ 1025 d and classify WR 6 to be a binary system, in agreement with other findings.

WR 7: The GCWR classifies WR 7 as a single star. With Hipparcos photometry, [Marchenko et al. \(1998b\)](#) observed a long-term trend but did not find any periods. We find that WR 7 exhibits strong line-profile variability over short timescales, although we were unable to discern any conclusive periodicity. With observations over ~ 640 d,

we measure a ΔRV of 46.5 km s^{-1} and classify it as a single star. However, recent observations from TESS indicate the presence of two short periods, about 0.3 d and 2.6 d . A detailed analysis of these periods is in progress (Toalá et al. in accepted).

WR 10: In the GCWR, WR 10 is classified as a single WN5h star. It is a visual binary with an A2V star as a companion, but it lacks RV variation (Niemela et al. 1999), which we confirm. In this work, we find WR 10 to have a ΔRV of 10.2 km s^{-1} over $\sim 680 \text{ d}$, thus classifying it as a single star.

WR 110: WR 110 is classified as a single WN5b (broad-lined) star in the GCWR. Over a time span of $\sim 680 \text{ d}$, we do not find significant RV variations with a ΔRV of 31.8 km s^{-1} and classify it as a single star.

WR 127: According to the GCWR, WR 127 is a binary system with spectral type WN3b + O9.5V. A spectroscopic orbit was derived by Massey (1981) with a period of $9.5550 \pm 0.0002 \text{ d}$. Lamontagne et al. (1996) and Marchenko et al. (1998b) found shallow eclipses in the light curve over the same period. de La Chevrotière et al. (2011) improved the orbital solution, modelled the wind-wind collision zone, and revised the classification of the O-star, reclassifying WR 127 as a WN5o+O8.5V system. We find WR 127 to have a ΔRV of 332.0 km s^{-1} over $\sim 2650 \text{ d}$ and classify it as a binary system.

WR 128: According to the GCWR, WR 128 is classified as a WN4(h) star with a binary status of SB2?. It was found to be a photometric variable by Antokhin & Cherepashchuk (1985) with a period of 3.871 d in the V band. The depth of the eclipses led the authors to conclude that the companion was a neutron star with a bright accretion disk. Moffat & Shara (1986) could not verify this period in their study, and the nature of the companion has also not been confirmed yet. In this study, we find WR 128 to have a ΔRV of 9.7 km s^{-1} over $\sim 1120 \text{ d}$ and classify it as a single star.

WR 133: WR 133 is classified as a WN5o + O9I system. In addition to being a SB2 system, it also shows photometric (Marchenko et al. 1998b) and polarimetric (Robert et al. 1989) variability, although the photometric variability is not coherent with the binary orbit. The spectroscopic orbit was first derived by Underhill & Hill (1994). Richardson et al. (2021) combined interferometric and spectroscopic data to derive the first visual orbit for a WN star and also to improve upon the parameters of the system. In this study, we measure RVs for WR 133 with N v $\lambda 4945$. We find a ΔRV of 111.6 km s^{-1} over a timescale of $\sim 2900 \text{ d}$ and classify it as a binary system.

WR 138: According to the GCWR, WR 138 is classified as a WN5o + B? system. The companion was classified as an O9 star by Annuk (1990), who found a period of 1538 d . This was further confirmed and improved upon by Palate et al. (2013), who derived a period of $1521 \pm 35 \text{ d}$ with optical spectroscopy. They also found evidence of

wind-wind collision with X-ray observations. Finally, Richardson et al. (2016) were able to resolve the system with interferometry and, with spectroscopy, they classified the companion as an O9V star with a fairly high $v \sin i$ of $\sim 350 \text{ km s}^{-1}$. We measured the RVs with weak N v lines, particularly a combination of N v $\lambda\lambda 4604, 4620$, and N v $\lambda 4945$. Over a timescale of ~ 2900 d, we find WR 138 to have a ΔRV of 92.1 km s^{-1} and classify it as a binary system.

WR 139: Also known as V444 Cyg, WR 139 is an eclipsing short-period binary system with a spectral classification of WN5o + O6III-V with a period of 4.212435 d. It is a well-studied object both with photometry (Moffat & Shara 1986; Marchenko et al. 1998b, and references within) and spectroscopy (Marchenko et al. 1994). Marchenko et al. (1994) also found evidence of a stable, short-period signal ($P \sim 0.36$ d) from the He II $\lambda 4686$ and He II $\lambda 5412$ radial velocities that they attributed to pulsations. The RVs were measured with N v $\lambda 4945$. With a ΔRV of 618.3 km s^{-1} over ~ 2950 d, we classify WR 139 as a binary system.

WR 141: According to the GCWR, WR 141 is a SB2 binary system with a spectral type of WN5o + O5V-III and a period of 21.7 d. Orbital solutions were derived by both Marchenko et al. (1998a) and Ivanov et al. (1999), but we list the former in Table 4.2 as it is an SB2 solution and as both derived orbital parameters are consistent within errors. In this study, we find WR 141 to have a ΔRV of 209.8 km s^{-1} over ~ 2040 d and classify it as a binary system. The RVs were measured with N v $\lambda 4945$.

WR 151: WR 151 is another short-period eclipsing binary with a period of 2.12691 d that is classified as a WN4o + O5V system in the GCWR. Hutton et al. (2009) combined RV measurements from Lewis et al. (1993) and photometry to fit a simultaneous orbital solution. We measure RVs with N v $\lambda 4945$, find a ΔRV of 650 km s^{-1} over ~ 950 d and classify it as a binary.

WR 152: The GCWR classifies WR 152 as a WN3(h). We measure RVs using N v $\lambda 4945$ and find a ΔRV of 8.3 km s^{-1} over ~ 920 d, thus classifying it as a single star.

WR 157: According to the GCWR, WR 157 is a visual binary with a spectral type WN5o (+B1III). As part of a larger sample, Maíz Apellániz et al. (2021) observed the system with lucky spectroscopy and reclassified the companion as an SB2 (B0.7II + B1III) system. In this study, we measure RVs for the WR star with N v $\lambda\lambda 4604, 4620$ and note that it barely moves. We measure a ΔRV of 11.8 km s^{-1} over ~ 2170 d. However, He I $\lambda 4471$ shows an SB2 behaviour, implying that the system is a triple (Fig. B.1). He II $\lambda 4541$ also appears to show the same SB2 behaviour, although it is less certain due to the blend with the WR emission. We conclude that the system has a tight B + B binary and a WR star whose connection to the B-binary is yet to be

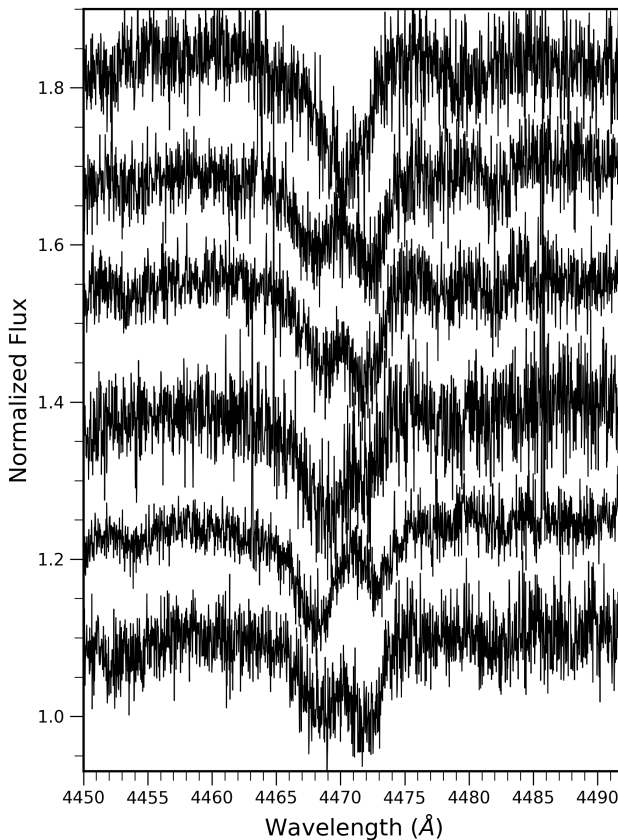


Figure B.1: $\text{He I } \lambda 4471$ line for WR 157. Six epochs of spectra are stacked with an arbitrary distance apart to demonstrate its SB3 nature.

established. This is similar to BAT99 126, the WR star in the Large Magellanic Cloud that was found to be a quadruple system ([Janssens et al. 2021](#)).

B.2 Relative RV measurements

Relative RVs for the objects in our sample. The reference epoch has a RV of 0.0 km s^{-1} . We refrain from providing absolute RV measurements as this is highly

method dependent, especially for WR stars. The Barycentric Julian Date (BJD) is given as the middle of the exposure. The average S/N is given in Table 4.1. Along with the measured RVs, we have indicated the measurement error, that is, the statistical uncertainty σ_p (Eq. 3.13).

Table B.1: Journal of HERMES observations for WR 1. Mask used: wings of the N v λ 4945

BJD – 2450000 (d)	Relative RV (km s ⁻¹)	σ_p (km s ⁻¹)
7966.6224	12.6	3.5
8090.5018	5.9	6.6
8102.3783	-2.5	3.9
8131.3316	0.0	2.5
8713.6443	8.6	3.1
8714.5128	7.4	2.6
8717.6878	-6.5	3.7
8774.6470	-3.1	4.7
8779.4524	-24.9	4.6
8789.5124	-18.2	6.7
8796.5305	-7.1	4.0
8817.3615	3.0	5.9
8826.5518	-6.6	5.1
8856.3320	-11.5	8.4
8860.3339	-14.5	4.4
8878.3833	-14.8	3.4
9081.6208	-6.3	3.9
9082.6225	7.1	3.7
9146.5251	-4.2	3.4
9152.4444	-8.3	4.4
9153.4682	-7.5	4.5
9154.4621	3.9	6.0
9155.5839	-4.4	6.3
9156.5588	-15.5	4.7
9170.4167	-11.1	5.4
9206.3990	-9.8	4.2
9230.3722	-7.8	6.2

Table B.2: Journal of HERMES observations for WR 2. Mask used: full spec.

BJD – 2450000 (d)	Relative RV (km s ⁻¹)	σ_p (km s ⁻¹)
8089.4747	13.7	1.4
8102.3978	-23.2	4.8
8131.3613	0.0	3.4
8739.6347	-16.1	4.3
8742.6421	-10.4	4.5
8744.6089	-13.6	4.9
8753.6487	-7.1	3.3
8774.6743	-8.9	3.5
8817.4228	-16.8	5.4
9081.6507	2.8	3.2
9089.6989	8.9	3.0
9146.5668	-1.2	3.4
9148.4564	-4.4	5.6
9170.4916	-15.0	4.2
9171.3888	-5.4	4.3
9172.3591	-2.3	4.7
9173.4578	-9.6	4.4
9174.3348	-0.4	3.6

Table B.3: Journal of HERMES observations for WR 3. Mask used: Nv λ 4945.

BJD – 2450000 (d)	Relative RV (km s ⁻¹)	σ_p (km s ⁻¹)
8786.6329	-3.4	0.9
8817.4783	0.6	1.1
8854.4345	0.0	0.9
8876.3900	0.1	1.0
8878.4478	1.5	1.1
8892.3619	1.1	1.5
8898.3471	-0.7	1.3
8906.3982	-3.5	1.1

B.3 Posterior plots from MC simulations

Here we present the three-dimensional likelihood plots for the Bayesian analysis of the WNE sample with the assumptions and setup as described in 4.5.2 while exploring values for the mass-ratio index (κ) of +1.0 (Fig. B.2) and -1.0 (Fig. B.3). The conclusions do not vary significantly as compared to a flat mass ratio ($\kappa = 0.0$, Fig. 4.7).

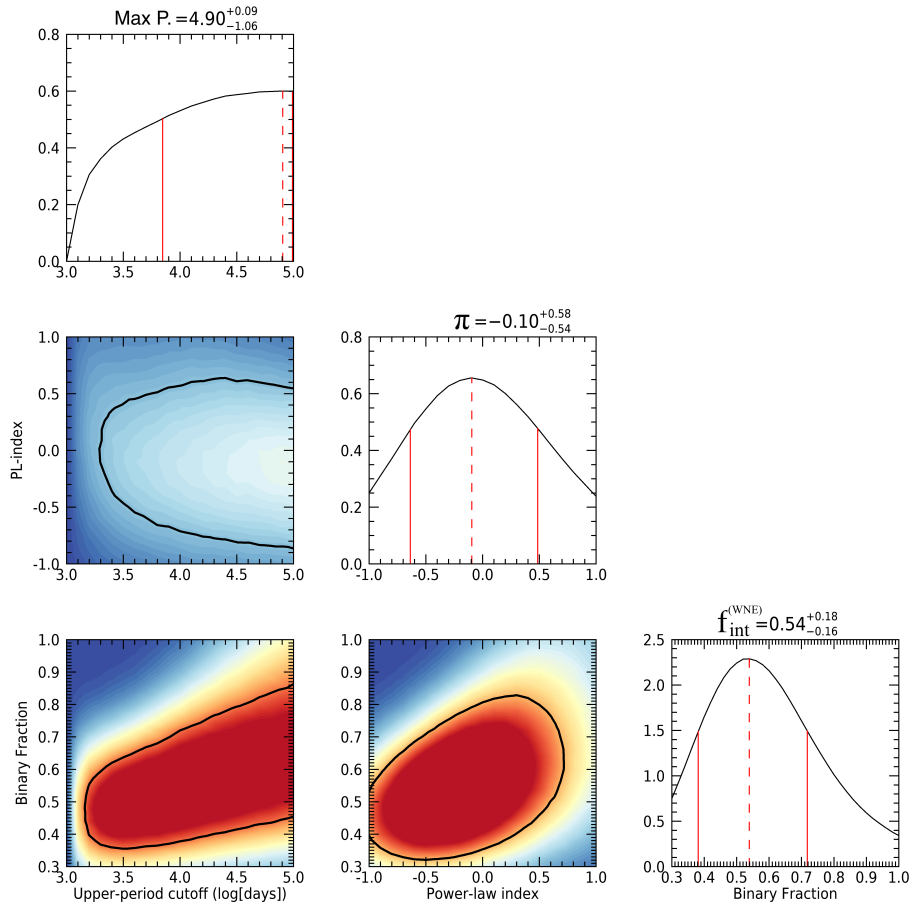


Figure B.2: Posteriors for $\log P_{\max}$, $f_{\text{int}}^{(\text{WNE})}$, and π for $\kappa = +1.0$. For each posterior, the solid red lines show HDI68, and the dashed red line shows the mode.

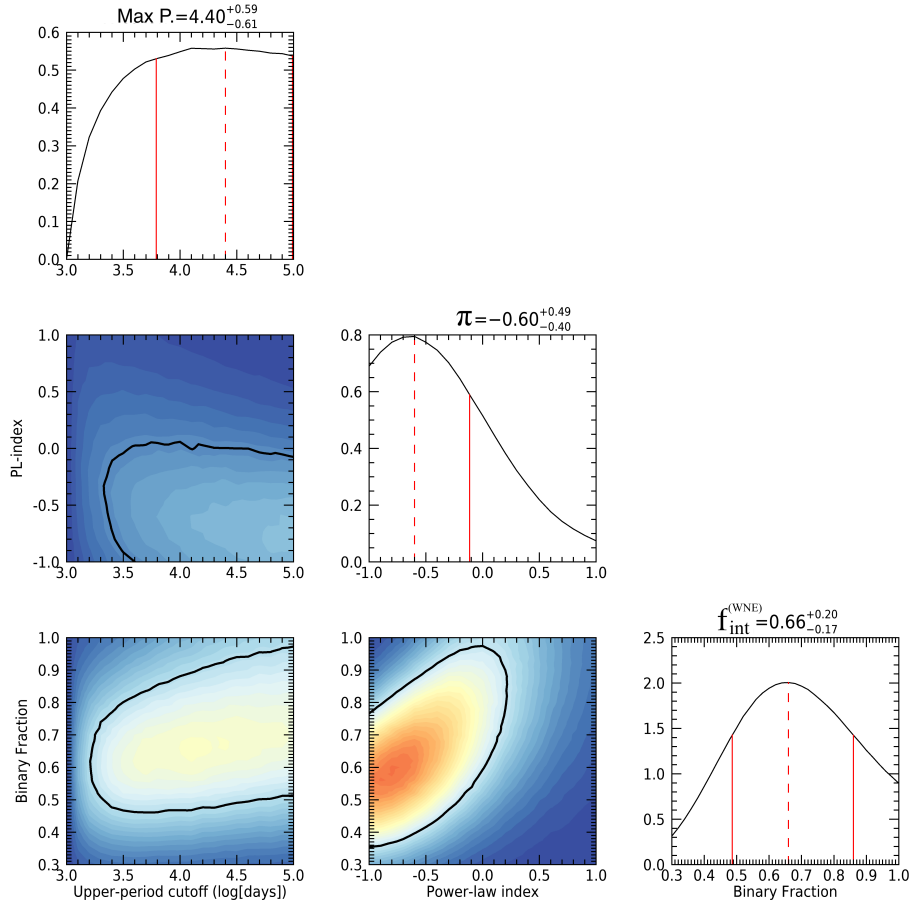


Figure B.3: Posteriors for $\log P_{\max}$, $f_{\text{int}}^{(\text{WNE})}$, and π for $\kappa = -1.0$. For each posterior, the solid red lines show HDI68, and the dashed red line shows the mode.

Table B.4: Journal of HERMES observations for WR 6. Mask used: full spec.

BJD – 2450000 (d)	Relative RV (km s ⁻¹)	σ_p (km s ⁻¹)
8131.5571	2.7	6.0
8139.5854	3.9	5.5
8165.4858	-7.9	10.3
8220.3593	-55.0	7.9
8227.3515	62.1	7.0
8796.7597	14.2	6.7
8799.7682	-106.0	6.4
8804.7649	0.0	5.4
8809.6896	-83.2	4.5
8818.6700	-107.9	3.7
8854.5539	-67.1	5.1
8859.5353	-98.4	4.4
8876.4221	-50.7	4.4
8876.4272	-60.1	4.0
8876.4324	-48.1	4.2
8876.5373	-55.3	4.0
8876.5425	-55.3	4.2
8876.5477	-48.8	4.1
8876.5529	-52.5	4.4
8876.5581	-52.9	4.8
8876.5634	-58.2	3.7
9147.7394	-6.6	7.0
9149.7643	-0.7	7.3
9150.7615	-57.9	6.6
9151.7686	-2.5	5.9
9152.7737	0.2	9.6
9155.7095	4.4	5.8
9156.7172	-11.3	6.7

B.3.1 WC sample

As discussed in Sect. 4.5.3, we performed MC simulations with a Bayesian framework for the 12 Galactic WC stars in Chapter 3 over four parameters, $\log P_{\min}$, $\log P_{\max}$, $f_{\text{int}}^{\text{WNE}}$, and π , with the same step size as for the WNE sample and over the ranges displayed in Fig. 4.8. We calculated the four-dimensional likelihood and corresponding posteriors, assuming flat priors. With this, we enable a consistent comparison of the corresponding WC and WNE populations from an evolutionary perspective.

As in Chapter 3, we divided the stars into four ΔRV bins: $5 \leq \Delta \text{RV} \leq 30 \text{ km s}^{-1}$ (six

Table B.5: Journal of HERMES observations for WR 7. Mask used: N v λ 4945.

BJD – 2450000 (d)	Relative RV (km s ⁻¹)	σ_p (km s ⁻¹)
8167.4273	–11.5	1.2
8183.3812	–10.4	1.2
8214.4138	0.0	1.1
8220.3859	–20.9	1.1
8225.3718	–18.4	1.3
8786.7478	–25.3	1.5
8809.7142	–46.5	1.9

Table B.6: Journal of HERMES observations for WR 10. Mask used: full spec.

BJD – 2450000 (d)	Relative RV (km s ⁻¹)	σ_p (km s ⁻¹)
8139.6049	2.7	0.6
8166.4471	0.0	0.7
8188.4025	–0.7	0.7
8223.3767	3.4	0.8
8226.3695	–4.5	0.6
8817.7041	5.7	0.8

Table B.7: Journal of HERMES observations for WR 110. Mask used: full spec.

BJD – 2450000 (d)	Relative RV (km s ⁻¹)	σ_p (km s ⁻¹)
7880.6775	–2.4	2.1
7904.6723	1.9	2.3
7907.6736	–9.4	2.8
8227.7273	–14.1	3.1
8249.6929	–20.3	2.2
8255.6409	4.7	2.8
8662.5573	0.0	2.8
8717.4911	–27.1	5.9
8721.4891	–19.1	4.3
9002.6274	4.1	3.4
9022.5824	–13.7	2.5

targets), $30 \leq \Delta\text{RV} \leq 250 \text{ km s}^{-1}$ (no observations), $250 < \Delta\text{RV} \leq 300 \text{ km s}^{-1}$ (one observation), and $\Delta\text{RV} \geq 300 \text{ km s}^{-1}$ (no observations). We also enforced that our simulations have binaries in the following period bins: $P > 20 \text{ d}$ (three systems), $P > 2000 \text{ d}$ (two systems). With this setup, we simulated 10 000 sets of 12 WC stars for each bin in this four-dimensional parameter space, hence $\sim 7^9$ populations.

Table B.8: Journal of HERMES observations for WR 127. Mask used: N v λ 4945.

BJD – 2450000 (d)	Relative RV (km s ⁻¹)	σ_p (km s ⁻¹)
6383.7311	269.4	2.5
7925.6481	190.6	2.7
7958.5570	128.5	6.3
7965.6804	27.0	3.2
8262.6484	0.0	2.9
8317.6849	137.1	3.0
8624.6814	36.4	5.2
8669.6351	292.6	3.3
8677.4986	332.0	3.4
9001.5189	274.0	2.2
9029.5713	201.6	2.5

Table B.9: Journal of HERMES observations for WR 128. Mask used: N v weak.

BJD – 2450000 (d)	Relative RV (km s ⁻¹)	σ_p (km s ⁻¹)
7914.7009	-3.9	0.8
7949.6014	-5.4	1.3
7965.6303	-6.9	1.1
7965.6540	-2.6	1.1
8201.7115	-9.5	1.0
8678.6017	-9.7	1.4
8749.5071	0.0	1.1
8762.4726	-4.6	1.6
9009.6923	-4.1	0.8
9034.6393	-4.4	1.3

Table B.10: Journal of HERMES observations for WR 133. Mask used: N v λ 4945.

BJD – 2450000 (d)	Relative RV (km s ⁻¹)	σ_p (km s ⁻¹)
6118.7225	57.5	3.7
6118.7252	58.1	4.2
6118.7279	60.1	3.8
6488.7325	0.0	1.8
6889.5771	80.7	2.1
6890.5661	93.8	2.1
7896.6971	79.1	3.5
7902.6919	77.7	3.3
7914.7239	68.8	3.3
8184.7739	42.7	4.0
8206.6924	27.4	4.1
8262.6628	30.1	2.7
8308.6629	41.2	4.0
8310.7398	24.0	4.1
8608.7226	20.2	3.2
8626.7249	-17.8	2.8
8652.5782	20.2	2.6
8779.4212	59.0	4.7
8921.7629	80.9	6.3
8999.6873	48.6	4.0
9008.7106	44.7	3.1

Table B.11: Journal of HERMES observations for WR 138. Mask used: N v weak.

BJD – 2450000 (d)	Relative RV (km s^{-1})	σ_p (km s^{-1})
6126.4561	87.3	2.0
6126.4602	81.2	1.9
6126.4643	75.8	2.0
6890.5817	29.4	0.8
7902.7238	83.0	1.1
7938.6839	82.0	1.1
7966.6459	73.3	1.3
8199.7580	57.1	1.4
8209.7583	48.5	1.3
8265.6425	48.4	1.3
8309.6314	42.2	1.8
8629.7285	14.5	1.3
8705.5768	-3.1	1.7
8706.6016	5.1	1.2
8707.5636	6.0	1.7
8708.5046	-2.7	1.2
8709.4356	4.9	1.2
8710.5668	0.0	1.3
8712.5364	4.4	1.6
8713.5060	5.7	1.6
8714.4872	6.9	1.4
8715.4997	9.0	1.3
8716.4250	5.5	1.3
8716.5228	5.2	1.2
8716.6573	3.3	1.4
8717.5872	9.3	1.5
8718.4849	5.0	1.3
8719.4380	3.8	1.5
8720.4098	4.8	2.2
8721.5385	-4.9	1.5
8726.4055	10.4	1.2
8726.4439	1.0	1.5
8726.4945	5.3	1.3
8726.5372	4.2	1.3
8726.5798	7.5	1.4
8726.6220	7.4	1.3
8796.4390	7.7	1.6
8800.3992	2.3	2.2
9008.7211	41.9	1.2
9024.5965	37.9	1.2

Table B.12: Journal of HERMES observations for WR 139. Mask used: N v λ 4945.

BJD – 2450000 (d)	Relative RV (km s ⁻¹)	σ_p (km s ⁻¹)
6126.6048	–217.3	8.1
6126.6090	–232.2	9.0
6126.6131	–231.8	7.4
6889.3780	–80.4	1.4
6889.5173	–38.7	1.4
6889.6903	29.5	3.0
6890.3932	274.2	1.3
6890.5345	280.2	1.2
6890.6132	275.1	2.8
6892.4109	–290.3	4.3
6892.5832	–338.1	5.7
6892.6850	–285.8	6.1
6894.3711	212.3	1.3
6894.5183	261.5	1.0
6894.6484	259.0	1.2
6896.4061	–236.0	3.2
6896.5401	–247.7	6.9
6896.6318	–274.3	5.3
6931.5018	–100.1	2.2
6946.3462	0.0	2.1
6946.4447	–64.2	2.8
7915.7128	–227.3	6.0
7919.7200	–130.5	3.8
7938.6750	78.2	1.9
8199.7629	21.2	2.7
8267.5991	192.4	2.7
8277.7066	–95.6	3.0
8277.7119	–91.1	3.6
8663.7305	247.9	1.9
8682.5103	–243.0	5.7
8741.4968	–250.7	5.2
8779.4428	–281.8	11.3
9024.6078	–255.7	8.2
9080.5344	167.5	2.2

Table B.13: Journal of HERMES observations for WR 141. Mask used: N v λ 4945.

BJD – 2450000 (d)	Relative RV (km s ⁻¹)	σ_p (km s ⁻¹)
6889.6476	74.8	5.1
6889.6690	47.7	7.9
7949.5642	-11.9	4.8
7957.6105	126.0	4.3
7961.6127	59.2	4.6
8196.7557	188.7	3.0
8267.6131	0.0	2.7
8332.7166	14.9	2.9
8666.7123	46.6	3.4
8749.5352	-15.0	3.0
8759.4257	152.6	4.4
8799.4244	136.5	7.4
9021.7199	146.7	6.8
9029.7067	-21.1	6.9

Table B.14: Journal of HERMES observations for WR 151. Mask used: N v λ 4945.

BJD – 2450000 (d)	Relative RV (km s ⁻¹)	σ_p (km s ⁻¹)
8133.3587	0.0	9.5
8718.5857	124.8	19.3
8763.4920	351.8	31.2
9042.5982	650.0	41.3
9051.6960	277.9	15.9
9057.6630	622.4	34.0

Table B.15: Journal of HERMES observations for WR 152. Mask used: N v λ 4945.

BJD – 2450000 (d)	Relative RV (km s ⁻¹)	σ_p (km s ⁻¹)
8137.3704	0.0	1.2
8712.5811	4.7	1.5
8753.5905	-0.0	1.6
8775.5911	-3.0	1.5
8791.4069	-2.0	1.3
9052.7004	-3.6	1.7
9058.6666	-0.6	1.5

Table B.16: Journal of HERMES observations for WR 157. Mask used: Nv $\lambda\lambda$ 4604, 4620.

BJD – 2450000 (d)	Relative RV (km s ⁻¹)	σ_p (km s ⁻¹)
6890.6373	–1.3	1.5
6890.6588	–1.9	1.4
8091.4134	0.0	1.1
8321.7169	–3.3	1.8
8336.6816	–8.1	1.4
8665.6904	–6.4	1.6
8754.5808	–8.7	1.6
8762.5811	–4.2	1.4
8775.4222	0.1	1.3
8787.4261	3.1	2.6
9041.7175	–0.1	1.2
9058.7028	–1.1	1.6

Appendix C

Appendix for Chapter 5

C.1 Comments on individual objects

WR 108: According to the GCWR, the spectra of WR 108 suffers from a dilution of emission lines, as well as absorption present in the spectrum. While it is quite common for WNL stars to show absorption, the dilution of emission lines is often attributed to a companion star. We measured a ΔRV of $\sim 16 \text{ km s}^{-1}$ over 1140 days, and classified WR 108 as a single star.

WR 120: The GCWR classifies WR 120 as a single WN7 star. The few absorption lines in the spectra exhibit moderate line-profile variability. However, the S/N of the data in the extreme blue regions makes it challenging to identify if this is simply due to intrinsic variability or due to Doppler motion. With 7 epochs spanning 385 days, we find a ΔRV of 40.5 km s^{-1} using N III, and classified it as a single star.

WR 123: WR 123 is notorious for its strong photometric and spectral line-profile variability (Marchenko & Moffat 1998). It was found to have a periodicity of ~ 10 hours using photometric and spectroscopic monitoring (Lefèvre et al. 2005; Dorfi et al. 2006; Chené et al. 2011). Similar to WR 120, we find the absorption lines in the spectra to vary quite significantly. By monitoring N V $\lambda\lambda 4604, 4620$ for eight epochs over 387 days, we measured a ΔRV of 57.1 km s^{-1} and classified it as a binary system. The sampling and number of spectra are too sparse to find any significant periodicity, and so further monitoring is required to verify its binary status.

WR 124: The GCWR classifies WR 124 as a SB1? with no dilution of emission lines. It is surrounded by a spectacular nebula M1-67 and is the fastest runaway in the Galaxy (Moffat et al. 1982). Given its 2.4 d and 2.7 d periodicity found (Moffat et al. 1982;

Moffat & Shara 1986), it was considered to be a binary with a neutron star. Toalá et al. (2018) could not rule out the presence of an embedded neutron star when studying the system with X-rays. If this were the case, the RV amplitude of the WR star would be below our threshold. In any case, we measured ΔRV to be 19.3 km s^{-1} with 10 epochs over 577 days, and classified WR 124 as a single star.

WR 134: Similar to WR 123 and WR 124, WR 134 is classified as a SB1? with no dilution of emission lines. Its binary status has been widely debated in the literature, and the observed periodicity has been attributed to a low-mass companion (Marchenko & Moffat 1998; Rustamov & Cherepashchuk 2012). However, Aldoretta et al. (2016) demonstrated that large-scale structures in the wind, particularly in He II $\lambda 5412$, exist with a period of 2.255 ± 0.008 d. We obtained 15 epochs over 2901 days and measured ΔRV to be 29.6 km s^{-1} using N V $\lambda 4945$ and classified it as a single star.

WR 136: WR 136 is surrounded by a ring nebula (NGC 6888), and is classified as a SB1? with no dilution of emission lines in the GCWR. A period of 4.554 d was found using line-profile variations (Koenigsberger et al. 1980) and RV measurements (Aslanov & Cherepashchuk 1981). However, this period was not verified later with polarisation (Robert & Moffat 1989) and photometry (Moffat & Shara 1986). A neutron star companion was suggested as a companion, which would again result in small RV variations of the WR star. With 39 epochs over a time baseline of 2907 days, we measured a ΔRV of 15.4 km s^{-1} using He II lines and classified it as a single star.

WR 148: WR 148 is one of the few WN8 stars in the Galaxy that is confirmed to be in a binary system. The GCWR classifies it as a SB1 system, as it has a short period of 4.3 d and was thought to have a compact companion (Drissen et al. 1986a; Bracher 1979; Marchenko et al. 1996). However, Munoz et al. (2017) found a period of 4.317336 ± 0.000026 and were able to disentangle the spectra to find a O4-6 companion. Hamann et al. (2019) found a luminosity ($\log L(L_\odot)$) of 6.2, indicating its potential to be a main-sequence star. However, they also reported that 15% of the flux is contributed by its companion, so further analysis taking this into account is required. We obtained 20 epochs over 1161 days and measured RVs using N IV $\lambda\lambda 7103, 7109, 7123$. We found WR 148 to have a ΔRV of 171.8 km s^{-1} and classified it as a binary system.

WR 153: The GCWR classifies WR 153 to be a quadruple system (WN6o/CE+O3-6 + B0:I+B1:V-III) where the WR binary has a period of 6.6887 days and a circular orbit (Massey 1981; Demers et al. 2002). With 49 epochs over 2858 days, we measured a ΔRV of 576.6 km s^{-1} using N V $\lambda\lambda 4604, 4620$ and classified it as a binary system.

WR 155: The GCWR classifies WR 155 as a SB2 (WN6o + O9II-Ib) system. It is a binary with the shortest known period (1.6412436 d, Moffat & Shara 1986; Marchenko et al. 1995). Drissen et al. (1986b) studied the system with polarimetry and found masses of 42 and $30 M_\odot$ for the WN and O stars respectively. We obtained 85 epochs over 3075 days, measured ΔRV to be 609.5 km s^{-1} using N V $\lambda 4945$ and $\lambda 4058$ and

classified it as a binary system.

WR 156: WR 156 is another WN8 star with large photometric and spectral line-profile variability, with its emission lines diluted. Photometric studies have not found any conclusive periodicity ([Moffat & Shara 1986](#); [Marchenko et al. 1998](#)). It is reported to have a luminosity of 6.01 ([Hamann et al. 2019](#)), which questions its status as a massive WNL versus a classical WNL star. We observed WR 156 over 797 days and obtained 18 epochs. Using N IV $\lambda\lambda 7103, 7109, 7123$ and $\lambda 5737$ lines, we measured a ΔRV of 16.1 km s^{-1} and classified it as a single star.

WR 158: The GCWR classifies WR 158 as a WN7h star with its emission lines diluted. [Andrillat & Vreux \(1992\)](#) discovered the presence of O I $\lambda 8446$ in its spectrum, hypothesising it being produced in the slowly expanding cool shocked region located outside the ionisation front of the bubble created by the WR wind, or in a binary with a Be companion. [Hamann et al. \(2019\)](#) reported a luminosity ($\log L(L_\odot)$) of 6.06, which could potentially indicate its status as a main-sequence WNL star. We obtained 13 spectra over 1031 days, measured a ΔRV of 15.0 km s^{-1} using N IV $\lambda\lambda 7103, 7109, 7123$ and classified it as a single star.

C.2 Relative radial velocity measurements

Relative RVs for the 11 WNLs in our sample. The reference epoch has a RV of 0.0 km s^{-1} . We refrain from providing absolute RV measurements as this is highly method dependent, especially for WR stars. The Barycentric Julian Date (BJD) is given as the middle of the exposure. The average S/N is given in Table 5.1. Along with the measured RVs, we have indicated the measurement error, that is, the statistical uncertainty σ_p (Eq. 3.9).

Table C.1: Journal of HERMES observations for WR 108. Mask used: N III $\lambda\lambda$ 4634, 4641 and $\lambda\lambda$ 5321, 5327

BJD – 2450000 (d)	Relative RV (km s ⁻¹)	σ_p (km s ⁻¹)
7880.6447	6.7	0.4
7908.5761	-8.6	0.4
7910.5874	-8.8	0.9
8226.7346	0.0	0.3
8249.6662	-1.9	0.3
8255.6139	-3.8	0.3
8647.6343	-8.0	0.4
8651.5446	-4.2	0.5
8671.5345	-9.0	0.4
9002.5960	2.1	0.6
9020.6068	-3.3	0.4

Table C.2: Journal of HERMES observations for WR 120. Mask used: N III $\lambda\lambda$ 4634, 4641

BJD – 2450000 (d)	Relative RV (km s ⁻¹)	σ_p (km s ⁻¹)
9000.5647	8.2	1.4
9000.5754	9.7	1.8
9029.5217	0.0	1.3
9343.5826	-9.1	2.1
9352.6879	-30.8	3.3
9364.6366	2.2	1.6
9385.6108	-21.1	1.3

Table C.3: Journal of HERMES observations for WR 123. Mask used: N V $\lambda\lambda$ 4604, 4620.

BJD – 2450000 (d)	Relative RV (km s ⁻¹)	σ_p (km s ⁻¹)
9009.6572	-41.2	4.7
9041.4644	-5.2	6.3
9078.5129	0.0	4.9
9150.3408	15.9	9.0
9341.6353	-27.3	7.1
9370.6808	-20.5	7.7
9382.6264	-13.3	5.4
9396.5899	-34.3	4.8

Table C.4: Journal of HERMES observations for WR 124. Mask used: N IV $\lambda\lambda 7103, 7109, 7123$.

BJD – 2450000 (d)	Relative RV (km s ⁻¹)	σ_p (km s ⁻¹)
8779.3312	2.9	4.3
8909.7390	–6.1	2.5
9007.5659	0.0	1.5
9024.4541	7.3	1.3
9341.7066	1.4	2.0
9342.6831	12.2	1.5
9345.5820	11.4	1.7
9346.6531	4.1	1.6
9355.6618	13.2	1.9
9356.6234	1.0	1.5

Table C.5: Journal of HERMES observations for WR 134. Mask used: N v $\lambda 4945$.

BJD – 2450000 (d)	Relative RV (km s ⁻¹)	σ_p (km s ⁻¹)
6119.7082	–17.4	1.6
6889.4453	8.5	1.0
7902.7067	–16.2	1.8
7919.7115	–6.3	2.6
7938.7064	–16.6	1.8
8195.7332	11.5	2.4
8206.6993	–18.1	2.1
8262.7226	–9.9	2.0
8276.6976	0.0	1.5
8625.7223	–3.2	1.9
8652.6205	–15.6	2.0
8663.7183	–7.0	2.1
8779.4245	3.8	2.8
9008.7157	3.2	2.3
9020.7094	–8.6	2.0

Table C.6: Journal of HERMES observations for WR 136. Mask used: He II λ 4201, λ 4542, λ 4687, λ 5412, λ 6312 and λ 6685.

BJD – 2450000 (d)	Relative RV (km s ⁻¹)	σ_p (km s ⁻¹)
6113.4883	-2.9	0.6
7899.7208	-3.2	0.6
7915.7252	-4.7	0.8
7919.6966	-2.4	1.2
7988.5162	-2.3	0.5
8195.7629	1.2	0.8
8206.7539	2.4	0.8
8262.6675	-2.7	0.5
8276.7222	0.1	0.6
8308.5859	-6.8	0.6
8608.7275	5.6	0.6
8652.6254	2.1	0.5
8680.5815	0.8	0.5
8700.6889	3.2	0.4
8705.5711	-0.4	0.4
8706.5963	1.0	0.4
8707.5559	4.7	0.5
8708.4991	4.7	0.4
8709.4306	-2.9	0.4
8710.5613	-2.2	0.4
8712.5417	-3.3	0.4
8713.5110	-1.9	0.5
8714.4924	-1.1	0.4
8715.5051	0.2	0.5
8716.5422	-9.9	0.3
8717.5973	-0.5	1.1
8718.4901	-2.0	0.4
8719.4433	-0.2	0.4
8720.4152	0.9	0.5
8721.5437	-3.9	0.5
8729.5184	2.0	0.3
8766.4506	1.3	0.2
8767.4729	1.0	0.3
8771.3722	1.4	0.2
8772.4400	2.7	0.2
8773.3992	0.0	0.3
8779.4334	-0.7	0.5
9009.5365	1.2	0.5
9020.6861	-2.0	0.6

Table C.7: Journal of HERMES observations for WR 148. Mask used: N_{IV}
 $\lambda\lambda\lambda$ 7103, 7109, 7123 and λ 4058.

BJD – 2450000 (d)	Relative RV (km s ⁻¹)	σ_p (km s ⁻¹)
7912.6900	51.0	1.2
7934.7125	-22.9	1.3
7952.6962	-74.7	1.0
8203.7536	-60.6	0.7
8262.6954	0.0	0.6
8332.6787	-80.9	0.6
8684.5886	90.9	0.8
8757.4993	65.7	0.8
8775.4903	87.1	1.0
8776.4943	12.7	1.2
8778.4304	4.2	3.7
8779.3554	89.3	4.8
8780.4683	52.8	1.5
8781.3212	-51.7	1.4
8791.3731	5.0	1.6
8792.3957	82.5	1.7
8796.4216	73.3	1.2
8798.3922	-46.3	1.9
9029.6207	63.2	1.3
9073.5716	59.8	1.1

Table C.8: Journal of HERMES observations for WR 153. Mask used: Nv $\lambda\lambda$ 4604, 4620.

BJD – 2450000 (d)	Relative RV (km s ⁻¹)	σ_p (km s ⁻¹)
6305.3277	-11.8	3.0
6889.5378	41.7	3.2
6889.5592	27.0	3.7
6889.7109	-19.2	3.8
6889.7324	0.0	5.0
6890.4169	-151.0	4.1
6890.4383	-152.5	4.5
6890.6822	-223.8	3.3
6890.7036	-211.2	4.1
6892.4550	-336.0	2.9
6892.4764	-372.0	2.9
6892.7059	-293.0	2.2
6892.7273	-291.0	3.0
6894.3935	49.1	3.1
6894.4149	58.0	3.4
6894.5856	79.3	2.6
6894.6070	93.3	4.0
6896.4275	3.6	2.6
6896.4489	0.0	2.6
6896.6675	-71.7	5.7
6896.6855	-49.4	3.5
6903.4817	-64.8	3.0
6903.5031	-82.6	2.9
6903.6291	-123.0	3.1
6903.6505	-123.6	2.7
6946.3828	-278.5	2.3
6946.4121	-279.7	1.9
6946.5195	-233.3	3.4
6946.5435	-229.1	4.1
7952.7273	113.9	3.9
7958.7316	179.4	8.9
7963.6529	-101.2	5.5
8102.3196	-318.9	3.8
8198.7456	78.9	5.2
8267.7027	16.0	5.2
8310.6395	-287.8	3.7
8319.6697	151.2	4.4
8660.7183	130.3	4.1
8754.4247	130.2	3.2
8760.5219	27.5	3.6
8775.5577	72.1	2.6
8779.4643	-220.4	3.1
8796.4808	-122.2	3.9
8798.4221	-397.2	0.0
8799.4985	-238.5	2.7
8800.4418	11.9	6.5
8819.3970	-255.4	3.8

Table C.9: Continued for WR 153.

BJD – 2450000 (d)	Relative RV (km s^{-1})	σ_p (km s^{-1})
9080.5761	–185.6	1.9
9146.3619	–321.9	3.3
9147.4905	–160.5	4.9
9148.3736	28.2	3.5
9151.4101	–202.9	2.3
9152.3290	–320.1	1.6
9153.4017	–312.2	3.1
9154.4319	–97.8	3.4
9155.5509	79.1	5.4
9156.5313	114.1	2.9
9157.3331	–10.4	3.7
9163.4296	74.1	21.3

Table C.10: Journal of HERMES observations for WR 155. Mask used: N v λ 4945 and λ 4058.

BJD – 2450000 (d)	Relative RV (km s ⁻¹)	σ_p (km s ⁻¹)
6132.6769	316.0	0.9
6134.5244	324.1	0.9
6135.6394	-14.1	0.9
6209.4378	-89.5	0.9
6210.3816	60.3	1.0
6210.4044	24.5	1.1
6210.5143	-118.3	1.0
6210.5288	-133.4	0.9
6211.4146	290.0	0.7
6212.4061	-247.2	0.9
6213.5000	253.7	1.1
6214.4316	0.0	1.0
6215.5349	-203.8	0.6
7948.6674	-197.8	0.8
7956.6991	-23.8	1.2
7962.7296	354.7	1.2
8091.4423	-194.7	1.5
8102.3489	342.7	1.2
8132.3478	-85.3	1.3
8335.5487	278.6	1.8
8336.6230	98.9	1.7
8668.7252	267.6	1.3
8721.6561	-171.8	1.2
8733.5426	-160.8	1.6
8775.3155	298.6	1.1
8775.6162	48.7	1.6
8776.5293	159.5	0.8
8776.5871	217.1	0.8
8778.4172	335.2	1.6
8778.5538	314.4	1.3
8779.3193	-235.6	3.7
8779.4735	-188.6	2.9
8794.3532	-102.8	5.0
8794.3736	-77.8	2.7
8796.3591	287.6	1.0
8796.4956	333.0	1.3
8800.3673	-105.3	1.2
8819.3904	331.3	1.2
8819.4572	350.2	1.4
8820.3269	-239.6	1.4
8858.3542	-100.5	1.6
8859.3150	82.0	1.8
9009.7119	288.0	1.1
9041.5810	-61.4	2.2
9042.5025	259.4	1.5
9042.6246	334.2	1.2
9044.6499	206.8	1.1

Table C.11: Continued for WR 155.

BJD – 2450000 (d)	Relative RV (km s ⁻¹)	σ_p (km s ⁻¹)
9089.6076	–211.0	4.3
9089.6304	–200.2	1.2
9098.5925	323.5	1.3
9098.7359	263.4	1.3
9099.5498	–154.5	2.8
9146.3472	246.8	1.7
9146.5890	–30.0	2.2
9147.4761	187.5	1.3
9147.5661	277.5	1.6
9148.3213	–139.8	3.2
9148.5401	–254.9	4.1
9152.3438	136.5	1.3
9152.5696	338.3	1.8
9153.4166	–244.0	3.3
9153.5375	270.5	12.1
9154.4476	306.5	1.9
9155.3228	–186.9	2.4
9155.5357	11.6	1.4
9157.3185	195.3	1.2
9157.3482	221.8	1.1
9160.4016	–34.4	1.0
9162.3752	311.7	1.1
9196.4044	–148.5	2.4
9206.3166	–56.8	2.1
9206.4406	61.1	1.7
9207.3304	–42.3	2.1
9207.4586	–172.5	11.4

Table C.12: Journal of HERMES observations for WR 156. Mask used: N_{IV}
 $\lambda\lambda\lambda7103, 7109, 7123$ and $\lambda5737$.

BJD – 2450000 (d)	Relative RV (km s ⁻¹)	σ_p (km s ⁻¹)
8336.6487	5.4	1.2
8754.4051	-2.9	1.1
8761.5931	0.0	1.1
8775.4585	-3.5	1.0
8786.4646	-9.7	1.2
8798.5261	-6.0	1.7
8798.5368	-4.7	2.1
8821.3559	-6.3	1.2
8826.4376	-8.9	1.2
9073.6574	0.3	1.0
9079.6211	-6.5	1.0
9081.5919	-0.2	1.0
9106.6019	-3.9	1.2
9120.5904	-2.5	1.3
9124.4972	-8.8	1.2
9127.5059	-8.6	1.3
9132.5919	6.4	1.1
9133.5744	-2.8	1.1

Table C.13: Journal of HERMES observations for WR 158. Mask used: N_{IV}
 $\lambda\lambda\lambda7103, 7109, 7123$.

BJD – 2450000 (d)	Relative RV (km s ⁻¹)	σ_p (km s ⁻¹)
8091.4727	-2.7	0.4
8336.7140	3.1	0.4
8736.6307	-1.9	0.4
8737.5247	0.0	0.3
8775.3857	-1.0	0.4
8798.4824	-3.5	0.5
8821.4275	-2.2	0.3
8875.3741	6.5	0.4
9075.6776	-4.5	0.4
9089.6552	-8.5	0.5
9097.6090	3.6	0.6
9106.6458	0.6	0.5
9122.4711	4.6	0.4

Bibliography

- Aldroretta, E. J., St-Louis, N., Richardson, N. D., et al. 2016, Monthly Notices of the Royal Astronomical Society, 460, 3407, aDS Bibcode: 2016MNRAS.460.3407A
- Almeida, L. A., Sana, H., Taylor, W., et al. 2017, Astronomy & Astrophysics, Volume 598, id.A84, 36 pp., 598, A84
- Andrillat, Y. & Vreux, J.-M. 1992, Astronomy and Astrophysics, Vol. 253, p. L37-L39 (1992), 253, L37
- Annuk, K. 1990, ACTA, 40, 267
- Antokhin, I. I. & Cherepashchuk, A. M. 1985, Soviet Astronomy Letters, 11, 355
- Arora, B., Pandey, J. C., De Becker, M., et al. 2021, AJ, 162, 257
- Aslanov, A. A. & Cherepashchuk, A. M. 1981, Soviet Astronomy Letters, 7, 265, aDS Bibcode: 1981SvAL....7..265A
- Balona, L. A., Egan, J., & Marang, F. 1989, Monthly Notices of the Royal Astronomical Society, 240, 103, aDS Bibcode: 1989MNRAS.240..103B
- Banyard, G., Sana, H., Mahy, L., et al. 2022, Astronomy & Astrophysics, Volume 658, id.A69, 28 pp., 658, A69
- Barbá, R., Gamen, R., Arias, J. I., et al. 2014, 44, 148, conference Name: Revista Mexicana de Astronomia y Astrofisica Conference Series ADS Bibcode: 2014RMxAC..44Q.148B
- Bartzakos, P., Moffat, A. F. J., & Niemela, V. S. 2001, Monthly Notices of the Royal Astronomical Society, 324, 18, aDS Bibcode: 2001MNRAS.324...18B
- Bisiacchi, G. F., Firmani, C., & de Lara, E. 1983, RMxAA, 5, 285
- Bracher, K. 1979, Publications of the Astronomical Society of the Pacific, 91, 827, aDS Bibcode: 1979PASP..91..827B

- Bromm, V. & Larson, R. B. 2004, Annual Review of Astronomy & Astrophysics, vol. 42, Issue 1, pp.79-118, 42, 79
- Brown, J. C., Richardson, L. L., Antokhin, I., et al. 1995, A&A, 295, 725
- Castor, J. I., Abbott, D. C., & Klein, R. I. 1975, ApJ, 195, 157
- Chené, A. N. & St-Louis, N. 2010, ApJ, 716, 929
- Chené, A. N. & St-Louis, N. 2011, ApJ, 736, 140
- Chené, A. N. & St-Louis, N. 2011, The Astrophysical Journal, 736, 140, aDS Bibcode: 2011ApJ...736..140C
- Chené, A.-N., St-Louis, N., Moffat, A. F. J., & Gayley, K. G. 2020, The Astrophysical Journal, 903, 113, aDS Bibcode: 2020ApJ...903..113C
- Chené, A.-N., St-Louis, N., Moffat, A. F. J., & Gayley, K. G. 2020, ApJ, 903, 113
- Chené, A. N., St-Louis, N., Moffat, A. F. J., et al. 2019, MNRAS, 484, 5834
- Chené, A.-N., Foellmi, C., Marchenko, S. V., et al. 2011, Astronomy & Astrophysics, Volume 530, id.A151, 6 pp., 530, A151
- Clark, J. S., Negueruela, I., Crowther, P. A., & Goodwin, S. P. 2005, A&A, 434, 949
- Conti, P. 1976, in Proc. 20th Colloq. Int. Astrophys., Univ. Liege, 193
- Conti, P. S. & Massey, P. 1989, ApJ, 337, 251
- Crowther, P. A. 2007, Annual Review of Astronomy & Astrophysics, vol. 45, Issue 1, pp.177-219, 45, 177
- Crowther, P. A. 2007, ARA&A, 45, 177
- Crowther, P. A., Smith, L. J., Hillier, D. J., & Schmutz, W. 1995, A&A, 293, 427
- David-Uraz, A., Moffat, A. F. J., Chené, A.-N., et al. 2012, MNRAS, 426, 1720
- David-Uraz, A., Moffat, A. F. J., Chené, A.-N., et al. 2012, Monthly Notices of the Royal Astronomical Society, 426, 1720, aDS Bibcode: 2012MNRAS.426.1720D
- Davies, B., Crowther, P. A., & Beasor, E. R. 2018, Monthly Notices of the Royal Astronomical Society, 478, 3138, aDS Bibcode: 2018MNRAS.478.3138D
- de Jager, C., Nieuwenhuijzen, H., & van der Hucht, K. A. 1988, A&AS, 72, 259
- de Koter, A., Heap, S. R., & Hubeny, I. 1997, ApJ, 477, 792
- de La Chevrotière, A., Moffat, A. F. J., & Chené, A. N. 2011, MNRAS, 411, 635

- de Mink, S. E., Langer, N., Izzard, R. G., Sana, H., & de Koter, A. 2013, ApJ, 764, 166
- de Mink, S. E., Sana, H., Langer, N., Izzard, R. G., & Schneider, F. R. N. 2014, ApJ, 782, 7
- Demers, H., Moffat, A. F. J., Marchenko, S. V., Gayley, K. G., & Morel, T. 2002, The Astrophysical Journal, 577, 409, aDS Bibcode: 2002ApJ...577..409D
- Desforges, S., St-Louis, N., Chené, A. N., de la Chevrotière, A., & Hénault-Brunet, V. 2017, MNRAS, 465, 1227
- Dessart, L. & Owocki, S. P. 2005, A&A, 437, 657
- Dorfi, E. A., Gautschy, A., & Saio, H. 2006, Astronomy and Astrophysics, Volume 453, Issue 3, July III 2006, pp.L35-L37, 453, L35
- Dougherty, S. M., Williams, P. M., & Pollacco, D. L. 2000, MNRAS, 316, 143
- Dougherty, S. M., Williams, P. M., van der Hucht, K. A., Bode, M. F., & Davis, R. J. 1996, MNRAS, 280, 963
- Driessen, F. A., Sundqvist, J. O., & Kee, N. D. 2019, A&A, 631, A172
- Drissen, L., Lamontagne, R., Moffat, A. F. J., Bastien, P., & Seguin, M. 1986a, The Astrophysical Journal, 304, 188, aDS Bibcode: 1986ApJ...304..188D
- Drissen, L., Moffat, A. F. J., Bastien, P., Lamontagne, R., & Tapia, S. 1986b, The Astrophysical Journal, 306, 215, aDS Bibcode: 1986ApJ...306..215D
- Drissen, L., Robert, C., Lamontagne, R., et al. 1989, ApJ, 343, 426
- Dunstall, P. R., Dufton, P. L., Sana, H., et al. 2015, Astronomy & Astrophysics, Volume 580, id.A93, 10 pp., 580, A93
- Ekström, S., Georgy, C., Eggenberger, P., et al. 2012, A&A, 537, A146
- Fabry, M., Hawcroft, C., Mahy, L., et al. 2021, spinOS: SPectroscopic and INterferometric Orbital Solution finder, Astrophysics Source Code Library, record ascl:2102.001
- Fahed, R., Moffat, A. F. J., & Bonanos, A. Z. 2009, MNRAS, 392, 376
- Fahed, R., Moffat, A. F. J., Zorec, J., et al. 2011, Monthly Notices of the Royal Astronomical Society, 418, 2, aDS Bibcode: 2011MNRAS.418....2F
- Fahed, R., Moffat, A. F. J., Zorec, J., et al. 2011, MNRAS, 418, 2
- Faherty, J. K., Shara, M. M., Zurek, D., Kanarek, G., & Moffat, A. F. J. 2014, The Astronomical Journal, 147, 115, aDS Bibcode: 2014AJ....147..115F

- Fitzpatrick, E. L. 2004a, 309, 33, conference Name: Astrophysics of Dust Place: eprint: arXiv:astro-ph/0401344 ADS Bibcode: 2004ASPC..309...33F
- Fitzpatrick, E. L. 2004b, Astronomical Society of the Pacific Conference Series, Vol. 309, Interstellar Extinction in the Milky Way Galaxy, 33
- Flores, A., Koenigsberger, G., Cardona, O., & de la Cruz, L. 2007, AJ, 133, 2859
- Foellmi, C., Moffat, A. F. J., & Guerrero, M. A. 2003a, Monthly Notices of the Royal Astronomical Society, 338, 360, aDS Bibcode: 2003MNRAS.338..360F
- Foellmi, C., Moffat, A. F. J., & Guerrero, M. A. 2003b, Monthly Notices of the Royal Astronomical Society, 338, 1025, aDS Bibcode: 2003MNRAS.338.1025F
- Fryer, C. L., Mazzali, P. A., Prochaska, J., et al. 2007, Publications of the Astronomical Society of the Pacific, 119, 1211, aDS Bibcode: 2007PASP..119.1211F
- Fullerton, A. W., Massa, D. L., & Prinja, R. K. 2006, The Astrophysical Journal, 637, 1025, aDS Bibcode: 2006ApJ...637.1025F
- Gamow, G. 1943, The Astrophysical Journal, 98, 500, aDS Bibcode: 1943ApJ....98..500G
- Gilkis, A., Shenar, T., Ramachandran, V., et al. 2021, Monthly Notices of the Royal Astronomical Society, 503, 1884, aDS Bibcode: 2021MNRAS.503.1884G
- Gräfener, G. & Hamann, W. R. 2005, A&A, 432, 633
- Gräfener, G., Koesterke, L., & Hamann, W. R. 2002, A&A, 387, 244
- Grassitelli, L., Langer, N., Grin, N. J., et al. 2018, Astronomy & Astrophysics, Volume 614, id.A86, 17 pp., 614, A86
- Groh, J. H., Ekström, S., Georgy, C., et al. 2019, Astronomy & Astrophysics, Volume 627, id.A24, 19 pp., 627, A24
- Gräfener, G., Koesterke, L., & Hamann, W.-R. 2002, Astronomy and Astrophysics, v.387, p.244-257 (2002), 387, 244
- Gräfener, G., Owocki, S. P., & Vink, J. S. 2012, Astronomy & Astrophysics, Volume 538, id.A40, 14 pp., 538, A40
- Güdel, M. & Nazé, Y. 2009, A&A Rev., 17, 309
- Hainich, R., Pasemann, D., Todt, H., et al. 2015, Astronomy & Astrophysics, Volume 581, id.A21, 30 pp., 581, A21
- Hamann, W. R. & Gräfener, G. 2004, A&A, 427, 697

- Hamann, W.-R. & Gräfener, G. 2003, *Astronomy and Astrophysics*, v.410, p.993-1000 (2003), 410, 993
- Hamann, W.-R., Gräfener, G., Liermann, A., et al. 2019, *Astronomy & Astrophysics*, Volume 625, id.A57, 11 pp., 625, A57
- Hamann, W. R. & Koesterke, L. 1998, *A&A*, 335, 1003
- Heger, A., Fryer, C. L., Woosley, S. E., Langer, N., & Hartmann, D. H. 2003, *The Astrophysical Journal*, 591, 288, aDS Bibcode: 2003ApJ...591..288H
- Hilditch, R. W. 2001, *An Introduction to Close Binary Stars*
- Hill, G. M., Moffat, A. F. J., & St-Louis, N. 2018, *Monthly Notices of the Royal Astronomical Society*, 474, 2987, aDS Bibcode: 2018MNRAS.474.2987H
- Hill, G. M., Moffat, A. F. J., & St-Louis, N. 2018, *MNRAS*, 474, 2987
- Hillier, D. J. 1991, *A&A*, 247, 455
- Humphreys, R. M. & Davidson, K. 1979, *The Astrophysical Journal*, 232, 409, aDS Bibcode: 1979ApJ...232..409H
- Hut, P. 1981, *A&A*, 99, 126
- Hutton, K., Henden, A., & Terrell, D. 2009, *PASP*, 121, 708
- Ivanov, M. M., Valchev, T. S., Georgiev, L. N., Barba, R., & Iliev, I. K. 1999, *RMxAA*, 35, 25
- Ivanova, N., Justham, S., Chen, X., et al. 2013, *The Astronomy and Astrophysics Review*, Volume 21, article id.59, 21, 59
- Janssens, S., Shenar, T., Mahy, L., et al. 2021, *A&A*, 646, A33
- Janssens, S., Shenar, T., Sana, H., et al. 2022, *A&A*, 658, A129
- Jones, D., Boffin, H. M. J., Rodríguez-Gil, P., et al. 2015, *A&A*, 580, A19
- Kausch, W., Noll, S., Smette, A., et al. 2015, *Astronomy & Astrophysics*, Volume 576, id.A78, 17 pp., 576, A78
- Klencki, J., Nelemans, G., Istrate, A. G., & Chruslinska, M. 2021, *Astronomy & Astrophysics*, Volume 645, id.A54, 27 pp., 645, A54
- Kobulnicky, H. A., Kiminki, D. C., Lundquist, M. J., et al. 2014, *The Astrophysical Journal Supplement Series*, 213, 34, aDS Bibcode: 2014ApJS..213...34K
- Koenigsberger, G., Firmani, C., & Bisiacchi, G. F. 1980, *Revista Mexicana de Astronomia y Astrofisica*, 5, 45, aDS Bibcode: 1980RMxAA...5...45K

- Koenigsberger, G. & Schmutz, W. 2020, A&A, 639, A18
- Lamers, H. J. G. L. M. & Levesque, E. M. 2017, Understanding Stellar Evolution
- Lamontagne, R. & Moffat, A. F. J. 1987, AJ, 94, 1008
- Lamontagne, R., Moffat, A. F. J., Drissen, L., Robert, C., & Matthews, J. M. 1996, AJ, 112, 2227
- Langer, N. 2012, Annual Review of Astronomy and Astrophysics, vol. 50, p.107-164, 50, 107
- Langer, N., Hamann, W.-R., Lennon, M., et al. 1994, Astronomy and Astrophysics, Vol. 290, p.819-833 (1994), 290, 819
- Langer, N., Schürmann, C., Stoll, K., et al. 2020, Astronomy & Astrophysics, Volume 638, id.A39, 18 pp., 638, A39
- Lefèvre, L., Marchenko, S. V., Lépine, S., et al. 2005, Monthly Notices of the Royal Astronomical Society, 360, 141, aDS Bibcode: 2005MNRAS.360..141L
- Lefèvre, L., Marchenko, S. V., Lépine, S., et al. 2005, MNRAS, 360, 141
- Lefèvre, L., Marchenko, S. V., Moffat, A. F. J., et al. 2005, The Astrophysical Journal, 634, L109, aDS Bibcode: 2005ApJ...634L.109L
- Lépine, S., Moffat, A. F. J., & Henriksen, R. N. 1996, The Astrophysical Journal, 466, 392, aDS Bibcode: 1996ApJ...466..392L
- Lépine, S., Moffat, A. F. J., St-Louis, N., et al. 2000, The Astronomical Journal, 120, 3201, aDS Bibcode: 2000AJ....120.3201L
- Lewis, D., Moffat, A. F. J., Matthews, J. M., Robert, C., & Marchenko, S. V. 1993, ApJ, 405, 312
- Lomb, N. R. 1976, Ap&SS, 39, 447
- Lomb, N. R. 1976, Astrophysics and Space Science, Volume 39, Issue 2, pp.447-462, 39, 447
- Lucy, L. B. & Solomon, P. M. 1970, ApJ, 159, 879
- Lührs, S. & Moffat, A. F. J. 2002, 260, 555, conference Name: Interacting Winds from Massive Stars ADS Bibcode: 2002ASPC..260..555L
- Lührs, S. & Moffat, A. F. J. 2002, in Astronomical Society of the Pacific Conference Series, Vol. 260, Interacting Winds from Massive Stars, ed. A. F. J. Moffat & N. St-Louis, 555

- Mac Low, M.-M., Balsara, D. S., Kim, J., & de Avillez, M. A. 2005, The Astrophysical Journal, 626, 864, aDS Bibcode: 2005ApJ...626..864M
- MacLeod, M. & Loeb, A. 2020, The Astrophysical Journal, 895, 29, aDS Bibcode: 2020ApJ...895...29M
- Maeder, A. & Meynet, G. 1994, Astronomy and Astrophysics, Vol. 287, p.803-816 (1994), 287, 803
- Mahy, L., Lanthermann, C., Hutsemékers, D., et al. 2022, Astronomy & Astrophysics, Volume 657, id.A4, 15 pp., 657, A4
- Maíz Apellániz, J., Barbá, R. H., Fariña, C., et al. 2021, A&A, 646, A11
- Maíz Apellániz, J., Sota, A., Arias, J. I., et al. 2016, The Astrophysical Journal Supplement Series, 224, 4, aDS Bibcode: 2016ApJS..224....4M
- Maíz Apellániz, J., Trigueros Páez, E., Negueruela, I., et al. 2019, Astronomy & Astrophysics, Volume 626, id.A20, 39 pp., 626, A20
- Manick, R., Miszalski, B., & McBride, V. 2015, MNRAS, 448, 1789
- Marchenko, S. V. & Moffat, A. F. J. 1998, The Astrophysical Journal, 499, L195, aDS Bibcode: 1998ApJ...499L.195M
- Marchenko, S. V., Moffat, A. F. J., Crowther, P. A., et al. 2004, MNRAS, 353, 153
- Marchenko, S. V., Moffat, A. F. J., & Eenens, P. R. J. 1998a, PASP, 110, 1416
- Marchenko, S. V., Moffat, A. F. J., Eenens, P. R. J., Hill, G. M., & Grandchamps, A. 1995, The Astrophysical Journal, 450, 811, aDS Bibcode: 1995ApJ...450..811M
- Marchenko, S. V., Moffat, A. F. J., & Grosdidier, Y. 1999, ApJ, 522, 433
- Marchenko, S. V., Moffat, A. F. J., & Koenigsberger, G. 1994, ApJ, 422, 810
- Marchenko, S. V., Moffat, A. F. J., Lamontagne, R., & Tovmassian, G. H. 1996, The Astrophysical Journal, 461, 386, aDS Bibcode: 1996ApJ...461..386M
- Marchenko, S. V., Moffat, A. F. J., van der Hucht, K. A., et al. 1998b, A&A, 331, 1022
- Marchenko, S. V., Moffat, A. F. J., van der Hucht, K. A., et al. 1998, Astronomy and Astrophysics, v.331, p.1022-1036 (1998), 331, 1022
- Mason, B. D., Gies, D. R., Hartkopf, W. I., et al. 1998, The Astronomical Journal, 115, 821, aDS Bibcode: 1998AJ....115..821M
- Mason, B. D., Hartkopf, W. I., Gies, D. R., Henry, T. J., & Helsel, J. W. 2009, The Astronomical Journal, 137, 3358, aDS Bibcode: 2009AJ....137.3358M

- Massey, P. 1981, *The Astrophysical Journal*, 244, 157, aDS Bibcode: 1981ApJ...244..157M
- Massey, P. 1981, *ApJ*, 244, 157
- Massey, P. 1984, *The Astrophysical Journal*, 281, 789, aDS Bibcode: 1984ApJ...281..789M
- Massey, P. & Niemela, V. S. 1981, *ApJ*, 245, 195
- Mauerhan, J. C., Van Dyk, S. D., & Morris, P. W. 2009, *Publications of the Astronomical Society of the Pacific*, 121, 591, aDS Bibcode: 2009PASP..121..591M
- Meynet, G. & Maeder, A. 2003, *Astronomy and Astrophysics*, v.404, p.975-990 (2003), 404, 975
- Meynet, G. & Maeder, A. 2003, *A&A*, 404, 975
- Meynet, G. & Maeder, A. 2005, *Astronomy and Astrophysics*, v.429, p.581-598 (2005), 429, 581
- Michaux, Y. J. L., Moffat, A. F. J., Chené, A.-N., & St-Louis, N. 2014, *MNRAS*, 440, 2
- Miszalski, B., Acker, A., Moffat, A. F. J., Parker, Q. A., & Udalski, A. 2009, *A&A*, 496, 813
- Miszalski, B., Corradi, R. L. M., Jones, D., et al. 2011, in *Asymmetric Planetary Nebulae 5 Conference*, ed. A. A. Zijlstra, F. Lykou, I. McDonald, & E. Lagadec, 328
- Miszalski, B., Manick, R., & McBride, V. 2015, in *EAS Publications Series*, Vol. 71-72, *EAS Publications Series*, 117–120
- Moe, M. & Di Stefano, R. 2017, *The Astrophysical Journal Supplement Series*, 230, 15, aDS Bibcode: 2017ApJS..230...15M
- Moens, N., Poniatowski, L. G., Hennicker, L., et al. 2022, arXiv e-prints, arXiv:2203.01108
- Moffat, A. F. J., Drissen, L., Lamontagne, R., & Robert, C. 1988, *ApJ*, 334, 1038
- Moffat, A. F. J. & Haupt, W. 1974, *A&A*, 32, 435
- Moffat, A. F. J., Lamontagne, R., Seggewiss, W. 1982, *Astronomy and Astrophysics*, Vol. 114, p. 135-146 (1982), 114, 135
- Moffat, A. F. J., Lamontagne, R., Shara, M. M., & McAlister, H. A. 1986, *AJ*, 91, 1392
- Moffat, A. F. J. & Shara, M. M. 1986, *The Astronomical Journal*, 92, 952, aDS Bibcode: 1986AJ.....92..952M

- Moffat, A. F. J. & Shara, M. M. 1986, AJ, 92, 952
- Monnier, J. D., Zhao, M., Pedretti, E., et al. 2011, ApJ, 742, L1
- Morel, T., Georgiev, L. N., Grosdidier, Y., et al. 1999, A&A, 349, 457
- Morel, T., Georgiev, L. N., Grosdidier, Y., et al. 1999, *Astronomy and Astrophysics*, v.349, p.457-466 (1999), 349, 457
- Morel, T., St-Louis, N., & Marchenko, S. V. 1997, ApJ, 482, 470
- Munoz, M., Moffat, A. F. J., Hill, G. M., et al. 2017, *Monthly Notices of the Royal Astronomical Society*, 467, 3105, aDS Bibcode: 2017MNRAS.467.3105M
- Neijssel, C. J., Vinciguerra, S., Vigna-Gómez, A., et al. 2021, *The Astrophysical Journal*, 908, 118, aDS Bibcode: 2021ApJ...908..118N
- Neugent, K. F. & Massey, P. 2014, *The Astrophysical Journal*, 789, 10, aDS Bibcode: 2014ApJ...789...10N
- Niemela, V. S., Gamen, R., Morrell, N. I., & Giménez Benítez, S. 1999, in *IAU Symposium*, Vol. 193, Wolf-Rayet Phenomena in Massive Stars and Starburst Galaxies, ed. K. A. van der Hucht, G. Koenigsberger, & P. R. J. Eenens, 26
- Niemela, V. S., Morrell, N. I., Barba, R. H., & Bosch, G. L. 1996, in *Revista Mexicana de Astronomía y Astrofísica Conference Series*, Vol. 5, *Revista Mexicana de Astronomía y Astrofísica Conference Series*, ed. V. Niemela, N. Morrell, P. Pismis, & S. Torres-Peimbert, 100–102
- Niemela, V. S., Shara, M. M., Wallace, D. J., Zurek, D. R., & Moffat, A. F. J. 1998, AJ, 115, 2047
- Nieuwenhuijzen, H. & de Jager, C. 1990, A&A, 231, 134
- Owocki, S. P., Castor, J. I., & Rybicki, G. B. 1988, ApJ, 335, 914
- Paczyński, B. 1967, ACTA, 17, 355
- Paczyński, B. 1967, *Acta Astronomica*, 17, 355, aDS Bibcode: 1967AcA....17..355P
- Palate, M., Rauw, G., De Becker, M., Nazé, Y., & Eenens, P. 2013, A&A, 560, A27
- Patrick, L. R., Evans, C. J., Davies, B., et al. 2019, 344, 213, conference Name: Dwarf Galaxies: From the Deep Universe to the Present ADS Bibcode: 2019IAUS..344..213P
- Patrick, L. R., Lennon, D. J., Britavskiy, N., et al. 2019, A&A, 624, A129
- Podsiadlowski, P., Joss, P. C., & Hsu, J. J. L. 1992, ApJ, 391, 246

- Pols, O. R. 1994, *Astronomy and Astrophysics*, Vol. 290, p.119-128 (1994), 290, 119
- Pols, O. R. 1994, *A&A*, 290, 119
- Poniatowski, L. G., Sundqvist, J. O., Kee, N. D., et al. 2021, *A&A*, 647, A151
- Puls, J., Markova, N., Scuderi, S., et al. 2006, *Astronomy and Astrophysics*, Volume 454, Issue 2, August I 2006, pp.625-651, 454, 625
- Raskin, G., van Winckel, H., Hensberge, H., et al. 2011, *Astronomy and Astrophysics*, Volume 526, id.A69, 12 pp., 526, A69
- Rate, G. & Crowther, P. A. 2020, *Monthly Notices of the Royal Astronomical Society*, 493, 1512, aDS Bibcode: 2020MNRAS.493.1512R
- Richardson, N. D., Lee, L., Schaefer, G., et al. 2021, *ApJ*, 908, L3
- Richardson, N. D., Shenar, T., Roy-Loubier, O., et al. 2016, *Monthly Notices of the Royal Astronomical Society*, 461, 4115, aDS Bibcode: 2016MNRAS.461.4115R
- Richardson, N. D., Shenar, T., Roy-Loubier, O., et al. 2016, *MNRAS*, 461, 4115
- Ro, S. 2019, *The Astrophysical Journal*, 873, 76, aDS Bibcode: 2019ApJ...873...76R
- Ro, S. & Matzner, C. D. 2016, *ApJ*, 821, 109
- Robert, C. & Moffat, A. F. J. 1989, *The Astrophysical Journal*, 343, 902, aDS Bibcode: 1989ApJ...343..902R
- Robert, C., Moffat, A. F. J., Bastien, P., Drissen, L., & St. -Louis, N. 1989, *ApJ*, 347, 1034
- Robert, C., Moffat, A. F. J., Drissen, L., et al. 1992, *ApJ*, 397, 277
- Robertson, B. E., Ellis, R. S., Dunlop, J. S., McLure, R. J., & Stark, D. P. 2010, *Nature*, 468, 49, aDS Bibcode: 2010Natur.468...49R
- Rodríguez, L. F., Arthur, J., Montes, G., Carrasco-González, C., & Toalá, J. A. 2020, *ApJ*, 900, L3
- Rosslowe, C. K. & Crowther, P. A. 2015, *Monthly Notices of the Royal Astronomical Society*, 447, 2322, aDS Bibcode: 2015MNRAS.447.2322R
- Rosslowe, C. K. & Crowther, P. A. 2018, *Monthly Notices of the Royal Astronomical Society*, 473, 2853, aDS Bibcode: 2018MNRAS.473.2853R
- Rustamov, D. N. & Cherepashchuk, A. M. 1989, *Soviet Ast.*, 33, 36
- Rustamov, D. N. & Cherepashchuk, A. M. 2012, *Astronomy Reports*, 56, 761, aDS Bibcode: 2012ARep...56..761R

- Sana, H., de Koter, A., de Mink, S. E., et al. 2013, *Astronomy & Astrophysics*, Volume 550, id.A107, 22 pp., 550, A107
- Sana, H., de Mink, S. E., de Koter, A., et al. 2012, *Science*, 337, 444, aDS Bibcode: 2012Sci...337..444S
- Sana, H., de Mink, S. E., de Koter, A., et al. 2012, *Science*, 337, 444
- Sana, H., Le Bouquin, J. B., Lacour, S., et al. 2014, *The Astrophysical Journal Supplement Series*, 215, 15, aDS Bibcode: 2014ApJS..215...15S
- Sander, A., Hamann, W.-R., & Todt, H. 2012, *Astronomy & Astrophysics*, Volume 540, id.A144, 79 pp., 540, A144
- Sander, A., Hamann, W. R., & Todt, H. 2012, *A&A*, 540, A144
- Sander, A. A. C., Hamann, W. R., Todt, H., Hainich, R., & Shenar, T. 2017, *A&A*, 603, A86
- Sander, A. a. C., Hamann, W.-R., Todt, H., et al. 2019, *Astronomy & Astrophysics*, Volume 621, id.A92, 19 pp., 621, A92
- Sanyal, D., Grassitelli, L., Langer, N., & Bestenlehner, J. M. 2015, *Astronomy & Astrophysics*, Volume 580, id.A20, 24 pp., 580, A20
- Scargle, J. D. 1982, *ApJ*, 263, 835
- Scargle, J. D. 1982, *The Astrophysical Journal*, 263, 835, aDS Bibcode: 1982ApJ...263..835S
- Schmutz, W. & Koenigsberger, G. 2019, *A&A*, 624, L3
- Schnurr, O., Moffat, A. F. J., St-Louis, N., Morrell, N. I., & Guerrero, M. A. 2008, *Monthly Notices of the Royal Astronomical Society*, 389, 806, aDS Bibcode: 2008MNRAS.389..806S
- Shara, M. M., Faherty, J. K., Zurek, D., et al. 2012, *The Astronomical Journal*, 143, 149, aDS Bibcode: 2012AJ....143..149S
- Shara, M. M., Moffat, A. F. J., Gerke, J., et al. 2009, *The Astronomical Journal*, 138, 402, aDS Bibcode: 2009AJ....138..402S
- Shenar, T., Gilkis, A., Vink, J. S., Sana, H., & Sander, A. a. C. 2020, *Astronomy & Astrophysics*, Volume 634, id.A79, 12 pp., 634, A79
- Shenar, T., Sablowski, D. P., Hainich, R., et al. 2019, arXiv e-prints, arXiv:1905.09296
- Shenar, T., Sablowski, D. P., Hainich, R., et al. 2019, *Astronomy & Astrophysics*, Volume 627, id.A151, 68 pp., 627, A151

- Shulyak, D., Tsymbal, V., Ryabchikova, T., Stütz, C., & Weiss, W. W. 2004, *Astronomy and Astrophysics*, v.428, p.993-1000 (2004), 428, 993
- Skinner, S., Güdel, M., Schmutz, W., & Zhekov, S. 2006, *Astrophysics and Space Science*, 304, 97
- Smette, A., Sana, H., Noll, S., et al. 2015, *Astronomy & Astrophysics*, Volume 576, id.A77, 17 pp., 576, A77
- Smith, L. F. 1968, *MNRAS*, 138, 109
- Smith, L. F. 1968a, *Monthly Notices of the Royal Astronomical Society*, 140, 409, aDS Bibcode: 1968MNRAS.140..409S
- Smith, L. F. 1968b, *Monthly Notices of the Royal Astronomical Society*, 138, 109, aDS Bibcode: 1968MNRAS.138..109S
- Smith, N. 2014, *Annual Review of Astronomy and Astrophysics*, vol. 52, p.487-528, 52, 487
- Smith, N. & Conti, P. S. 2008, *ApJ*, 679, 1467
- Smith, N. & Owocki, S. P. 2006, *The Astrophysical Journal*, 645, L45, aDS Bibcode: 2006ApJ...645L..45S
- Soberman, G. E., Phinney, E. S., & van den Heuvel, E. P. J. 1997, *A&A*, 327, 620
- Soberman, G. E., Phinney, E. S., & van den Heuvel, E. P. J. 1997, *Astronomy and Astrophysics*, v.327, p.620-635, 327, 620
- St-Louis, N. 2013, *ApJ*, 777, 9
- St-Louis, N., Chené, A. N., de La Chevrotière, A., & Moffat, A. F. J. 2008, 388, 79, conference Name: Mass Loss from Stars and the Evolution of Stellar Clusters ADS Bibcode: 2008ASPC..388...79S
- St-Louis, N., Chené, A. N., Schnurr, O., & Nicol, M. H. 2009, *The Astrophysical Journal*, 698, 1951, aDS Bibcode: 2009ApJ..698.1951S
- St-Louis, N., Moffat, A. F. J., Ramiaramanantsoa, T., & Lenoir-Craig, G. 2020, BRITE Photometric Variability of the Intriguing Wolf-Rayet Star WR6: Rotational or Binary Modulations?, conference Name: Stars and their Variability Observed from Space Pages: 423-426 ADS Bibcode: 2020svos.conf..423S
- St-Louis, N., Tremblay, P., & Ignace, R. 2018, *Monthly Notices of the Royal Astronomical Society*, 474, 1886, aDS Bibcode: 2018MNRAS.474.1886S
- Stevens, I. R., Blondin, J. M., & Pollock, A. M. T. 1992, *ApJ*, 386, 265

- Sundqvist, J. O. & Owocki, S. P. 2013, MNRAS, 428, 1837
- Sundqvist, J. O., Owocki, S. P., & Puls, J. 2018, A&A, 611, A17
- Tanvir, N. R., Fox, D. B., Levan, A. J., et al. 2009, Nature, 461, 1254, aDS Bibcode: 2009Natur.461.1254T
- Thomas, J. D., Richardson, N. D., Eldridge, J. J., et al. 2021, Monthly Notices of the Royal Astronomical Society, 504, 5221, aDS Bibcode: 2021MNRAS.504.5221T
- Tkachenko, A. 2015, Astronomy & Astrophysics, Volume 581, id.A129, 18 pp., 581, A129
- Toalá, J. A., Guerrero, M. A., Ramos-Larios, G., & Guzmán, V. 2015, Astronomy & Astrophysics, Volume 578, id.A66, 11 pp., 578, A66
- Toalá, J. A., Oskinova, L. M., Hamann, W. R., et al. 2018, The Astrophysical Journal, 869, L11, aDS Bibcode: 2018ApJ...869L..11T
- Todt, H., Sander, A., Hainich, R., et al. 2015, A&A, 579, A75
- Todt, H., Sander, A., Hainich, R., et al. 2015, Astronomy & Astrophysics, Volume 579, id.A75, 6 pp., 579, A75
- Tody, D. 1993, 52, 173, conference Name: Astronomical Data Analysis Software and Systems II ADS Bibcode: 1993ASPC...52..173T
- Tonry, J. & Davis, M. 1979, The Astronomical Journal, 84, 1511, aDS Bibcode: 1979AJ.....84.1511T
- Toonen, S., Boekholt, T. C. N., & Portegies Zwart, S. 2022, Astronomy & Astrophysics, Volume 661, id.A61, 25 pp., 661, A61
- Toonen, S., Portegies Zwart, S., Hamers, A. S., & Bandopadhyay, D. 2020, Astronomy & Astrophysics, Volume 640, id.A16, 18 pp., 640, A16
- Tsymbal, V. 1996, 108, 198, conference Name: M.A.S.S., Model Atmospheres and Spectrum Synthesis ADS Bibcode: 1996ASPC..108..198T
- Underhill, A. B. & Hill, G. M. 1994, ApJ, 432, 770
- van der Hucht, K. A. 2001, NewAR, 45, 135
- van der Hucht, K. A. 2001, New Astronomy Reviews, 45, 135, aDS Bibcode: 2001NewAR..45..135V
- Vanbeveren, D. & Conti, P. S. 1980, A&A, 88, 230

- Vanbeveren, D. & Conti, P. S. 1980, *Astronomy and Astrophysics*, Vol. 88, p. 230-239 (1980), 88, 230
- Vanbeveren, D., De Donder, E., Van Bever, J., Van Rensbergen, W., & De Loore, C. 1998, *NewA*, 3, 443
- Vanbeveren, D., De Donder, E., Van Bever, J., Van Rensbergen, W., & De Loore, C. 1998, *New Astronomy*, 3, 443, aDS Bibcode: 1998NewA....3..443V
- Varricatt, W. P. & Ashok, N. M. 2006, *MNRAS*, 365, 127
- Villaseñor, J. I., Taylor, W. D., Evans, C. J., et al. 2021, *Monthly Notices of the Royal Astronomical Society*, 507, 5348, aDS Bibcode: 2021MNRAS.507.5348V
- Vink, J. S. & de Koter, A. 2005, *Astronomy and Astrophysics*, Volume 442, Issue 2, November I 2005, pp.587-596, 442, 587
- Vink, J. S., de Koter, A., & Lamers, H. J. G. L. M. 2001, *Astronomy and Astrophysics*, v.369, p.574-588 (2001), 369, 574
- Webster, B. L. & Glass, I. S. 1974, *MNRAS*, 166, 491
- Wesselowski, U. & Niedzielski, A. 1996, in *Roentgenstrahlung from the Universe*, ed. H. U. Zimmermann, J. Trümper, & H. Yorke, 73–74
- Williams, P. M. 1995, in *Wolf-Rayet Stars: Binaries; Colliding Winds; Evolution*, ed. K. A. van der Hucht & P. M. Williams, Vol. 163, 335
- Williams, P. M. 2014, *MNRAS*, 445, 1253
- Williams, P. M. 2019, *MNRAS*, 488, 1282
- Williams, P. M., Kidger, M. R., van der Hucht, K. A., et al. 2001, *MNRAS*, 324, 156
- Williams, P. M., van der Hucht, K. A., & Rauw, G. 2005, arXiv e-prints, astro
- Woosley, S. E. & Bloom, J. S. 2006, *Annual Review of Astronomy & Astrophysics*, vol. 44, Issue 1, pp.507-556, 44, 507
- Zahn, J. P. 1977, *A&A*, 57, 383
- Zhekov, S. A. 2017, *MNRAS*, 472, 4374
- Zhekov, S. A., Petrov, B. V., Tomov, T. V., & Peshev, P. 2020, *MNRAS*, 494, 4525
- Zucker, S. 2003, *Monthly Notices of the Royal Astronomical Society*, 342, 1291, aDS Bibcode: 2003MNRAS.342.1291Z
- Zucker, S. 2003, *MNRAS*, 342, 1291

List of publications

Publications in refereed journals:

1. Royer, P., **Dsilva, K.** et. al in prep., *MELCHIORS: The Mercator Library of High Resolution Stellar Spectroscopy*
2. Toalá, J.A., Bowman, D., Van Reeth, T., Todt, H., **Dsilva, K.**, Shenar, T., Koenigsberger, G., Estrada-Dorado, S., Oskinova, L.M., and Hamann, W.-R., *Multiple variability time-scales of the early nitrogen-rich Wolf-Rayet star WR7*
3. **Dsilva, K.**, Shenar, T., Sana, H., and Marchant, P., *A spectroscopic multiplicity survey of Galactic Wolf-Rayet stars: II. The northern WNE sequence*
4. Frost, A.J., Bodensteiner, J., Rivinius, T., Baade, D., Merand, A., Selman, F., Abdul-Masih, M., Banyard, G., Bordier, E., **Dsilva, K.**, Hawcroft, C., Mahy, L., Reggiani, M., Shenar, T., Cabezas, M., Hadraiva, P., Heida, M., Klement, R., and Sana, H., *HR 6819 is a binary system with no black hole. Revisiting the source with infrared interferometry and optical integral field spectroscopy*
5. Kluska, J., Van Winckel, H., Coppée, Q., Oomen, G.-M., **Dsilva, K.**, Kamath, D., Bujarrabal, V., and Min, M., *A population of transition disks around evolved stars: Fingerprints of planets. Catalog of disks surrounding Galactic post-AGB binaries*
6. Bodensteiner, J., Shenar, T., Mahy, L., Fabry, M., Marchant, P., Abdul-Masih, M., Banyard, G., Bowman, D.M., **Dsilva, K.**, Frost, A.J., Hawcroft, C., Reggiani, M., and Sana, H., *On the binary origin of Be stars and the nature of exotic Be binary systems*
7. Shenar, T., Sana, H., Marchant, P., Pablo, B., Richardson, N., Moffat, A.F.J., Van Reeth, T., Barbá, R.H., Bowman, D.M., Broos, P., Crowther, P.A., Clark, J.S., de Koter, A., de Mink, S.E., **Dsilva, K.**, Gräfener, G., Howarth, I.D., Langer, N., Mahy, L., Maíz Apellániz, J., Pollock, A.M.T., Schneider, F.R.N., Townsley,

- L., and Vink, J.S., *The Tarantula Massive Binary Monitoring. V. R 144: a wind-eclipsing binary with a total mass $\gtrsim 140 M_{\odot}$*
8. Johnston, C., Aimar, N., Abdul-Masih, M., Bowman, D.M., White, T.R., Hawcroft, C., Sana, H., Sekaran, S., **Dsilva, K.**, Tkachenko, A., and Aerts, C., *Characterization of the variability in the O+B eclipsing binary HD 165246*
9. Bodensteiner, J., Shenar, T., Mahy, L., Fabry, M., Marchant, P., Abdul-Masih, M., Banyard, G., Bowman, D.M., **Dsilva, K.**, Frost, A.J., Hawcroft, C., Reggiani, M., and Sana, H., *Is HR 6819 a triple system containing a black hole?. An alternative explanation*
10. **Dsilva, K.**, Shenar, T., Sana, H., and Marchant, P., *A spectroscopic multiplicity survey of Galactic Wolf-Rayet stars. I. The northern WC sequence*
11. Shenar, T., Bodensteiner, J., Abdul-Masih, M., Fabry, M., Mahy, L., Marchant, P., Banyard, G., Bowman, D.M., **Dsilva, K.**, Hawcroft, C., Reggiani, M., and Sana, H., *The "hidden" companion in LB-1 unveiled by spectral disentangling*
12. Shenar, T., **Dsilva, K.**, Gilkis, A., Hainich, R., Hamann, W.-R., Janssens, S., Mahy, L., Marchant Campos, P.I., Osokinova, L., Ramachandran, V., Sander, A., and Todt, H., *The multiplicity and properties of the LMC WC stars: the immediate progenitors of black holes and stripped supernovae*
13. Abdul-Masih, M., Banyard, G., Bodensteiner, J., Bordier, E., Bowman, D.M., **Dsilva, K.**, Fabry, M., Hawcroft, C., Mahy, L., Marchant, P., Raskin, G., Reggiani, M., Shenar, T., Tkachenko, A., Van Winckel, H., Vermeylen, L., and Sana, H., *On the signature of a 70-solar-mass black hole in LB-1*
14. **Dsilva, K.**, Van Winckel, H., and Kluska, J., *A systematic survey of grain growth in discs around post-AGB binaries with PACS and SPIRE photometry*

FACULTY OF SCIENCE
DEPARTMENT OF PHYSICS AND ASTRONOMY
INSTITUTE OF ASTRONOMY
Celestijnlaan 200D box 2401
B-3001 Leuven
<https://fys.kuleuven.be/ster>

